PART I: FABRICATION AND SURFACE MODIFICATION OF COMPOSITE BIOMATERIALS BASED ON SILICON AND CALCIUM DISILICIDE

PART II: SYNTHESIS AND CHARACTERIZATION OF ERBIUM DOPED SILICON NANOCRYSTALS ENCAPSULATED BY ALUMINUM AND ZINC OXIDES

by

VLADIMIR VICTOR SEREGIN

Bachelor of Science, May 2001
University of Texas A&M - Commerce
Commerce, Texas

Submitted to the Graduate Faculty of the
College of Science and Engineering
Texas Christian University
in partial fulfillment of the requirements
for the degree of

Doctor of Philosophy

May, 2006

Copyright by
Vladimir Victor Seregin
2006

ACKNOWLEDGEMENTS

I would like to thank Dr. Jeffery L. Coffer for research supervision and publications revision. I am also grateful for his conveying to me the critical scientific thinking and the ability to successfully compete in the field of modern science. Finally, I thank him for understanding my research habits and managing my time in a way that allowed me to mature as a person and grow as a scientist.

Arriving at Texas Christian University (TCU), I began to appreciate the well developed laboratory skills I had received at Texas A&M University-Commerce, conducting undergraduate research under the direction of Dr. Yen-Yan J. Wu and Dr. Kenneth Ashley. I sincerely regret my occasional ignorance and arrogance demonstrations and would like to thank both of them for their outstanding teaching performance.

I would like thank those who offered an advice on my research and/or allowed me to use their equipment: Dr. Senter, Dr. Mukherjee, Dr. Montchamp, Dr. Albright, Dr. Hanna, Dr. Minter, Dr. Zerda, Dr. Nelson, Dr. Annunziata, Dr. Nelson, and Ji Wu. For useful discussions and a kind word, I thank the rest of TCU Chemistry faculty, Biology Department faculty, and TCU staff. In particular, I thank David Yale, Jerry Katchinska and Pam Davis for their professional expertise and friendship. Finally, I would like to thank my fellow students at TCU Departments of Chemistry and many others for any help and support. My gratitude is also extended to the members of Coffer’s group.

Financial support was provided in part by the Robert A. Welch Foundation, National Science Foundation, and by Texas Advanced Technology Program.

TABLE OF CONTENTS

PART I: FABRICATION AND SURFACE MODIFICATION OF COMPOSITE BIOMATERIALS BASED ON SILICON AND CALCIUM DISILICIDE

PART II: SYNTHESIS AND CHARACTERIZATION OF ERBIUM DOPED SILICON NANOCRYSTALS ENCAPSULATED BY ALUMINUM AND ZINC OXIDES

LIST OF FIGURES

LIST OF TABLES

LIST OF ABBREVIATIONS

BET	Brunauer-Emmett-Teller
BIOPSi	partially-porosified silicon
CAp	carbonate apatite
CaP	calcium phosphate
CM	carrier mediated
CCD	charge coupled device
CVD	chemical vapor deposition
CZ	Czochralski
DE	direct excitation
DI	de-ionized
DMSO	dimethyl sulfoxide
EDTA	ethylenediaminetetraacetic acid
EDX	X-ray energy dispersive spectroscopy (XEDS)
EL	electroluminescence
EMB	embedded
EtOH	ethanol
EXAFS	extended x-ray absorption fine structure
FITC	fluorescein isothiocyanate
HA	hydroxyapatite
ICP	inductively coupled plasma
iPr	isopropyl
IR	infrared
MFC	mass flow controller
NC	nanocrystal
O-iPr	isopropoxide
PCL	polycaprolactone
PL	photoluminescence
ppm	part per million
RD	randomly dispersed

RTP	rapid thermal processor
SBF	simulated body fluid
sccm	standard cubic centimeter
SE	surface enriched
SEM	scanning electron microscopy
TCMP	magnesium-substituted whitlockite
TCP	tricalcium phosphate
TEM	transmission electron microscopy
THF	tetrahydrofuran
tmhd	2,2,6,6-tetramethylheptanedionato
UV	ultraviolet
XRD	X-ray diffraction

Part I

CHAPTER I.

Literature Review

1.0 Introduction

1.0.1 Importance of Silicon in Bioelectronics

Nonviable synthetic or modified natural materials interfaced with biological systems are referred to as biomaterials, particularly if they are intended for use in a medical device.[1] The challenging and fascinating field of biomaterials continues to attract scholars from chemistry, chemical engineering, materials science, mechanics, surface science, bioengineering, biology, and medicine.[1] Replacements of biological tissues, controlled drug delivery and *in situ* diagnostics represent frontiers of biomedical materials research.[2] As the search for new biomaterials continues, one focus point is the development of bioactive silicon-based platforms for constructing integrated circuits which can operate *in vivo*.

Biomaterials have evolved through several generations. Bio-inert materials came first, originally created with intention to match the physical properties of the replaced tissues with a minimal toxic response in the host.[3] Next came bioactive and biodegradable materials with low toxicity and the ability to affect their physiological environment by either some controlled action or by undergoing physicochemical transformations in response to a biological stimuli.[4] At the present time, the odds of being used in a medical application favor those biomaterials which are able to perform a programmed task *in vivo* and subsequently biodegrade, thereby eliminating chronic foreign body reactions.[5] If used in a tissue engineering application (*e.g.* replacing damaged or diseased tissue through self-healing), degradation of a biomaterial will also generate additional volume for regenerated tissues.

A major challenge associated with the latest generation of biomaterials, so-called “smart” biomaterials, is the design of biomedical devices that stimulate specific cellular responses at the molecular level and/or respond to specific cellular signals themselves.[4,6] Many developed tissue engineering constructs, drug delivery systems, and biosensors integrate within living organisms by employing their tailored physicochemical properties. The bioactivity of such devices is strongly dependent on complex chemical reactions. An alternative comes from the emerging field of bioelectronics[7] which targets the development of materials whose biologically relevant actions can be significantly altered by a simple application of electric bias.

Recent advances in organic electronics are considered by some to be the key to the development of silicon microchip-like bioprocessor and their subsequent implementation in medicine.[8] For example, Hill and co-workers have synthesized highly-conductive three-dimensional bioelectronic architectures through metallization of proteins that show great promise for monitoring and stimulating biological processes *in situ.*[9] In addition, biologically functional tissue scaffolds can be fabricated through the encapsulation of bioactive compounds within biodegradable polymer fibers.[10] In theory, this method can be complemented by the addition of a conductive polymer to a biodegradable polymer (*e.g.* polyaniline, polypyrole), thereby producing an electronically-responsive material.[11-13] While such approaches build on a platform that is organic-based, existing microelectronics technology is nonetheless dominated by silicon,[14,15] and a bioactive silicon microchip is the optimal choice for an electronically-responsive platform in the construction of integrated circuits operating *in vivo*.

1.0.2 Bone Structure and Bone Tissue Engineering

Bone, the anchoring point for most skeletal muscles and ligaments, is a living tissue able to undergo spontaneous regeneration and to remodel its structure through a delicate balance between an osteogenic (bone forming) and osteoclatic (bone removing) processes.[5] Orthopedic practice began in the time of Hippocrates (460-377 BC), who treated every known spine and limb disorder.[7,16] The term "orthopaedia" was created by Nicholas Andry in 1742 to describe the practice of preventing and correcting deformity and improving function of the spine and limbs.[16] While initially the field was dominated by orthopedic surgery, finding better methods of preventing and treating bone disorders that cause pain and loss of mobility for middle-aged and older people is perhaps the greatest clinical and scientific challenge to orthopedics at the beginning of the twenty-first century.[16]

The term bone refers to a family of materials, all of which have evolved to fulfill a variety of mechanical functions.[17] In this context, calcium phosphate phases make up the mineral component of bone and are responsible for its strength and integrity. Bone diseases (*e.g.* osteoporosis) disrupt the delicate balance between bone resorption and formation, thereby affecting the strength and integrity of bones.[18] In order to successfully treat these diseases, one must understand the mechanism of biomineralization. Biomineralization (biologically induced mineralization) is the process by which minerals deposit within or outside the cells of a variety of organisms.[19,20] Calcification is the term reserved specifically for biologically induced deposition of calcium phosphates (CaP). Osteoblasts are cells that deposit calcium phosphates *in vivo*, using blood plasma as the source of calcium, *etc.* Concurrently, osteoclasts dissolve bones. Various bone disease therapies are designed to selectively regulate action of either one of them in several different ways. For example, osteoporosis in postmenopausal women is caused by hormonal misbalance which reduces differentiation of stem cells into osteoblasts. As a result, bone dissolution by osteoclasts occurs at a faster rate than bone formation. When these women undergo estrogen therapy, hormonal misbalance is reduced. Another treatment method, the dietary intake of sodium fluoride, does not affect either one of these cells, but rather results in the formation of a less soluble calcium phosphate phase--fluoroapatite (in place of hydroxyapatite), and the rate of bone destruction by osteoclasts is reduced. Another approach is to increase daily intake of calcium, thereby shifting the chemical equilibrium towards calcium phosphate formation according to Le Chatelier's principle.

Applying scientific principles to design, construct, modify, grow, and maintain living tissue is what defines the discipline of tissue engineering.[5] The use of cells isolated by enzymatic dissociation of donor tissue to construct bioartificial tissues *in vitro*, and the *in vivo* alteration of cell growth/function are the two general categories of tissue engineering.[5] In the field of orthopedics, bone tissue engineering and development of new materials for bone substitution are considered by some to be "one of the most important objectives of science today".[21] It is important to understand that the discipline of bone tissue engineering targets the goal of obtaining control over selective deposition of calcium phosphates *in vivo* via chemical or biological reactions. If such control is achieved, a synthetic material is rendered 'bioactive'. Table 1 is a list of calcium phosphates which are known to occur in normal and pathological calcifications.[22] Crystalline hydroxyapatite [$Ca_{10}(PO_4)_6(OH)_2$] is the end member of apatite family.

Calcium phosphate	Chemical formula	Occurrences
'Apatite'	$(Ca, Z)_{10}(PO_4, Y)_6(OH, X)_2$	enamel,[a] dentine,[a] bone,[a] dental calculi, stones, soft-tissue calcifications dental and urinary calculi
Octacalcium phosphate, OCP	$Ca_8H_2(PO_4)_6 \cdot 5H_2O$	dental and urinary calculi
Brushite, dicalcium phosphate dehydrate, DCPD	$CaHPO_4 \cdot 2H_2O$	dental calculi, decomposed bones
Whitlockite, tricalcium phosphate, β-TCP	$(Ca, Mg)_9(PO_4)_6$	dental and urinary calculi, dentinal caries, arthritic cartilage, soft-tissue calcifications
Amorphous calcium phosphate, ACP	$(Ca, Mg)_?(PO_4, Y')_?$	soft-tissue calcifications

Z = Na, Mg, K, Sr, etc.; Y = CO_3, HPO_4; X = Cl, F; Y′ = P_2O_7, CO_3.

Table 1. Calcium phosphates in biological systems (human). Adapted from reference 22.

In 1969 Hench *et al.* synthesized a soda-lime-phosphate-silicate glass (Bioglass^{TM}) which bonded directly to living bone when implanted *in vivo.*[23] Formation of a bond between bone and a bioactive glass involved a sequence of interfacial reactions (see Figure 1), which was initiated by the deposition of amorphous calcium phosphate and its transformation into carbonate-substituted hydroxyapatite.[3,23,24] Thereafter, it became common among researchers to declare synthetic materials as bioactive (with regard to orthopedics) if a given material's surface could autonomously initiate nucleation of CaP. While only *in vivo* calcification is the ultimate test of a material's bioactivity, biomineralization of new bone engineering constructs is now routinely investigated *in vitro*, and expensive animal studies are done only in those

		Bioactive glass
SURFACE REACTION STAGES	1&2	Formation of SiOH bonds and release of $Si(OH)_4$
	3	Formation of hydrated silica gel
	4	Adsoption of amorphous calcium phosphate
	5	Crystallization of hydroxyl carbonate apatite (HCA)
	6	Adsorption of biological moieties in HCA layer
	7	Action of macrophages
	8	Attachment of osteoblast stem cells
	9	Synchronized proliferation and differentiation of osteoblasts
	10	Generation of matrix
	11	Crystallization of matrix
	12	Growth of bone

Figure 1. Sequence of interfacial reactions involved in forming a bond between bone and a bioactive glass. Adapted from reference 23.

cases where materials show great potential to be used in a real medical application. In fact, CaP is sometimes referred to in the literature as a ‘bioactive coating’, and it is not uncommon for otherwise bioinert materials to be declared bioactive if they are coated with a thin layer of calcium phosphate.

1.0.3 Developing a Bioactive Silicon Microchip

In 1995, Canham demonstrated that layers of hydroxyapatite can be grown onto a porous silicon surface, thereby rendering it bioactive;[25] under electric bias, the growth process can be greatly accelerated.[26] Since then, patterned[27] and drug-loaded[28,29] calcified silicon electrodes have been fabricated, and the availability of a bioactive silicon-based semiconducting platform was firmly established. More recently, Santini and co-workers developed a solid-state silicon microchip (Figure 2) that can provide controlled release of single or multiple chemical substances on demand,[30] while Lahann *et al.* designed semiconductor surfaces that exhibit dynamic changes in interfacial properties in response to an electrical potential.[31] These proofs of concept open numerous possibilities for fabrication of smart biomaterials, and several groups are currently applying their discoveries to biocompatible substrates.[30,31] Although it is apparent that patterned porous silicon wafers may be well suited for this task, the development of simpler fabrication strategies to produce bioactive/biocompatible silicon surfaces is in demand.

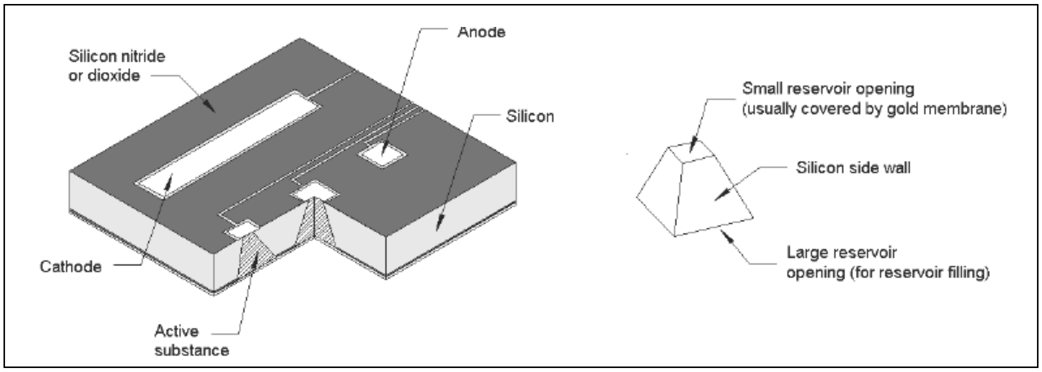

Figure 2. A prototype microchip for controlled release showing the shape of a single reservoir. Adapted from reference 30.

1.0.4 Calcium Disilicide

Until now calcium silicides were never considered by the scientific community to be used in biomedical applications. In the last three decades, research pertaining to calcium silicides was primarily focused on investigating their fundamental properties with regard to potential microelectronic applications.[32] At elevated temperatures, many metals react with silicon to form silicides,[32] and studies in this area can help to solve technological problems associated with metal-semiconductor interfaces. Calcium silicides can be considered to be structural analogs of silicides formed by other elements, including rare-earths,[33] and therefore may serve as model systems for various heterojunctions between silicon device components and metal contacts. Unfortunately, methods for fabricating epitaxial films of calcium silicides on silicon are limited to the evaporation of calcium metal onto Si wafers followed by an anneal to produce $CaSi_2$.[34-36] In addition, $CaSi_2$ and CaSi melts, prepared by heating of Ca and Si in stoichiometric proportion, exhibit superconducting behavior at high pressures[37,38] and show potential for reversible hydrogen storage,[39] respectively.

In regard to orthopedic applications, calcium disilicide ($CaSi_2$) is an appealing candidate because of its composition [silicon sheets intercalated with calcium (Figure 3)[40]] and properties. Recall that the next generation of biomaterials desire conductivity as an intrinsic property. Calcium disilicide is a semimetal, and it is the structure of the polymorphic $CaSi_2$ bulk that accounts for its metallic character, according to numerous theoretical[33,40-42]

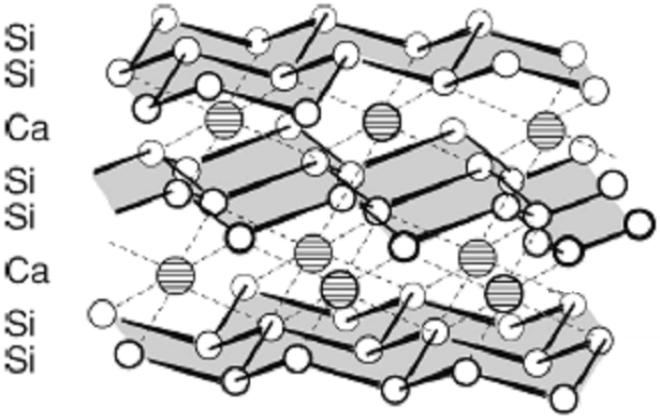

Figure 3. Schematic representation of crystalline $CaSi_2$. Adapted from reference 42.

and experimental[33,43] studies. In particular, the overlap between *p* and *d* orbitals of Si and Ca, respectively, results in a reduced energy gap between conduction and valance bands of the bulk crystalline material. In this dissertation, it will be shown that calcium disilicide ($CaSi_2$) is a novel biomaterial, able to biomineralize in the presence and absence of electric bias. When incorporated within the surface layer of a silicon wafer, $CaSi_2$ imparts bioactivity onto the underlying silicon substrate which is otherwise bioinert. In addition, $CaSi_2$-polymer composites can readily calcify and degrade *in vitro*, thereby acting as 'smart' tissue engineering scaffolds. In the absence of bias, calcium disilicide undergoes structural degradation and calcifies via sequence of interfacial reactions similar to biomineralization pathway of Bioglass^{TM}.

1.0.5 Polycaprolactone Tissue Engineering Scaffolds

Polymeric scaffolds have many biomaterial applications, with biodegradable polymers such as polycaprolactone (PCL) attracting extensive attention with regard to tissue regeneration.[2,44] Yet, there exist no pure polymers which can bond to bone *in vivo*.[45] In the field of orthopedics, bone tissue engineering is now commonly accomplished through the use of bioactive glasses and ceramics.[46] Some of the inherent disadvantages of these materials (*e.g.* brittleness in load-bearing applications) can be overcome by fabricating composite polymeric biomaterials. Various resorbable polymers have been used to create such polymer-bioactive glass composite scaffolds, which show improved mechanical and bioactive properties.[47] Although pure bone regenerative polymers which successfully mineralize *in vitro* are also known[5,48] incorporation of an inorganic phase into a polymeric scaffold is still a promising approach. Aside from achieving unique properties, employing an existing bioactive material increases the chances of the novel composites being used in practical clinical applications. Furthermore, since the biological processes that lead to calcium phosphate formation *in vivo* are still under debate, utilizing bioactive glasses for which a biomineralization mechanism has been well established[24] can simplify characterization of a composite material.

Polycaprolactone [$—\{O(CH_2)_5CO\}_n—$] receives less attention in the field of orthopedics due to the lack of functional groups which can be used for surface tailoring. Other polymers, such as poly(lactide-co-glycolide), direct heterogeneous mineral growth through surface carboxylic acid and hydroxyl groups.[48] Recently, Oyane *et al.* developed a facile method for fabricating bioactive PCL scaffolds.[49] In their work, a plasma treatment was used to form oxygen-containing functional groups on the surface of PCL. Subsequently, upon alternate dipping in calcium-ion and phosphate-ion solutions, respectively, these scaffolds became coated with a bone-like apatite layer and are capable of inducing accelerated CaP nucleation and growth in simulated body fluid.[49] Nonetheless, during the fabrication of composite scaffolds, the bioinertness of the PCL matrix is a preferred feature for mechanistic assessment since it allows one to attribute any CaP deposition solely to the incorporated bioactive inorganic phase. As mentioned previously, the preset work demonstrates that $CaSi_2$-PCL composites can readily calcify and degrade *in vitro*, thereby acting as ‘smart’ tissue engineering scaffolds. Furthermore, the presence of semimetallic $CaSi_2$ may potentially extend the applications of such scaffolds to the field of bioelectronics.

1.1 Biomineralization of Synthetic Biomaterials: an Overview

The sheer volume of currently available literature dealing with biomineralization of synthetic biomaterials is overwhelming. This is evidenced by the number of hits (7K+) that come up when the term "biomineralization" is entered into Google Scholar. Yet, it is amazing how little is known about biomineralization mechanisms. Several decades-worth of research focused on calcification of bioactive glasses and ceramics, pioneered by Hench and Kokubo, have advanced these synthetic materials from laboratory bench top to real life medical applications as bone cement or prosthetic implants.[4,46] Other well characterized biomaterials relevant to the field of orthopedics are titania and bioactive silicon, both of which can biomineralize under application of electric bias as well as in its absence.[5,50,51] These are just few synthetic materials whose calcification has been exhaustively studied *in vivo*. The focal point of each study dealing with biomineralization mechanism is nucleation and growth of interfacial layers of calcium phosphate. Needless to say, it is practically impossible to continuously monitor calcification of synthetic biomaterials *in situ* once they have been implanted into a human body. Animal studies can only describe biomineralization progress of an implanted material at discrete points in time but not continuously. Therefore, the majority of mechanistic insights on biomineralization of any biomaterial comes from *in vitro* studies. In particular, the deposition of calcium phosphates induced by a synthetic or modified natural material is most commonly studied in simulated body fluid (SBF), a solution with ion concentrations nearly equal to human blood plasma.[52] As a result, only the first five steps in the formation of bone on the surface of an implant outlined in Figure 1 can be realistically monitored *in situ*, but even then only after a calcium phosphate nucleus has reached a critical size.

For a long time, the deposition of calcium phosphate and its transformation into hydroxyapatite *in vitro* was viewed as a simple electrostatic accumulation of ions, initiated by the attraction of calcium to the surface of a negatively charged synthetic material. It is now known that any calcification pathway is a lot more complex from start to finish, dependent on many factors (*e.g.* surface morphology and functional groups), and in most cases unique to a specific substrate. For now, it is important to understand that none of the existing synthetic biomaterials can reproduce a biological process that leads to the formation of an apatitic mineral *in vivo*, nor establish a calcification mechanism identically duplicated by another synthetic material.[53] It is always necessary to elucidate the biomineralization mechanism of any new biomaterial starting from scratch, using the examples of known mechanisms only as a reference point rather than assigning an established mechanism to a new material based on few similarities.

Bioactive glasses and ceramics are known to facilitate heterogeneous germination of apatitic phosphates *in vitro* and *in vivo*.[22,24,54] Each of these biomaterials has its own signature advantage: the former is resorbable, while the later is more durable than hydroxyapatite (HA) or human bone (see Table 2). As mentioned previously, in 1969 Hench *et al.* developed the first bioactive glass, a melt derived soda-lime-phosphate-silicate glass containing 45 wt% SiO_2, with network modifiers of 24.5 wt% Na_2O and 24.5 wt% CaO and 6 wt% P_2O_5 added to simulate the Ca/P constituents of hydroxyapatite.[23] In 1982 Kokubo *et al.* developed the first bioactive ‘glassceramic A-W’ which contained 38% oxyfluoroapatite [$Ca_{10}(PO_4)_6(O, F_2)$], 34% β-wollastonite ($CaO\cdot SiO_2$), and 28% MgO-CaO-SiO_2 glassy

		Strength (MPa)	
		Compressive	Bending
Bioglass^{TM}		--	42
Glass-ceramic A-W		1080	220
Hydroxyapatite (sintered)		500-1000	115-200
Human bone	Cancellous	2-12	--
	Cortical	100-230	50-150

Table 2. Mechanical properties of bioactive ceramics and human cortical and cancellous bone. Adapted from reference 46.

matrix.[46,55] Thereafter, a variety of bioactive glasses and ceramics were synthesized using the sol-gel process as the favorite synthetic route.[45,56,57] The biomineralization of Bioglass^{TM} and glass-ceramic, as well as of many other less known bioactive materials of similar chemical composition, is induced by functional groups such as Si-OH, Ti-OH, Zr-OH, Nb-OH, Ta-OH, -COOH, and PO_4H_2.[46] A schematic illustration of a model biomineralization process associated with this family of biomaterials is illustrated in Figure 4. During the surface erosion of a bioglass, sodium ion exchange is accompanied by the formation of silica gel which is rich in silanol groups. Calcium is then attracted to the negatively-charged surface, followed by the phosphate ions. Once a layer of amorphous calcium phosphate is deposited, apatite grows by continuing to accumulate ions from the SBF and concurrently crystallize calcium phosphate. Bone ingrowth *in vivo* and apatite formation on bioglasses *in vitro* follow the same biomineralization mechanism.[24] In fact, Kokubo *et al.* recently demonstrated that the *in vivo* bioactivity of these glasses is “precisely” reproduced by apatite-forming ability in SBF.[58] As it was pointed out earlier, animal experimentation, *i.e.* the *in vivo* studies, cannot

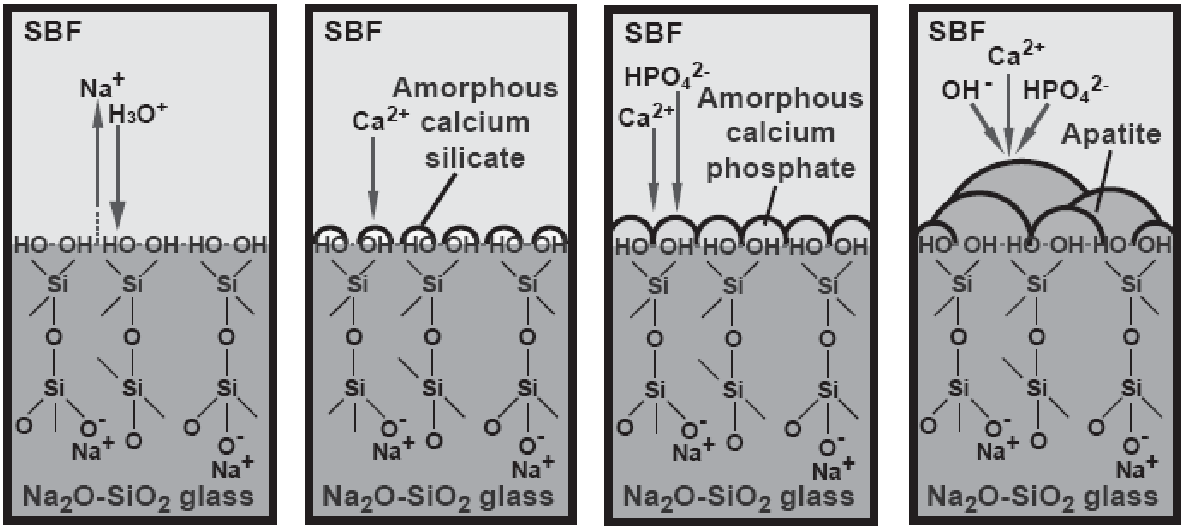

Formation of Si-OH groups

Formation of amorphous calcium silicate

Formation of amorphous calcium phosphate

Formation of crystalline apatite

Figure 4. Mechanism of apatite nucleation on a Na_2O-SiO_2 glass. Adapted from reference 47.

uncover the detailed mechanism of hydroxyapatite-bone interface formation. So, according to Kokubo, “evaluating apatite formation in SBF is [only] a good screening test for the *in vivo* bioactivity of [any] materials, resulting in reduction of the need for animal sacrifices and savings in experimental time”.[58] Issues such as biomechanical loading, physical forces, micromovement at the interface, fluid pressure waves, the related host response or changes which occur at the implant-bone interface ultimately also need to be investigated in joint replacement models in large and small animals.[59]

Bioactivity of a material *in vitro* is usually evaluated by examining calcium phosphate formation on its surface when soaked in acellular simulated body fluid for periods of days to weeks at the physiological temperature of 37°C. A SBF solution is typically prepared by dissolving reagent grade $CaCl_2 \cdot 2H_2O$, Na_2SO_4, NaCl, KCl, $MgCl_2 \cdot 6H_2O$, $NaHCO_3$ and K_2HPO_4 in a buffer of tris(hydroxymethyl)aminomethane and HCl with a final pH of 7.40.[52] This acellular SBF has all ion concentrations nearly equal to those in human blood plasma except that its chloride concentration is higher and carbonate concentration is lower. Standard SBF solution is highly supersaturated with respect to hydroxyapatite and undersaturated with respect to calcite (most stable polymorph of calcium carbonate).[52] During calcification studies *in vitro*, the chemical composition of SBF, the biomaterial substrate surface, *etc.* are rather frequently modified in such way that a particular change in an experimental parameter either provides an insight on the biomineralization mechanism or maximizes the yield of a specific calcium phosphate phase. It is generally accepted that the heterogeneous nucleation of calcium phosphate is induced by various surface hydroxyl groups, and that subsequent growth of apatitic phosphates proceeds by dehydration of the matrix and concurrent substitution of phosphate ions by the CO_3^{2-} ions.[22,24,46,47,60] This carbonate-containing apatite (also naturally occurring) is more soluble than carbonate-free apatite (synthetic only) due to the fact that the Ca-CO_3^{2-} bonds are weaker than the Ca-PO_4^{3-} bonds.[60] As a result, carbonate substituted apatite is more susceptible to acid dissolution which takes places during normal and cancer-induced osteolytic bone destruction by osteoclasts.[61-67]

1.2 Porous Silicon: Fabrication and Biomineralization

The same silicon wafers as those used for constructing elaborate microelectronic integrated circuits began to be viewed in a new light in 1995, when Canham demonstrated the bioactive properties of partially-porosified silicon (BIOPSi).[25] Five years earlier, porous silicon captured the attention of the global scientific community as an optically active material which could possibly be used in optoelectronic applications.[68] When simply immersed in simulated body fluid, BIOPSi readily facilitates heterogeneous deposition of calcium phosphate.[25] The following year, Canham demonstrated accelerated biomineralization of BIOPSi in SBF under bias.[26] Since then, BIOPSi has evolved into patented 'BioSilicon™' (Figure 4) which is currently being investigated in a broad array of biomaterial applications.

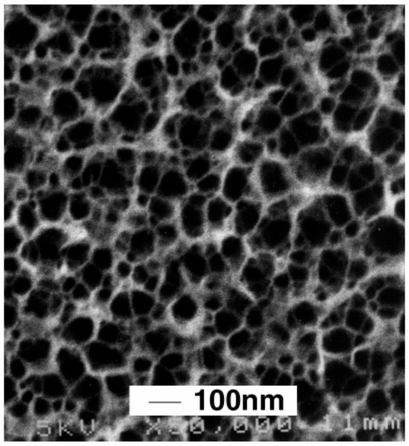

Figure 5. A plan view SEM image of BioSilicon™. Adapted from reference 11.

The biomineralization mechanism of BioSilicon™ has never been discussed in the literature to the same extent as bioactive glasses and ceramics. Porous silicon and Bioglass™

have markedly different chemical compositions, but the process of apatite deposition on their surfaces is rather similar. Bioglasses typically contain at least four components: SiO_2, Na_2O, CaO, and P_2O_5.[24] Calcium and sodium leaching from within the glass assist apatite growth by increasing local Ca supersaturation and locally raising pH, respectively.[24] Yet, as in the case of porous silicon, the nucleation begins with the formation of surface silanol groups (Si-OH). Since SBF solution is slightly alkaline (pH=7.40), it slowly deprotonates these silanols which results in the formation of $Si\text{-}O^-$ groups, accumulation of net negative surface charge, and the subsequent electrostatic attraction of calcium ions from SBF to the bioglass surface. The surface erosion of a bioglass exposes the underlying silica matrix which ultimately results in the formation of hydrated silica gel and the deposition of calcium phosphates, as discussed previously. Formation of hydrated silica gel is an important step in the biomineralization pathway of bioglasses. Furthermore, Kokubo *et al.* have demonstrated that pure silica gel alone can induce deposition of bone-like apatite layer.[69] Silicon, on the other hand, can be made extremely porous (*e.g.* BioSilicon^{TM} is completely resorbable *in vivo*), thereby structurally resembling the hydrated silica gel right from the start.[70] The SBF-exposed Si-Si and Si-H bonds on a microporous (< 50 nm average pore diameter) or macroporous (≥ 50 nm) silicon[71] surface undergo hydrolysis to form silanol groups. Due to the high surface area and small pore diameters, these three-dimensionally arranged silanols create effective nucleation sites for the trapping of calcium ions. The nucleation rate is intimately tied to the local pore structure and morphology. Porosity of a given type of silicon wafers also dictates the rate of the matrix dissolution and the associated release of silicic acid [$Si(OH)_4$], the only byproduct of porous silicon degradation under the physiological conditions.[71,72]

When cathodic bias is applied to a porous silicon wafer electrode immersed in SBF, deposition of calcium phosphate is dramatically accelerated.[25,26,73] Although, SBF is supersaturated with respect to apatite, a newly prepared SBF solution remains precipitate-free for approximately a month in the absence of bias, *i.e.* no spontaneous germination of CaP is expected to take place homogenously in solution. A bioactive surface usually develops a several micrometer-thick calcium phosphate film in a matter of days to weeks.[46] Under the electric bias, however, the same CaP film thickness can be obtained within hours, depending on the magnitude of the applied voltage.[26] Since the deposition process is so quick, the investigation of the biomineralization mechanism under bias is extremely challenging. The as-deposited calcium phosphates can vary in chemical composition, crystal phase, *etc.*, which are dependent not only on the bioactive substrate surface but also on the design and operational parameters of an electrochemical cell. Perhaps the only relatively reasonable mechanistic study of biomineralization in the presence of an electric field may come from experiments similar to the work of Yamashita *et al.* with electrically polarized hydroxyapatite. This group demonstrated the ability to control acceleration and deceleration of heterogeneous bone-like crystal growth by the magnitude of the electrostatic field possessed by ceramic hydroxyapatite produced by electric poling.[74,75]

As mentioned previously, porous silicon finds applications in the field of biomaterials and optoelectronics. Regardless of the intended use, the most common method of porosifying the surface of a silicon wafer is the so called ‘anodic [wet] etch’ route. This process involves the electrochemical reaction between a silicon wafer anode and a hydrofluoric acid based electrolyte.[70,76] The rate of electrochemical dissolution and subsequent oxidation of silicon surface is heavily dependent on concentration of positively changed holes (electron vacancies) within silicon bulk at the electrode-solution interface, *i.e.* the magnitude of the applied anodic bias. Any trace of highly hazardous HF solution needs to be completely removed before such wafer can be used in a biomedical application. Once properly isolated, porous silicon wafers can be implanted *in vivo* directly or after initial pre-calcification *in vitro*.

Taking the additional step of pre-depositing a layer of calcium phosphate on silicon wafer surface not only assures good biocompatibility of a device but also allows one to incorporate various medicinally relevant compounds into the system, particularly if the deposition of calcium phosphate is performed under bias. Xin Li, a previous student in the Coffer group, has developed a method of doping calcium phosphate/porous silicon/silicon structures with platinum anticancer drugs (cis-platin and carbo-platin) and other transition metal complexes, thereby demonstrating the potential use of these porous silicon wafers as drug delivery systems.[77] Some of the experimental work which is presented in this dissertation parallels this research and provides a deeper look on CaP deposition under electric bias. While it is difficult to establish a detailed mechanism for electrodeposition of CaP alone, it is even harder to take into account the presence of an SBF impurity (added drug, *etc.*), which can either accelerate or inhibit the growth process, or predict the behavior of the same system *in vivo*. For example, when cis-platin and carbo-platin were present in the SBF deposition solution, calcium phosphate films, which were deposited on porosified silicon wafers under cathodic bias (1 mA/cm^2), exhibited variation in film thickness and morphology depending on which drug was used.[29] More specifically, under similar electrodeposition conditions thinner calcium phosphate films were produced in the presence of carbo-platin as opposed to cis-platin, supposedly due to the larger Van der Waals volume possessed by the former.[29] The slower rates of nucleation and growth of the calcium phosphate layers in the presence of the larger Pt complex were attributed by the authors to steric inhibition of necessary Ca^{2+} and HPO_4^{2-} diffusion processes.[29] These drug-loaded wafers have not been tested *in vivo* to date. In addition, while studying the effect of thermal anneal on the drug release kinetics associated with transition metal complex-doped hydroxyapatite layers on porous silicon, Coffer *et al.* stated that heating electrodeposited apatite films to just 130°C for 80 minutes can slow down the release of $Ru(phen)_3^{2+}$ by a factor of ten.[28] Here, the authors also suggest that as-formed calcium phosphate (electrodeposited on porous silicon from SBF under the application of 1 mA/cm^2 bias) is not highly crystalline. In fact, their preliminary structural studies suggested that rapid cathodic nucleation gives rise to an amorphous phase, able to convert to a crystalline hydroxy-carbonate apatite over periods of days to weeks.[28] Aside from theorizing that in an annealed sample $Ru(phen)_3^{2+}$ complex is relatively more strongly bound to the apatite, no hypothesis has been offered to explain the effect that such a low temperature thermal treatment has on the electrodeposited calcium phosphate structure.[28]

1.3 Bioactive Silicon Surface Fabrication through Spark-Processing Technique

An alternative to the HF-etch method for porous silicon formation is the 'dry-etch' process developed by Hummel *et al*.[78] As in the case of Canham's BIOPSi, the spark-processed porous silicon was initially intended for optoelectronic applications; however, Hummel has never investigated its bioactive properties, principally because of non-specific protein adsorption on SiO_2. In this dissertation, the spark-processing method was used to fabricate bioactive porous silica and calcium disilicide growth layers on silicon wafers for the bias-assisted area-selective deposition of calcium phosphates *in vitro*.

The spark ablation technique describes formation of a porous silicon layer on a silicon wafer surface under the sustained ablation of silicon wafers with a high-energy

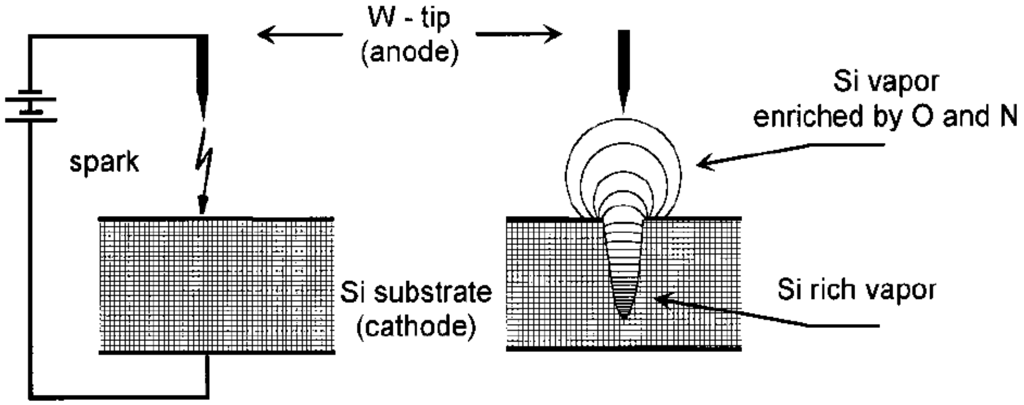

Figure 6. Schematic illustration of spark ablation process. High-voltage direct current pulses cause a discharge between the Si substrate and a tip of the anode. Through impact of accelerated ions from the plasma channel a certain amount of Si is flash evaporated. Taken from reference 78.

electric arc.[78,79] Figure 6 illustrates the spark ablation process as described by Hummel *et al*. This method was later successfully adapted by the Coffer group for kinetic entrapment of diverse chemical species such as rare earth ions and calcium phosphate particles within a surface silica layer which forms when silicon is exposed to a 10kV, low current Tesla coil discharge.[80-82] Here, an electric arc forms between a nickel wire (cathode) and the silicon wafer (anode), which are typically separated by a 3.2 mm air gap. The energy can be controlled by the magnitude of the applied voltage. During spark ablation, silicon on the wafer surface undergoes flash-evaporation and subsequent oxidation by the atmospheric oxygen plasma at the momentary residence of the electric arc. When the arc moves to a different location on the silicon target, the newly formed silica deposits on the eroded wafer surface, eventually forming a porous silica film. Incorporation of impurities into the Si surface (*e.g.* calcium phosphate, $CaSi_2$, *etc.*) occurs when an appropriate precursor is present in the ablation zone. For the deposition of CaP, an acetone slurry is allowed to dry on the wafer surface, and then a high-voltage low-current Tesla coil discharge is used to blast holes in the silicon wafer. Here again, as the spark hits the target, silicon flash-evaporates, quickly oxidizes and comes down as a silica film which entraps calcium phosphate particles.

Coffer *et al.* have also developed an automated spark-ablation apparatus which is capable of making micro-patterns such as the one shown in Figure 7.[82] An alternative spark ablation setup, which avoids the need for re-applying the acetone slurry is shown in Figure 8. Here, the dry calcium phosphate powder forms a plume which does not escape the ablation zone. Unfortunately, both of these methods (with and without acetone) for depositing an interfacial layer of calcium phosphate produce rather non-uniform calcium phosphate films.

Figure 7. Optical micrograph illustrating circular calcium phosphate patterns (0.9 mm diameter) on silicon formed by using an automated spark-ablation apparatus. Taken from reference 82.

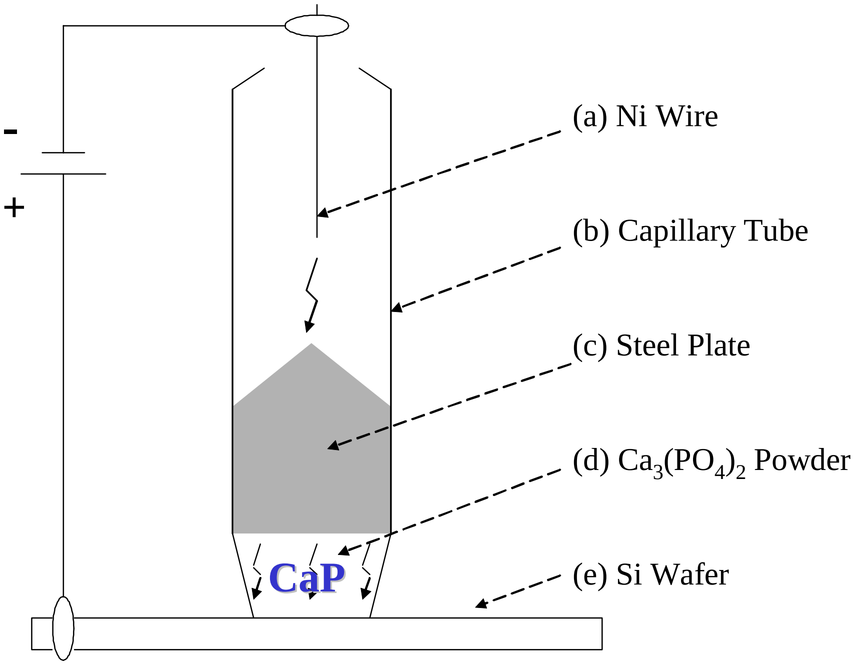

Figure 8. Schematic illustration of a spark ablation method for incorporation of calcium phosphates in Si without acetone slurry.

Part I

CHAPTER II.

Research Synopsis

This dissertation deals with biomineralization of porous silica and calcium disilicide growth layers on spark-processed silicon in the presence/absence of electric bias and the *in vitro* calcification of $CaSi_2$-PCL composite tissue engineering scaffolds. Initial focus involved the use of a dry-etch spark ablation method to produce porous silica (SiO_2/Si) and calcium disilicide ($CaSi_2$/Si) layers on silicon surfaces for the electrochemical growth of apatitic phosphates (CaP). The results of these experiments are described in Chapter 3. Both SiO_2/Si and $CaSi_2$/Si composite electrodes readily calcify *in vitro* under the application of a small electric potential, and with proper treatment the electrodeposition of CaP is localized to the sparked areas. Porous SiO_2 films can also be fabricated via a guided ablation technique and subsequently produce patterns of CaP on Si. In addition to increasing the local concentration of calcium, interfacial layers of $CaSi_2$ on Si exhibit exceptional site-selectivity towards CaP formation under bias due to the difference in conductivity between silicon and $CaSi_2$. The proposed mechanism for bias-assisted biomineralization of $CaSi_2$/Si layers on spark-processed Si accounts for the physicochemical properties of deposited CaP films. Chapter 3 also describes routes to surface modification of calcified composite electrodes with medicinally relevant compounds such as alendronate and norfloxacin. To assess the suitability of this material as a drug delivery platform, release of the latter compound was also monitored as a function of time.

Next, the biomineralization of calcium disilicide layers on spark-processed silicon surfaces under zero bias was analyzed by means of Scanning Electron Microscopy (SEM), X-Ray Energy Dispersive Analysis (EDX), and Raman spectroscopy. $CaSi_2$/Si wafers are bioinert at 25°C and bioactive at 37°C, as assessed by their ability to calcify at these temperatures. Mechanistic insights regarding biomineralization were derived from an analysis of film growth morphology and chemical composition after various soaking periods in standard simulated body fluid (SBF). Changes in $CaSi_2$ calcification behavior as a function of reaction temperature and pH, SBF concentration, and various surface modification processes were also employed for this purpose. During $CaSi_2$/Si calcification under zero bias, calcium phosphate growth is significantly dependent on the structural degradation of $CaSi_2$ grains. Surface silanol groups, initially present on the as-prepared material, cannot induce CaP nucleation; such a process begins only upon delamination of $CaSi_2$ layers. The calcium phosphate phases, which are present during various growth stages, possibly include a combination of Mg-substituted whitlockite, monetite, and tricalcium phosphate.

Finally, in the last chapter, the biomineralization of $CaSi_2$-polycaprolactone composite biomaterials is described. The incorporation of $CaSi_2$ grains within a PCL framework results in bioactive and biodegradable scaffolds which may be ideally used in bone tissue regeneration. Porous PCL scaffolds were prepared via a combination of salt-leaching/microemulsion methods. To provide markedly different structural environments for the inorganic phase, calcium disilicide powder was either added to a mixed-composition porogen during a given scaffold's preparation, or alternatively added to pre-formed PCL sponges. Selective fluorescent labeling, SEM, and EDX were employed to assess the scaffold calcification *in vitro*. The process of $CaSi_2$-PCL calcification under zero bias, during which CaP growth is significantly dependent on the structural degradation of $CaSi_2$ grains, has a similar mechanism as the CaP growth on bioactive glasses/ceramics. The biomineralization of these scaffolds is initiated solely by the silicide phase and can be accelerated by the degradation of the polymer matrix.

Part I

CHAPTER III.

Bias-Assisted *In Vitro* Calcification of Calcium Disilicide and Porous Silica Growth Layers on Spark-Processed Silicon

3.0 Overview

In this chapter, an alternative spark ablation method for the formation of bioactive silicon wafer surfaces is presented. This technique was used to selectively oxidize areas on single-crystal Si to form regions of porous silica (SiO_2/Si). These subsequently act as active growth layers for bias-assisted deposition of apatitic phosphates *in vitro*. The selectivity of bioactive pattern formation was further improved through fabrication of calcium disilicide ($CaSi_2$) growth layers on spark-processed Si. $CaSi_2$ was chosen as an alternative interfacial layer on Si in an attempt to increase local concentration of calcium and thus accelerate the onset of calcium phosphate nucleation. The incorporation of $CaSi_2$ on Si surfaces allows one to form patterned synthetic bone films on silicon chips by taking advantage of the difference in conductivity between silicon and $CaSi_2$. Under electric bias, a bioactive film selectively forms on the more conductive $CaSi_2$ growth layers, which can be deposited in the form of a pattern on semiconducting silicon platforms.

Both SiO_2/Si and $CaSi_2$/Si composite electrodes readily calcify *in vitro* under the application of a small electric potential, and the electrodeposition of apatitic phosphates (CaP) is localized to the sparked areas, while the layer-overgrowth has potential for covering the entire wafer surface with a continuous film. This work also presents routes to surface modification of calcified composite electrodes with medicinally relevant compounds such as alendronate[83] and norfloxacin[84] for potential applications in tissue engineering, drug delivery and biosensing.

Fluorescent tagging of calcium phosphate with fluorescein isothiocyanate (FITC) through alendronate (bisphosphonate amine) linkages was previously used by the Coffer research group in an attempt to develop a biosensor based on a tricalcium phosphate (TCP)-

coated silicon platform.[85] It was determined that TCP, which was entrapped within the silicon surface via a spark ablation technique, was stable and highly emissive when its surface was modified with an alendronate-FITC moiety. The drawback of this method was formation of rather non-uniform TCP-doped films on Si with associated limitations in a reproducible distribution of surface sites. However, such an approach to surface modification of calcified silicon wafers is an excellent model for a biosensor, and the alendronate-FITC coupling reaction was used here to assess the extent of alendronate incorporation.

Norfloxacin is an antibiotic that has been used as a target drug by Stein and co-workers to test the potential of periodic macroporous hydroxyapatite-containing calcium phosphates serving as a drug release agent.[86] They have observed an accelerated release of norfloxacin due to the pores within the three-dimensional network being much larger than the size of this particular drug molecule. The method developed for kinetic entrapment of norfloxacin in the growing $Si/CaSi_2/CaP$ structure, which is presented here, produces drug-loaded semiconducting platforms showing sustained release under zero bias. Norfloxacin is particularly suited for this study since its mechanism of action is known to be positively affected by the presence of Mg^{2+}, which promotes binding of the drug to DNA,[87] and magnesium is unusually abundant in some specific $Si/CaSi_2/CaP$ structures.

3.1 Experimental

3.1.1 Spark-Processing of Si

Pieces (8 mm x 14 mm) of p-type, <100>, boron-doped CZ Si (9-18 Ω cm) were pre-cut by a diamond saw from two Si wafers glued together through their polished sides by vacuum grease or parafilm. In order to obtain a hydrophilic surface, any organic residue was removed prior to sparking through a series of ultrasound assisted sequential immersions in hexane, chloroform, acetone and de-ionized (DI) water. Thereafter, wafers were soaked in a $(NH_4)_2S_2O_8/H_2SO_4$ (conc.) cleaning solution for 12-24 hours until a moment prior to spark ablation, at which point they were removed from the cleaning solution, thoroughly washed with DI-water, and dried under a stream of N_2. The anode was attached to silicon by using Ni wire in a pressure-contact with the side of wafer remote to the sparking location. A second Ni-wire (cathode) was positioned at a fixed distance above the surface of the wafer (sparking

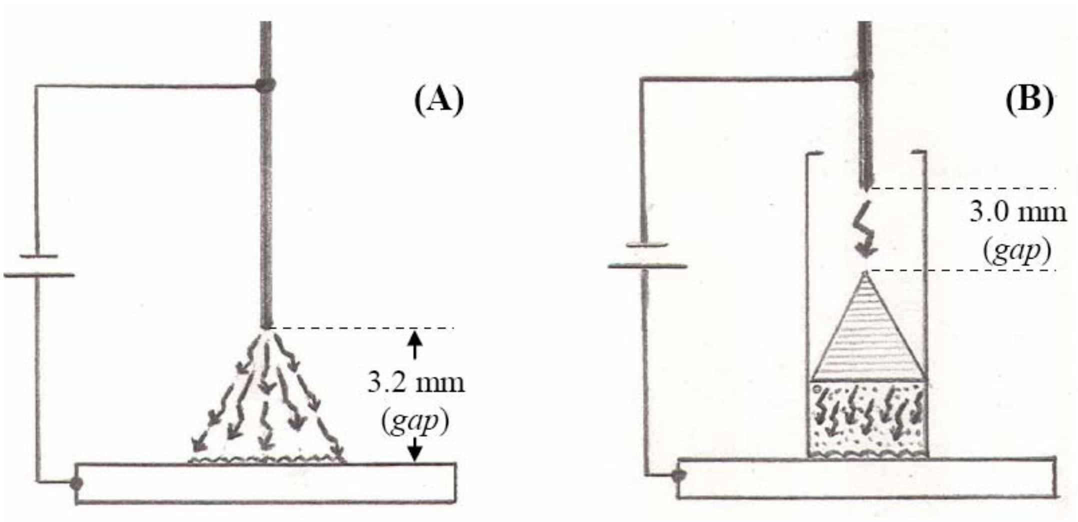

Figure 9. Experimental set up for fabrication of active growth layers on Si via spark ablation: (A) porous SiO_2 and (B) $CaSi_2$.

gap). The sparking setup for porous silica fabrication is shown in Figure 9A. The sparking gap and the ablation time can be varied to achieve desired surface properties (*vide supra*).

The experimental setup for incorporation of $CaSi_2$ is shown in Figure 9B. Here, the Ni-cathode is inserted inside a glass capillary tube (1.2 mm inner diameter), which is partially filled with $CaSi_2$ powder (Johnson Matthey) and pressed against the silicon wafer at the other end. Immediately prior to sparking, the capillary tube was dipped into the $CaSi_2$ powder up to a fixed 6 mm mark and mounted on top of the wafer. A conical steel plate (diameter $\leq$ 1.2 mm) was then inserted inside the tube on top of the $CaSi_2$ powder, and the tip of the cathode positioned at a fixed distance above the plate. The excess powder on the outside was removed by a gentle stream of N_2. Parameters that were varied to achieve optimal silicide incorporation were the sparking gap and duration, while the volume occupied by the $CaSi_2$ powder remained constant.

Upon completion of the sparking events, ether SiO_2/Si or $CaSi_2$/Si wafers were rinsed under a strong focused stream of DI-water to remove any loose particles, and then the samples were dried under a stream of N_2.

3.1.2 Electrodeposition of CaP in SBF

Electrical contact to the back side of SiO_2/Si wafers was made using Ni wire with a mechanically flattened tip and silver epoxy; platinum foil was used as the counter electrode. In case of the $CaSi_2$/Si electrodes, air-oxidation of the silicide film during epoxy-drying time was a concern, and a pressure-contact between the Si and the Ni was designed to allow minute adjustment of the electrochemical cell. First, two slits were cut in a 2-mL polypropylene microcentrifuge tube at a fixed distance from each other. Then, the tube was bent, and a $CaSi_2$/Si wafer was inserted into one of the open slits along with a mechanically flattened Ni wire, which was placed next to the back side of the wafer. When the tube relaxed, a tight pressure-contact was created between the wire and the wafer. The same process was applied to a counter Pt-foil electrode. The electrochemical cell schematic used in CaP deposition is shown in Figure 10. For both SiO_2/Si and $CaSi_2$/Si, the distance of 1.0 cm between the electrodes was held constant during all electrodeposition steps.

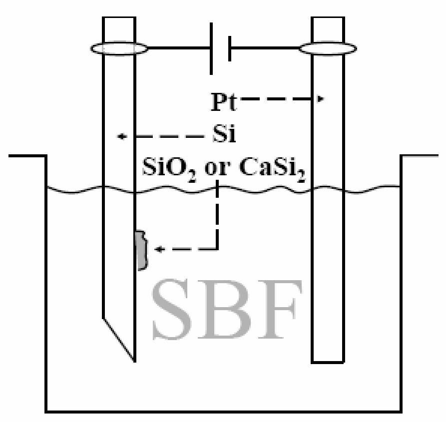

Figure 10. The schematic of the electrochemical cell, which was used in CaP electrodeposition experiments. The bias was applied using Keithley Model 236 source-measure unit.

Electrodeposition reactions were conducted at room temperature. Applied current values and deposition durations were varied systematically to obtain optimal CaP coverage. A SBF solution with ion concentrations nearly equal to those in human blood plasma was prepared from a literature procedure[88] by dissolving reagent grade $CaCl_2 \cdot 2H_2O$, Na_2SO_4, NaCl, KCl, $MgCl_2 \cdot 6H_2O$, $NaHCO_3$ and K_2HPO_4 in a buffer of tris(hydroxymethyl)aminomethane and HCl with a final pH of 7.35 (± 0.5). The corresponding molar ionic concentrations (mM) are as follows: Ca^{2+} 2.5; HPO_4^{2-} 1.0; K^+ 5.0; Na^+ 142.0; Mg^{2+} 1.5; Cl^- 147.8; HCO_3^- 4.2; and SO_4^{2-} 0.5. For a typical electrodeposition event, the volume of SBF electrolyte was 25.00 mL. At the end of the process, when the applied bias was discontinued, samples were taken out, rinsed with DI-water and dried under a stream of N_2.

The stability of calcified SiO_2/Si and $CaSi_2$/Si was evaluated via a 24-hour soak in DI-water at room temperature or a brief exposure to hot DI-water (15-45 min, 75°C). Thermal anneals (30 min, 600°C under N_2) were performed to improve CaP-wafer interface using a Modular Process Technology Rapid Thermal Processor (RTP 610), Tsunami Series. Thermal treatments lasting longer than 2 hours were done in a tube furnace under N_2.

3.1.3 Characterization of Growth Layers

The extent of bias-induced biomineralization of growth layers, *i.e.* the amount of hydroxyapatite deposited on the spark-processed Si surface, was primarily evaluated by means of FT-IR spectroscopy using a Midac system FT-IR with a DTGS detector at a resolution of 2 (or 4) cm^{-1}. The magnitudes of the absorption peaks due to the phosphate stretching (~1030 cm^{-1}) and deformation (~560 cm^{-1}) signature modes in the calcified growth layers served as an estimate of the CaP film uniformity. Similarly, stability of the calcified wafers was evaluated by comparing IR spectra before and after the water soak. The surface analysis was done using a JEOL JSM-6100 Scanning Electron Microscope (SEM) coupled with an Energy Dispersive X-Ray (EDX) Analysis detector under an accelerating voltage of 20 kV.

3.1.4 Surface Modification of CaP

Coupling reactions between CaP and alendronate, $(H_2O_3)_2C(OH)(CH_2)_3NH_2$,[89] were performed either by immersing as-prepared calcified $CaSi_2$/Si wafers in 2.0 mL aliquots of alendronate aqueous solution (5.0 mM) or by adding 2 mL of the same alendronate solution to SBF during electrodeposition of CaP. The latter method, herein referred to as “kinetic entrapment,” implies a two stage reaction: CaP electrodeposition from a standard SBF solution first, followed by the secondary growth stage in the alendronate-charged SBF. After alendronate exposure, samples of both types were washed with DI-water and dried under a stream of N_2. The extent of alendronate coverage was evaluated via fluorescence measurements performed on fluorescently labeled samples using a Nikon Optiphot-2 fluorescence microscope with a Santa Barbara Instruments Group CCD and an Ocean Optics S2000 fiber optic spectrometer. Coupling reactions with the fluorescent tag, fluorescein isothiocyanate (FITC, λ_{em}=520 nm), were performed as simple immersions of the corresponding wafers in 2.0 mL aliquots of 1.0 mM FITC solution in DMSO/H_2O (2:5) in the dark at 4°C. The duration of FITC exposure was typically 12 hours. Prior to fluorescence detection, the wafers were washed with DI-water and dried under a stream of N_2.

Similar to the kinetic entrapment of alendronate, norfloxacin was introduced into the SBF during the second stage of CaP electrodeposition by using 2.0 mL of aqueous norfloxacin solution (10.0 mM) per 25.0 mL of standard SBF. The solubility of norfloxacin (acid form, Aldrich) in water was achieved by adding 0.1 M NaOH dropwise until the salt was completely dissolved. After the electrodeposition process was complete, the wafers were washed with DI-water and dried under a stream of N_2. Prior to norfloxacin release experiments, excess CaP was physically removed from non-silicide containing wafer electrodes to ensure that calcified $CaSi_2$ growth layers were the only source of the released norfloxacin. This step was necessary to get rid of the overgrowth layers, which otherwise can be removed by a 24 hour water soak (*vide supra*). The wafers were then again washed with DI-water and dried under stream of N_2. Norfloxacin release was monitored by measuring the absorbance of the release medium (SBF) at 274 nm, using a Hewlett-Packard 8452A diode array spectrometer. A calibration curve was obtained using solutions of known concentration.

3.2 Results

3.2.1 Active Growth Layer Fabrication: Porous Silica Films

During spark ablation, the silicon wafer surface undergoes flash-evaporation and subsequent oxidation by the atmospheric oxygen plasma at the momentary residence of the electric arc. When the arc moves to a different location on the silicon target, the newly formed silica deposits on the eroded wafer surface, forming a porous silica film. An experimental setup for silica deposition via spark ablation is shown in Figure 9A. The optimal 3.2 mm air gap between the wafer and the Tesla coil sets the limit on the wafer area subjected to the ablation. When the gap distance is held constant, the electric arc moves through a path of minimal resistance; therefore, when an area of a silicon anode becomes covered with a layer of insulating silica, the arc changes location. Since the motion of the arc is random, the final porous silica film is circular, and it is centered directly below the nickel cathode. A SEM image of a typical silica sample (3.2 mm gap, 50 min duration) used in subsequent calcification studies is shown in Figure 11. The sparked layer extends 10-15 μm

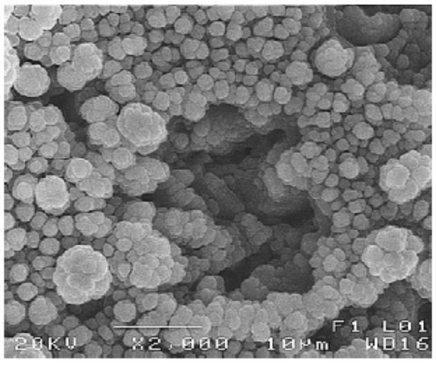

Figure 11. A plan view SEM of a porous SiO_2 growth layer on spark-processed Si produced under optimal sparking conditions: 3.2 mm gap and 50 min duration.

into the crystalline substrate, and its surface is composed of irregular holes surrounded by nonuniform clusters of SiO_2.[81] As the duration of the sparking event governs the uniformity and thickness of the resulting silica, the optimum ablation time period was determined experimentally and ultimately evaluated with regard to the quality of the final electrodeposited hydroxyapatite film. For a constant 3.2 mm air gap, durations of spark ablation under 45 minutes resulted in non-uniform silica films; ablation periods lasting greater than 50 minutes produced thicker insulating silica films which, in turn, adversely affected the electrochemical growth of CaP.

3.2.2 Active Growth Layer Fabrication: Calcium Disilicide Films

When crystalline $CaSi_2$ grains are placed on top of the silicon anode and in the path of the electric arc, $CaSi_2$ is kinetically trapped within the porous silica layer. The high temperature plasma generated at the wafer surface facilitates rapid oxidation of the entrapped grains as evidenced by the abrupt color change of the starting silicide. Since the spark is able to propagate freely through the adjoined grains of the metallic $CaSi_2$, the resulting pattern is no longer a circle as in case of porous silica films. Furthermore, the turbulent environment created during wafer surface erosion causes local movement of silicide grains, which in turn adds to the formation of an ill-defined pattern. Figure 9B depicts the experimental setup for calcium disilicide deposition via spark ablation, which is designed to produce uniform circular films with limited oxidation to the surface-entrapped grains of $CaSi_2$. The electric arc, whose motion is now confined to the inner diameter of a glass capillary tube, propagates through multi-layers of randomly stacked $CaSi_2$ grains. The weight of the conical steel plate inserted on top of the $CaSi_2$ powder applies pressure which reduces overall turbulence and prevents the escape of the grains during the spark ablation. In addition, as the spark leaves the base of the cone, its vertical motion is relatively uniform throughout the cylindrical body of $CaSi_2$ powder, assuming negligible resistance of steel compared to the air-gap between the cathode and the top of the conical plate. Finally, while the upper part of the $CaSi_2$ volume is rapidly oxidized, the grains in the bottom layer of the capillary retain their physical appearance. The resultant $CaSi_2$ is not measurably oxidized, as the FT-IR spectrum of the final material is unchanged with regard to the Si-O peak intensity at ~1100 cm^{-1} (relative to the native oxide of the wafer). Figure 12 demonstrates the effect of varying the duration of spark ablation and the energy of electric arc on $CaSi_2$ film morphology; continuous and more

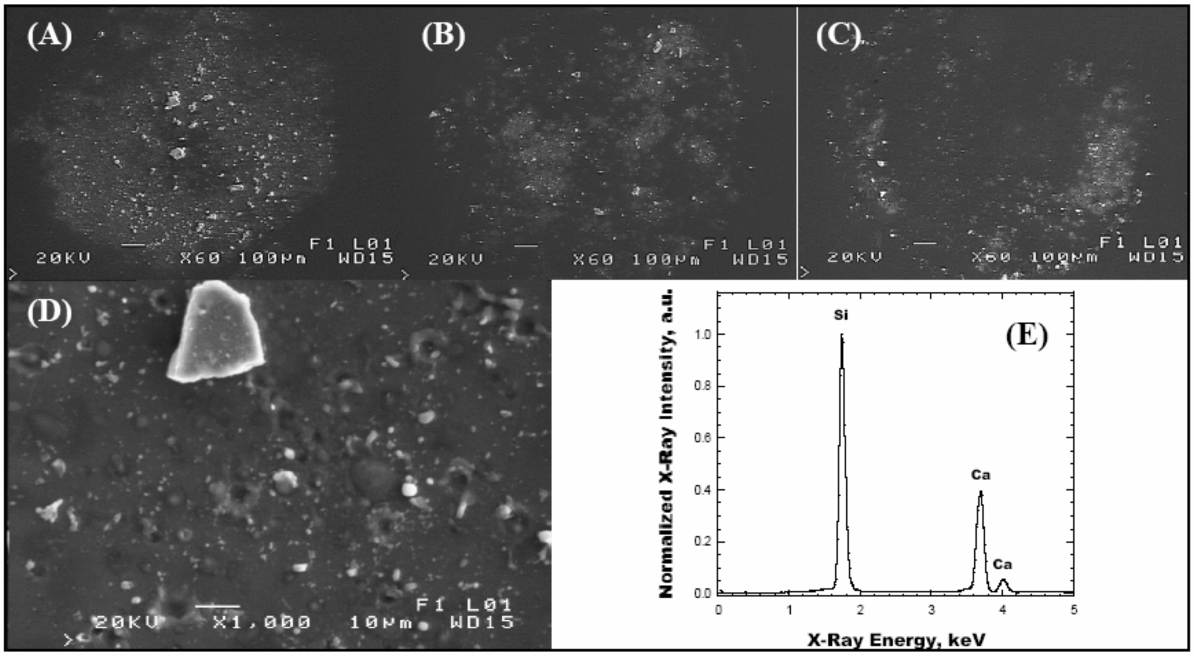

Figure 12. Plan view SEM of a $CaSi_2$ growth layers on spark-processed Si produced under various sparking conditions: (A) *optimal* 3 mm air gap and 900 sec duration, (B) 3 mm gap & 300 sec duration, (C) 1 mm gap & 900 sec, (D) magnified view of (A) showing a $CaSi_2$ grain & hole-like valleys, and (E) the EDX spectrum associated with $CaSi_2$ grain in (D).

uniform films are favored by longer deposition times and larger sparking gaps (Figure 12A). Note the two types of structural features: Ca^{2+}-rich valleys and $CaSi_2$ grains [1-10 μm] (Figure 12D). EDX confirms the presence of calcium and silicon at these respective locations. Beneath the surface of the silicon wafer, the $CaSi_2$ growth layer extends up to 2 μm deep as assessed by cross-section SEM measurements. As in the case of porous silica films fabrication, the optimum conditions for spark processing were determined experimentally and were ultimately evaluated with regard to the quality of the final electrodeposited hydroxyapatite film. For the constant volume occupied by $CaSi_2$ powder and the length of the steel plate, the optimum separation of Tesla coil electrodes is 18 mm, which translates into a 3 mm air-gap between the cathode and the top of the conical plate. For this optimal configuration, standard spark ablation experiments lasted 15 minutes. The upper limit is determined by the rate of $CaSi_2$ oxidation and subsequent loss of conductivity, which, in turn, affected the electrochemical growth of CaP.

3.2.3 Electrochemical Growth of CaP on Porous Silica Films

During the electrochemical growth of hydroxyapatite on the composite SiO_2/Si electrode from SBF, there are three major areas on the wafer that compete to serve as CaP nucleation sites: (i) porous silica thin-films produced by spark ablation, (ii) the polished wafer surface around the sparked region, and (iii) the wafer edges. While the nature of the competition is complex, the major prioritizing factor is local surface conductivity which varies throughout the electrode. If the magnitude of the applied current is under 0.89 mA/cm^2 (assuming the current flow primarily through the Si wafer), it is evident that the wafer edges are the most reactive, partly because of the thinner layer of insulating native oxide present on the freshly scribed silicon and partly due to the multiple crystal surfaces exposed during the wafer cutting process. The ablated silica surface is the least conductive and does not accommodate hydroxyapatite formation if the applied current is less than 0.89 mA/cm^2; when 0.9 mA/cm^2 or higher currents are used, the site selectivity is reduced, and all three areas participate in the nucleation process. Since the SBF solution is already saturated with respect to calcium phosphate, as the electrodeposition progresses, the wafer edges become shielded by a cloud of colloidal CaP, which begins to form spontaneously in solution in the path of ionic current, and the deposition at the remaining two sites is relatively accelerated. Eventually, this CaP cloud presumably inhibits further deposition at any location on the wafer since any deposition duration beyond 4 hours did not result in the significant increase of the final CaP concentration, as assessed by FT-IR measurements. Note that at this magnitude of applied current, the corresponding voltage is 5.5±0.5 volts, but the hydrogen formed upon water electrolysis does not have a pronounced effect on the system; application of larger current values causes rapid bubbling along the silicon surface, thereby disturbing the colloidal CaP, which results in the perturbation of film growth.

The extent of bias-induced biomineralization of porous silica growth layers, *i.e.* the amount of hydroxyapatite deposited on the ablated silica surface, was primarily evaluated by means of FT-IR spectroscopy. The magnitudes of the absorption peaks due to the phosphate stretching (~1030 cm^{-1}) and deformation (~560 cm^{-1}) signature modes in the calcified silica growth layers serve as an estimate of the CaP film uniformity. Shown in Figure 13 are the FT-IR spectra of calcified silica layers from multiple samples prepared under identical sparking (3.2 mm gap, 50 min. duration)/ electrodeposition (4 hr duration, 0.893 mA/cm^2 applied current) conditions and the average post-ablation spectrum from the same wafers

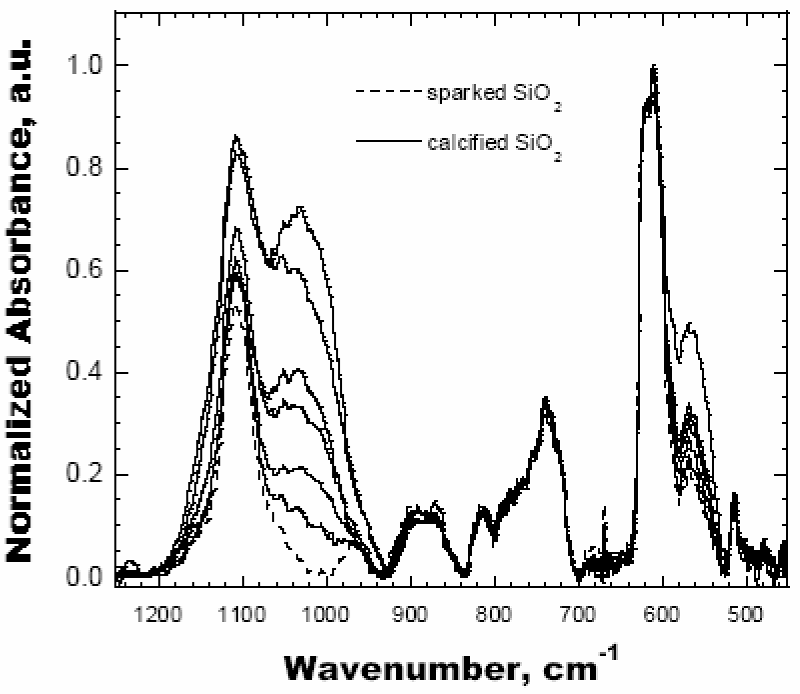

Figure 13. FT-IR spectra of six calcified SiO_2 growth layers on spark-processed silicon, fabricated under the same *optimal* conditions: 3.2 mm gap & 50 min sparking duration and 0.893 mA/cm^2 & 4 hr electrodeposition duration, and an average FT-IR spectrum of as-prepared SiO_2/Si. All spectra are normalized with respect to Si peak intensity.

immediately prior to SBF exposure. It is evident that under the influence of electric bias, SiO_2/Si surfaces readily induce formation of hydroxyapatite, but the large variation in CaP film uniformity between samples calls for careful optimization of experimental parameters. Note that during FT-IR measurements, care was taken to obtain the absorbance of the sparked areas only; therefore, contribution of the CaP overgrowth layer on polished wafer surface around the sparked region can be excluded. Separation of the porous silica-based CaP from the overgrowth layer on polished surface was rather straightforward as the perimeter of the ablated silica region was constantly surrounded by a circle of polished silicon devoid of CaP (see Figure 14). This lack of CaP growth is attributed to an electrohydrodynamic effect (*vide supra*).

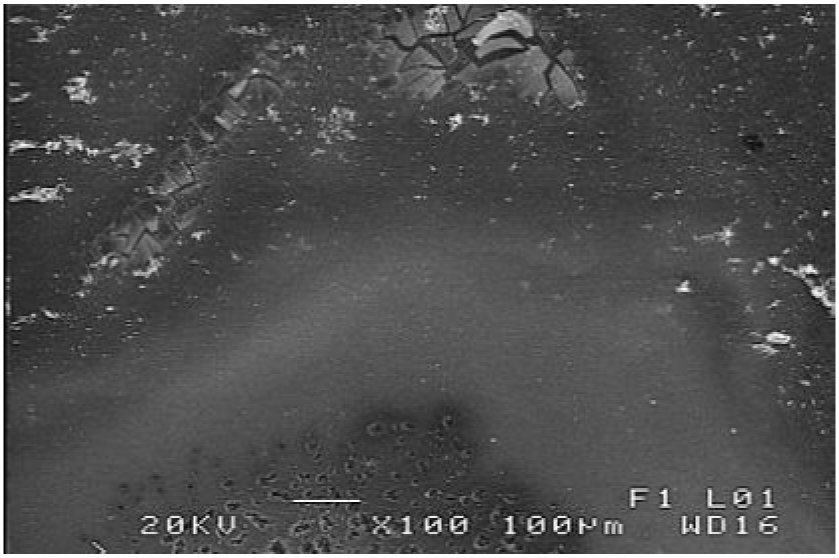

Figure 14. A plan view SEM of a part of the perimeter around a calcified SiO_2 growth layers on spark-processed silicon, devoid of CaP due to an electrohydrodynamic effect. The weakly bound CaP film seen on polished silicon surface beyond this circle can be easily removed as discussed in the text.

The stability of the final CaP film and the wafer interface is governed by the surface morphology and the silica surface hydroxyl group concentration. Therefore, the porous silica region is expected to have the most stable CaP film; however, a 24 hour soak in deionized water removes CaP from the entire electrode. When the electrodeposition was followed by a thermal anneal (30 min, 600°C), the interfacial stability was improved and the CaP film on the ablated silica surface survived the water exposure for three days, while the rest of the wafer surface was relieved of CaP. Such an approach results in the fabrication of apatite-coated silicon where the site selectivity for CaP presence is governed by the location of the sparking event.

3.2.4 Electrochemical Growth of CaP on Calcium Disilicide Films

As in the case of SiO_2/Si material, there is a preferred order of nucleation site selectivity for the $CaSi_2$/Si wafer electrodes. The inherent conductivity of metallic $CaSi_2$ causes rapid and selective deposition of CaP on the ablated region right from the start of the electrochemical growth process. As the reaction progresses, the wafer edges and the polished wafer surface surrounding the ablated region begin to participate in CaP deposition and eventually develop a cloud of colloidal CaP similar to SiO_2/Si electrodes. Nonetheless, CaP that deposits here is loosely bound to the wafer surface through available Si-OH groups and can be easily removed by the 24-hour deionized water exposure as described previously. Surprisingly, stability of the CaP films on the $CaSi_2$ growth layers is significantly higher compared to the porous silica growth layers as assessed by film delamination in H_2O, and the thermal anneal, which improves the CaP-wafer interface, was not required prior to the water soak. Overall, control over electrochemical reaction kinetics through the superior conductivity of $CaSi_2$ allows one to achieve relatively quick and site-selective biomineralization of silicon wafers under bias. In order to determine the mechanism of CaP electrodeposition on $CaSi_2$ growth layers, the experimental system was further optimized in attempt to localize CaP formation exclusively on the sparked pattern. Gaining better control over the selective nucleation and growth of CaP on the patterned silicon electrodes will become crucial during device miniaturization and its eventual operation *in vivo*.

Formation of the colloidal CaP cloud, which had a beneficial effect on the biomineralization of porous silica growth layers through shielding of the wafer edges, has a negative effect on the $CaSi_2$/Si system as it promotes deposition of weakly anchored CaP on the polished wafer surface and reduces growth selectivity towards the sparked pattern. Its effect on the CaP growth kinetics can be minimized by milling of the wafer edges with sandpaper and then polishing with 0.5-μm alumina powder prior to $CaSi_2$ incorporation as depicted in Figure 15. Such treatment decreases the number of morphological surface defects, thus discouraging physisorption of CaP particles involved in the growth of the colloidal cloud next to the wafer electrode. Subsequently, for a typical electrodeposition event, the absence of the CaP cloud shielding effect is sustained over a 2 to 4 hour period. During this time the conductivity of the active growth sites on the wafer surface is decreased primarily due to $Si/CaSi_2$ oxidation and to the appearance of apatite films. Minor CaP deposits on the wafer edges can be easily removed by a brief exposure to hot DI-water (15-45 min, 75°C), while the calcified $CaSi_2$ film is preserved. This new silicon/$CaSi_2$/CaP structure is stable and survives a 24 hour DI-water soak without the need for a preliminary thermal anneal. However, when these wafers were used in the drug incorporation/release experiments, an anneal was proven to be necessary as the slightly alkaline SBF (or a drug solution itself) facilitates $CaSi_2$/CaP film delamination from silicon.

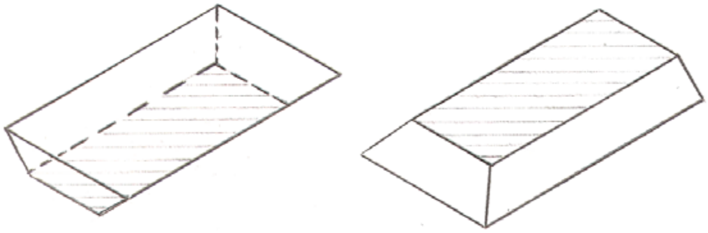

Figure 15. Schematic illustration of a milled and polished Si wafer.

The growth of the CaP on the polished wafer surface can be nearly eliminated by decreasing the magnitude of the applied current. Shown in Figure 16 are the FT-IR spectra of the calcified $CaSi_2$/Si films fabricated under variable bias conditions. The intensities of the

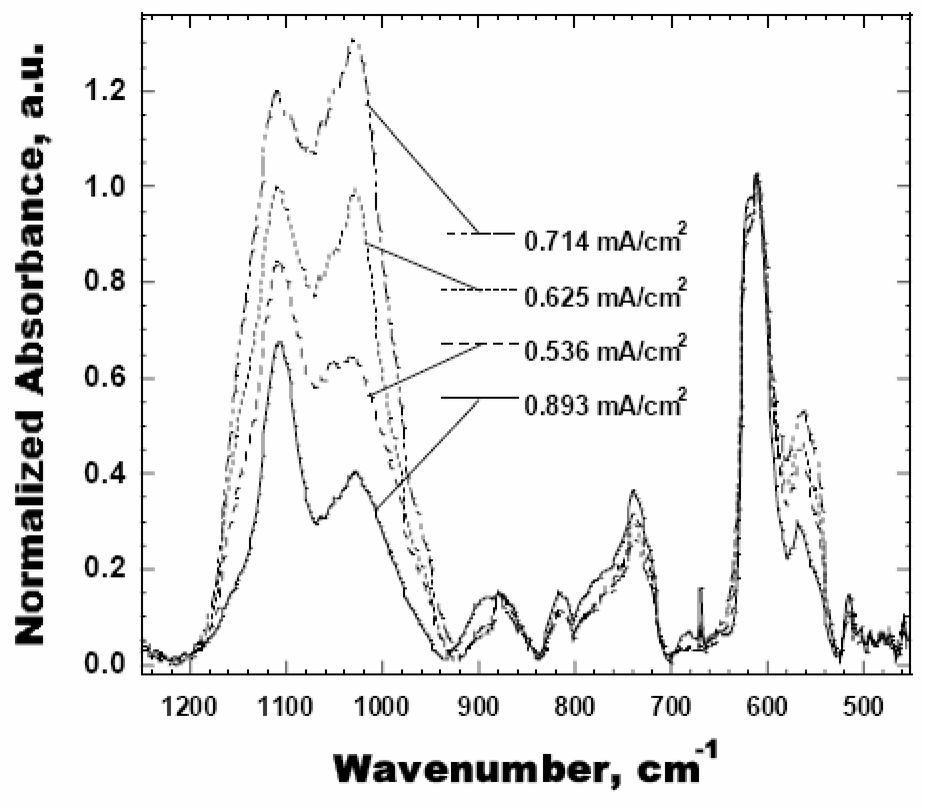

Figure 16. FT-IR spectra of calcified $CaSi_2$ growth layers on spark-processed Si fabricated under various electric currents. All spectra are normalized with respect to Si peak intensity.

peaks at ~1030 cm^{-1} due to the P-O stretch signify the amounts of CaP present on the sparked patterns. As the figure illustrates, the optimum value for the applied bias is 0.714 mA/cm^2. Application of larger current values causes non-selective deposition of CaP on the polished wafer surface which now competes with $CaSi_2$; smaller currents slow down the reaction kinetics and result in poor CaP coverage for the same duration of the electrodeposition. In the majority of experiments with optimal reaction conditions, the polished surface of Si electrode was completely free of CaP, which could only be found at the wafer edges and on the $CaSi_2$ growth layer. However, in some instances CaP deposited directly above the sparked area in the form of a strip. When loosely bound CaP particles detach from the $CaSi_2$ growth layer, they are carried upward by the surfacing hydrogen bubbles. Some of these particles get trapped by the wafer surface defects and subsequently act as secondary growth sites for CaP. Although this undesired CaP is easily removed by the water soak, the sheer occurrence of such a strip can be prevented by slightly tilting the electrode ~5 degrees from the vertical such that the polished surface is directed upwards.

Typical CaP structures formed on $CaSi_2$ growth layers via electrodeposition from simulated body fluid exhibits two common morphological features. Thin plate-like films comprised of spherulites with diameters ranging from 1-5 μm are shown in Figure 17A;

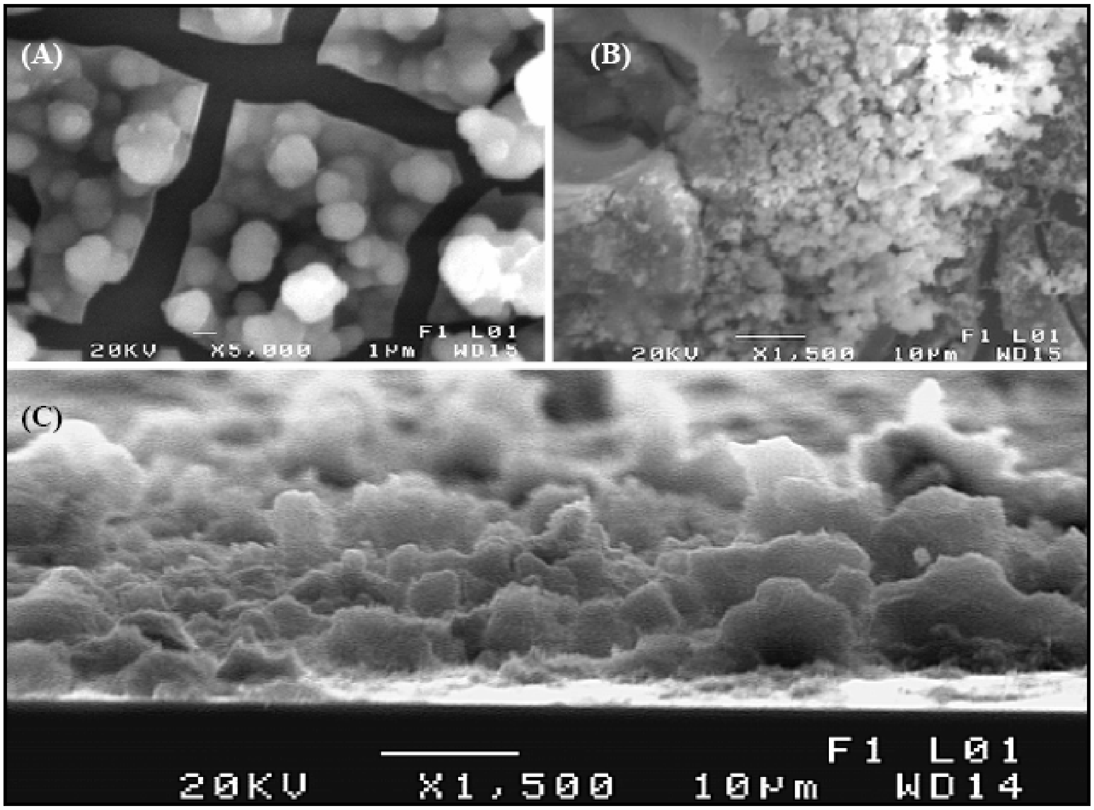

Figure 17. Plan view SEM of typical CaP structures formed on $CaSi_2$ growth layers via electrodeposition from SBF: (A) platelets & spherulites, (B) large porous structure, and (C) tilted view SEM of the wafer surface.

cracking of continuous films under rapid drying conditions (or evacuation of the SEM chamber) results in the formation of isolated platelets. Large porous structures are found less frequently and typically reach ~10 μm in height above the wafer surface. Figure 17B shows an example of such a structure. It appears to be made up of smaller calcium phosphate particles than the platelets and is expected to possess high surface area. A tilted view of the wafer surface shown in Figure 17C indicates that CaP films supply a uniform coverage of sparked patterns and should be ideal for tissue bonding if implanted *in vivo*. A typical EDX spectrum associated with calcified Si/$CaSi_2$ films is shown in Figure 18. The elements present (Ca, Mg and P) are native to naturally occurring apatites.[22] Occasionally, peaks

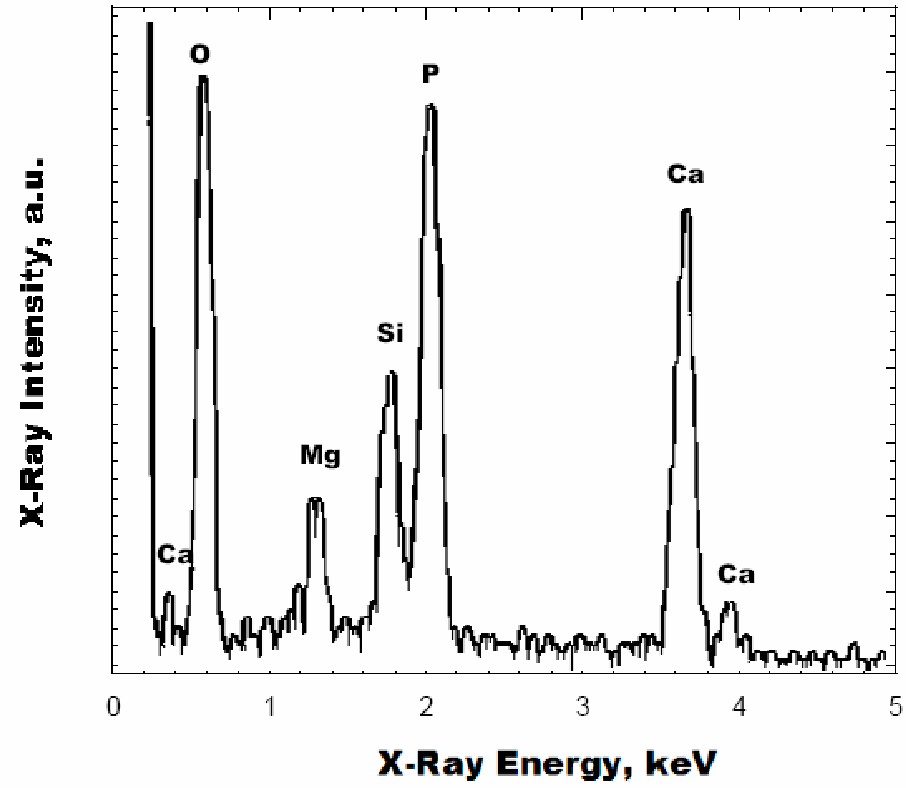

Figure 18. A typical plan view EDX spectrum of calcified $CaSi_2$ growth layers on spark-processed Si.

arising from other SBF constituents (such as sodium, chlorine and sulfur) were identified in EDX spectra, but usually their concentration is close to EDX detection limits. Note that the routinely used EDX instrument is equipped with a beryllium window, and as a result, carbon is not detectable, but the presence of carbonate is confirmed by FT-IR. In addition, no areas on these wafers were located indicating only the presence of calcium and silicon via EDX, which suggests that the original $CaSi_2$ layer had been completely covered by CaP. The thickness of deposited CaP layers (obtained from the optimal sparking/electrodeposition conditions) ranges between 1 and 10 μm throughout the sparked pattern. A cross-sectional SEM image in Figure 19 shows an average 3 μm-thick CaP film on the surface of a $CaSi_2$ growth layer and the deformation of silicon due to the spark ablation extending 2 μm beneath the surface of the wafer.

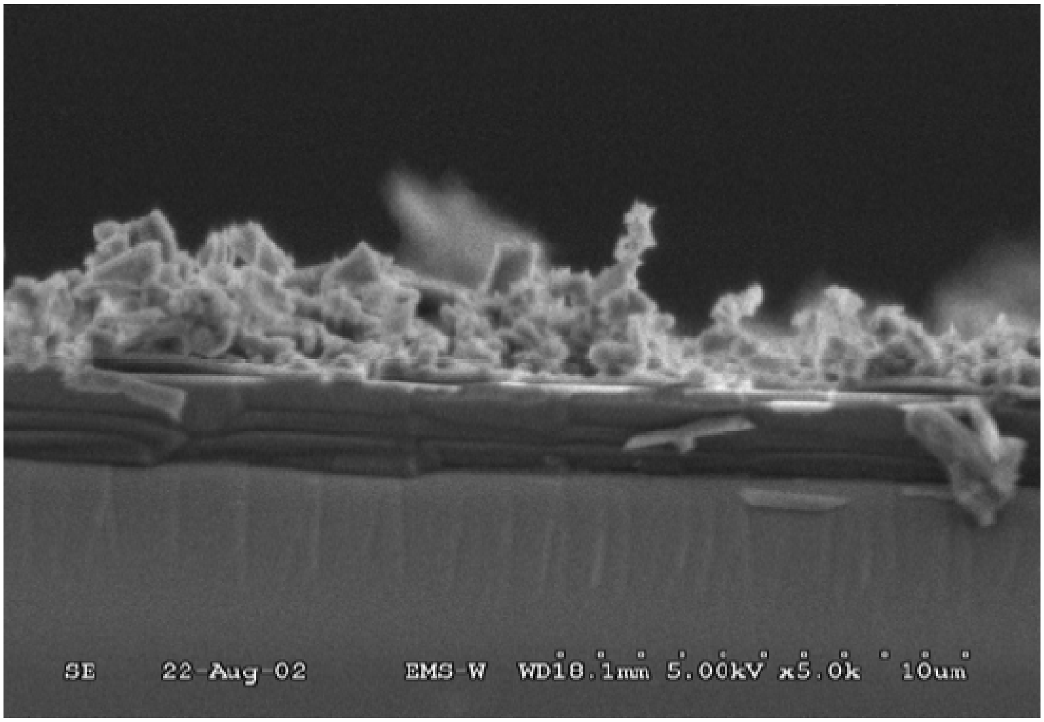

Figure 19. A typical cross-section SEM of calcified $CaSi_2$/Si wafer.

Aside from these commonly found morphological and compositional features of electrodeposited CaP films, one can frequently observe CaP structures, which are magnesium-rich and possess a different surface morphology, present on the calcified $CaSi_2$/Si film. The film shown in Figure 20 closely resembles magnesium-substituted whitlockites [or magnesium-substituted tricalcium phosphate (β-TCMP): $[Ca, Mg)_9(PO_4)_6]$.[22]

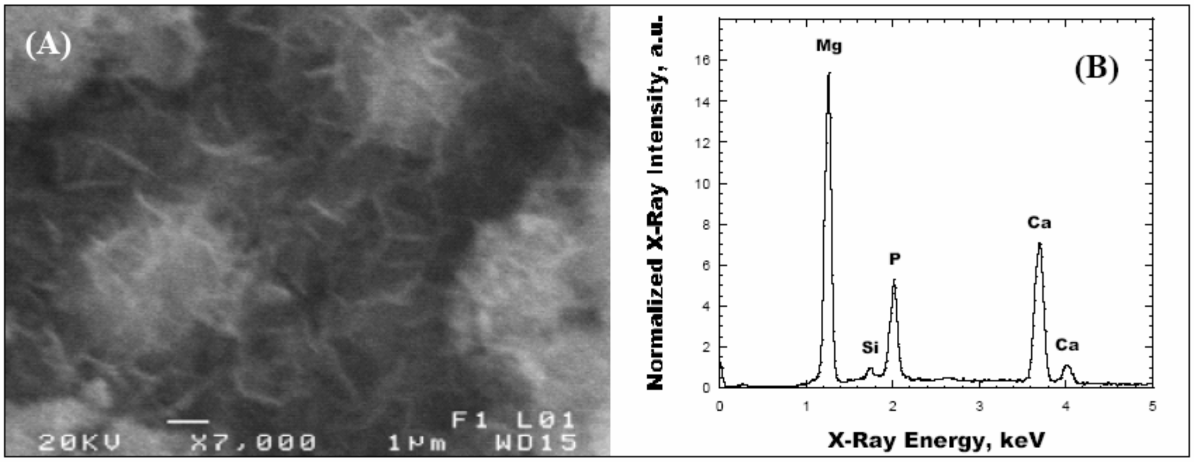

Figure 20. Magnesium-rich CaP structures frequently found on calcified $CaSi_2$/Si electrodes: (A) plan view SEM and (B) the EDX spectrum associated with (A).

These are not expected to form under physiological conditions,[22] yet formation of whitlockite in SBF was recently suggested by Vallet-Regi based on XRD patterns of calcified SiO_2-CaO-P_2O_5-MgO sol-gel glasses.[90] In addition, it was not uncommon to find structures which were morphologically similar to this Mg-rich CaP but lacked a phosphorous signature in their corresponding EDX spectra. The film shown in Figure 21 appears similar to calcium carbonates prepared by Mann *et al.* from bicontinuous microemulsions.[91] Since no XRD data were obtained, it is unclear if these deposits are, in fact, a mixture of $CaCO_3$ and magnesite ($MgCO_3$), Mg-substituted calcite [$(Ca_xMg_y)CO_3$], dolomite [$CaMg(CO_3)_2$] or some other combinations.

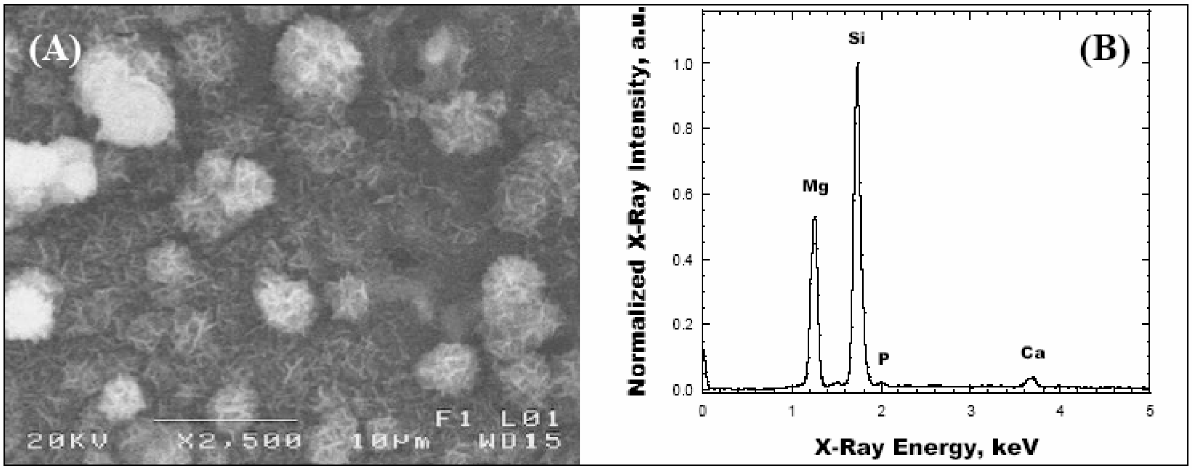

Figure 21. Magnesium-rich phosphorous-deficient CaP structures frequently found on calcified $CaSi_2$/Si electrodes: (A) plan view SEM and (B) the EDX spectrum associated with (A).

The phenomenon of CaP particle migration along the silicon wafer surface and their incidental deposition in the form of a strip above the sparked $CaSi_2$ area, described previously, was used to indirectly infer the role of magnesium during bias-assisted calcification of $CaSi_2$ growth layers. In particular, it was contemplated that high magnesium content reflected formation of Mg-substituted calcite at the early stage of CaP growth. For this purpose, a porous silica pattern (see Figure 22) was fabricated above the $CaSi_2$ area via the ablation technique under manual spark guidance. When such patterns are deliberately created on the wafer surface above the $CaSi_2$ growth layer, they serve as efficient traps for CaP particles which are being carried upward by the surfacing hydrogen bubbles along the

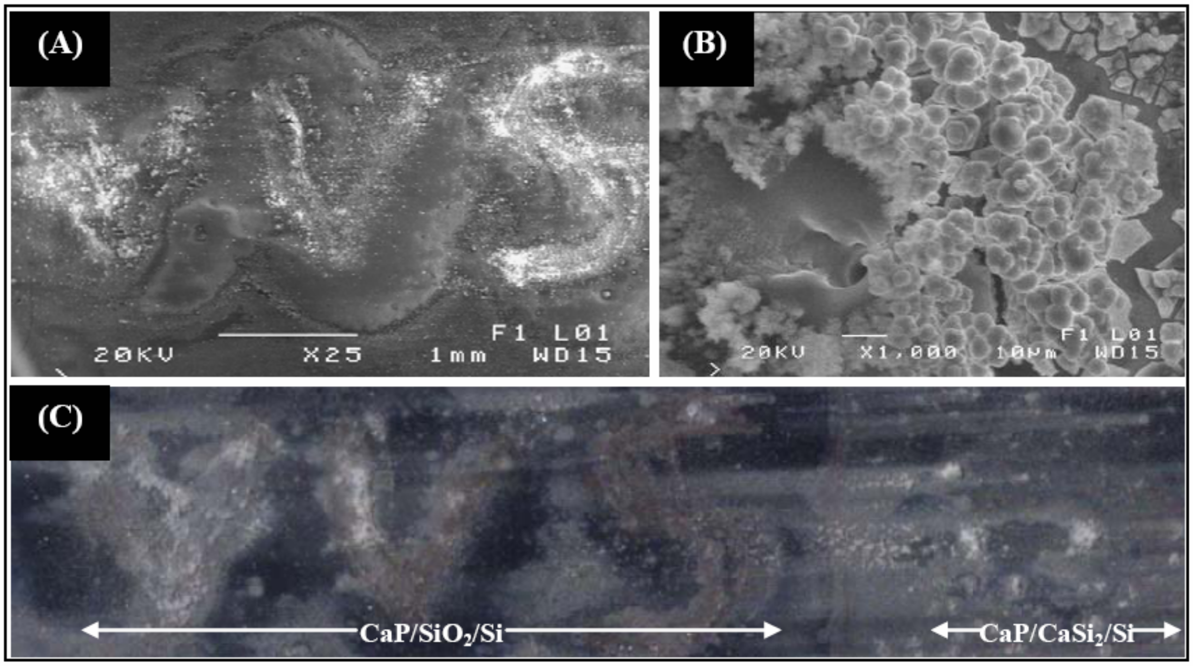

Figure 22. Calcified porous SiO_2 pattern on spark-processed Si produced under manual spark guidance above $CaSi_2$ growth layer: (A) plan view SEM of calcified SiO_2/Si, (B) magnified view of an area in (A) located 1 mm away from $CaSi_2$, and (C) optical image of the entire spark-processed area on Si.

vertically positioned silicon electrode. The process is sequential, *i.e.* depending on the distance from the $CaSi_2$ area, different parts of the silica pattern trap CaP particles which were formed at different stages of CaP nucleation and/or growth and later detached from the $CaSi_2$ area. These secondary growth sites imitate retarded CaP growth kinetics compared to $CaSi_2$, since the local surface conductivity at porous silica sites is significantly lower. Once formed under rapid nucleation conditions at the silicide area, a CaP particle, trapped at the porous silica region, undergoes much slower growth. The EDX spectra obtained from different locations on CaP film, which formed on this porous silica pattern, are shown in Figure 23. The magnesium content of the film gradually increases up along the wafer

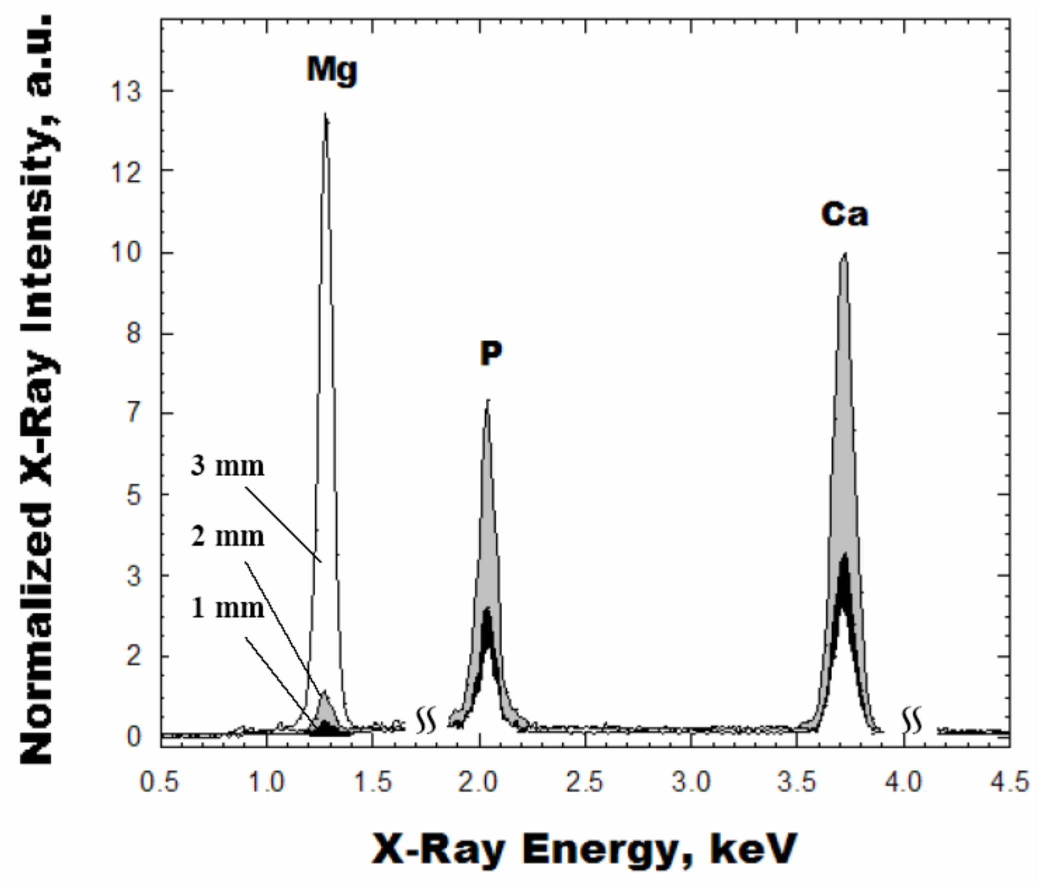

Figure 23. Plan view EDX spectra of selected areas on calcified SiO_2 pattern located at various distances above the $CaSi_2$ growth layer: 1 mm, 2 mm, and 3 mm. All spectra are normalized with respect to Si peak intensity.

beginning with the vicinity of $CaSi_2$ and peaks at the farthest location from the $CaSi_2$ area (see Figure 22C). Associated SEM images (not shown) exhibit a surface morphology consistent with previous observations of Mg-rich CaP (see Figures 20&21). Note that the calcified porous silica growth layers discussed earlier were never found to be unusually rich in magnesium. This indicates that high magnesium incorporation is related to $CaSi_2$ growth layers and occurs at the early stage of electrochemical growth of CaP.

In addition, the formation of magnesium-rich apatite was also observed in the events when CaP was electrochemically grown on already calcified Si/$CaSi_2$ samples. The surface of the initial CaP film, which was altered by either thermal anneal, exposure to electron beam of the SEM, or by attachment of calcium-binding drugs, presumably causes a secondary nucleation to occur rather than instantaneous growth of CaP. The SEM/EDX analysis of these double-layer samples indicated a magnesium-rich phase. The Mg content was higher compared to those Si/$CaSi_2$ samples which were allowed to calcify uninterrupted for the same period of time. Thus, the proposed mechanism for bias-assisted biomineralization of $CaSi_2$ in SBF discussed in Section 3.3.2 explains this presence of magnesium in terms of its effect on the nucleation of calcium phosphate.

3.2.5 Improvement of CaP and $CaSi_2$/Si Wafer Interface

The CaP and Si wafer interface of the calcified $CaSi_2$/Si electrodes, although stable in de-ionized water for prolonged periods of time, was found to fail when calcified $CaSi_2$/Si wafers were used in the drug incorporation/release experiments (*e.g.* extended soaks in alendronate charging solutions or SBF during the drug release measurements resulted in partial or complete CaP film delamination from the $CaSi_2$ growth layers). Similar structures remained intact when the composite wafers were subjected to a brief thermal anneal (30 min, 600°C) prior to drug incorporation, as assessed by comparing initial and final signature phosphate peak intensities in the FT-IR spectra of these materials. The intimate role of the 600°C anneal in stabilizing the CaP-wafer interface is unclear, since for a Si/$CaSi_2$/CaP system this anneal may have an impact on any of the three phases individually, as well as on the silicon-silicide and silicide-apatite interfaces.

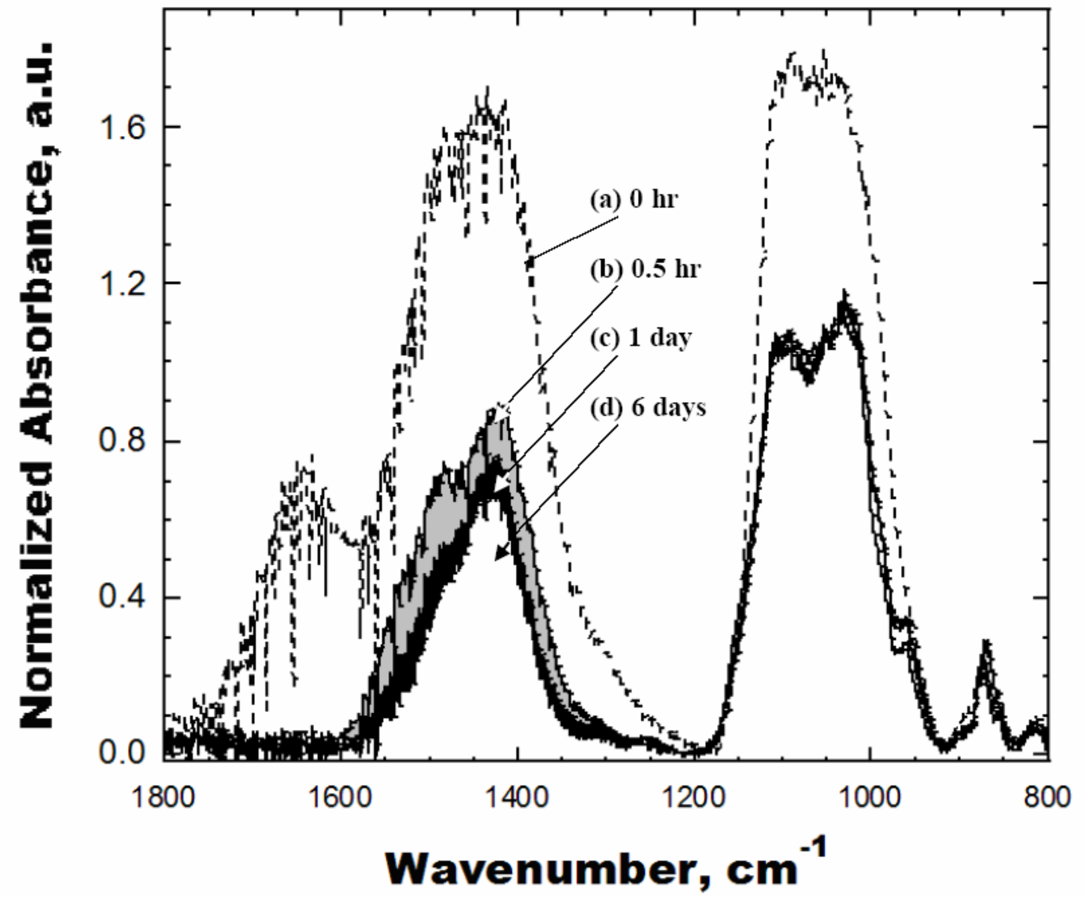

Figure 24. FT-IR absorbance spectra of calcified $CaSi_2$ film annealed under N_2 at 600°C for various periods of time: (a) 0 hr, (b) 0.5 hr, (c) 1 day, and (d) 6 days. The abrupt change in phosphate peak intensity between 0 hr and 0.5 hr reflects some loss of CaP during DI-water soak (15 min, 75°C), which was performed in between the measurements to remove CaP overgrowth layers. All spectra are normalized with respect to Si peak intensity.

Since formation of amorphous calcium carbonate was thought to occur at the early growth stage, *i.e.* at the CaP and $CaSi_2$/Si electrode interface, series of anneals were performed in order to determine if the calcified $CaSi_2$/Si wafers undergo thermally-induced dehydration and the silicide-apatite interface transforms to a stable calcitic form. Several Si/$CaSi_2$/CaP samples were systematically annealed at 600°C for up to 6 days, while the extent of crystallization was followed by the narrowing of the phosphate peaks (~1030 cm^{-1}) and carbonate peaks (~1420 cm^{-1}) in the FT-IR spectra.[22] The final phosphate peaks remained relatively unchanged, but the carbonate peaks sharpened significantly beginning with the very first 30 minute interval (see Figure 24). Furthermore, in all samples, the peak at ~1620 cm^{-1}, which is usually assigned to the H_2O molecules entrapped within various apatites,[22] also disappeared within 30 minutes, indicating dehydration of the CaP film.

3.2.6 Surface Modification of CaP with Alendronate

Simple immersion of calcified and annealed $CaSi_2$/Si wafers in alendronate solution followed by FITC exposure produced uniform fluorescent films. Unfortunately, due to the high intensity of focused UV excitation from a fluorescence microscope, which was necessary to produce detectable photoluminescence (PL) from small (1.2 mm) $CaSi_2$ sparked patterns, the majority of samples underwent significant bleaching of the FITC labels during the course of PL measurements. The problem is overcome when the alendronate solution is added to SBF during the second stage of electrochemical CaP growth on the pre-calcified and annealed $CaSi_2$/Si wafers. This kinetically-entrapped alendronate, subsequently coupled to FITC, is photophysically stable, presumably, due to the filtering and scattering of the short-wavelength UV radiation by the porous CaP structure. Figure 25 is a picture of a typical fluorescently-labeled Si/$CaSi_2$/CaP film, and the accompanying PL spectrum shows characteristic green FITC emission at 520 nm.

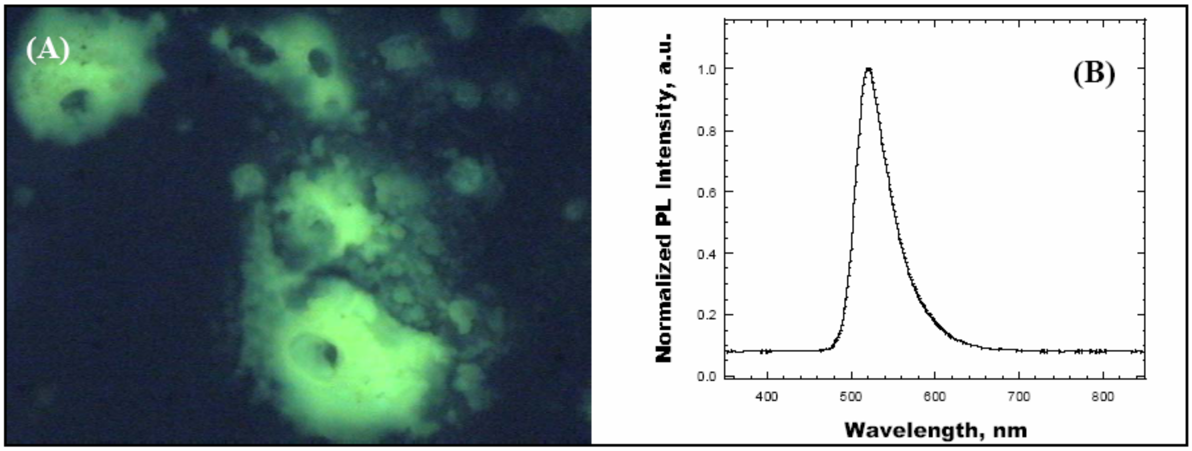

Figure 25. FITC-labeled alendronate-derivatized CaP on calcified $CaSi_2$/Si wafer: (A) fluorescence image and (B) the emission spectrum associated with (A).

3.2.7 Surface Modification of CaP with Norfloxacin: Loading and Release

Similar to kinetically-entrapped alendronate, norfloxacin was incorporated into CaP structures during 2 hours of the second stage of electrodeposition reaction using $CaSi_2$/Si wafers, which were pre-calcified for 2 hr (0.714 mA) and annealed (30 min, 600°C). Figure 26 shows the evolution of the deposited CaP film coverage as assessed by FT-IR. The drop in the phosphate peak intensity (~1030 cm^{-1}) indicates that some loss of CaP occurred during the DI-water soak (15 min, 75°C), which was performed after the first stage of electrodeposition. This loss of CaP is a reflection of a short duration of the first-time deposition period; $CaSi_2$/Si wafers, which were calcified for the optimal 4-hour periods, are significantly more stable. No change in the phosphate peak intensity between the initial drug-loaded sample and one which was taken after conclusion of a 5-hour long release experiment indicates that norfloxacin dissociated from within the pores in the film leaving the deposited CaP structure intact. Figure 27 shows the time-resolved release of norfloxacin from Si/$CaSi_2$/CaP structures in SBF. Since drug release experiments were performed inside fixed volume cuvettes, the UV absorbance values of the release medium reached saturation within 5 hours. Upon replacement with fresh SBF, the release continued.

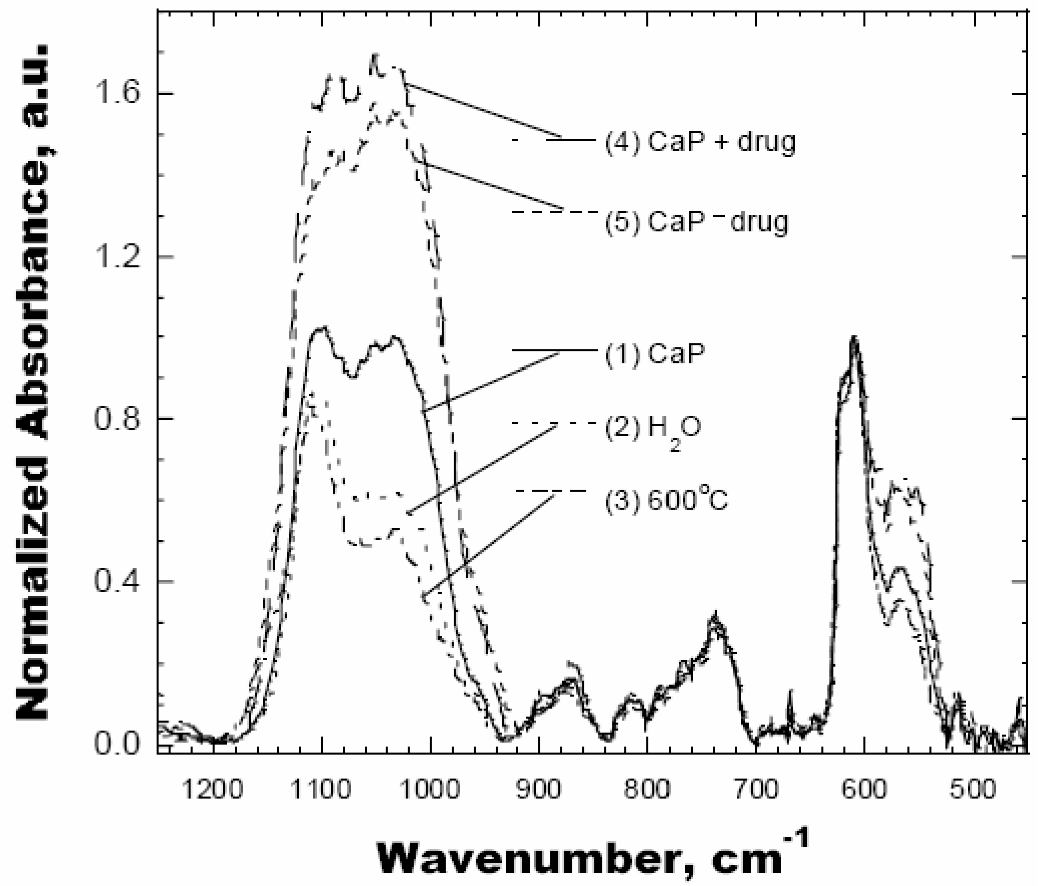

Figure 26. FT-IR spectra of calcified $CaSi_2$ growth layers on spark-processed Si — evolution of CaP film during norfloxacin loading and release experiments: (1) as deposited CaP [*1st stage*], (2) after soaking in H_2O, (3) after 600°C anneal, (4) as deposited CaP & norfloxacin [*2nd stage*], and (5) after release in SBF. All spectra are normalized with respect to Si peak intensity.

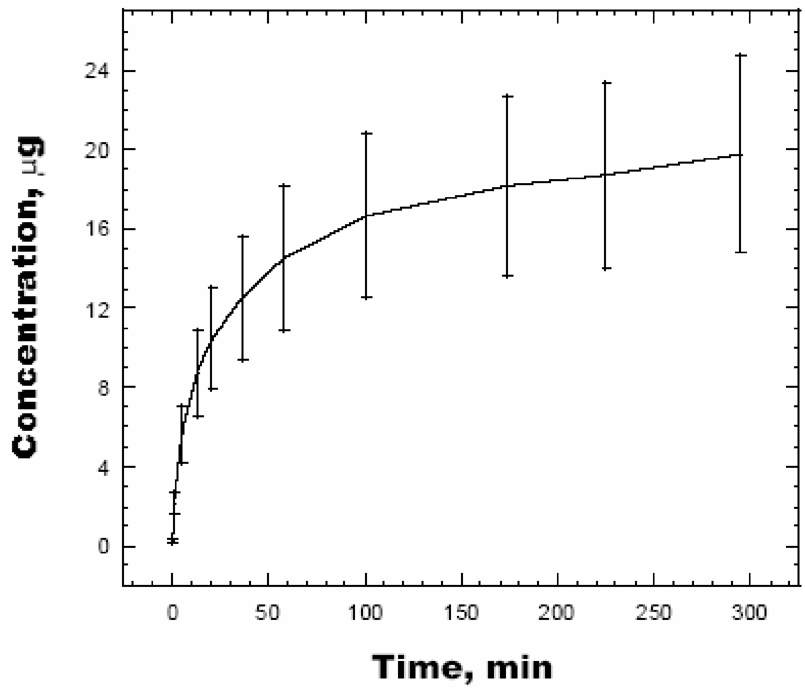

Figure 27. Time-dependent release of norfloxacin from Si/$CaSi_2$/CaP structures in SBF.

3.3 Discussion

3.3.1 Calcification of Porous Silica Films

Under the application of cathodic current to an oxide-terminated Si wafer electrode, the deposition of hydroxyapatite on porous silica growth layers is believed to follow the mechanism reported by Canham for bias-assisted calcification of bioactive porous silicon (‘BIOPSi’) wafers.[26] Ca^{2+} ions, attracted to the negatively charged electrode, combine with Si-OH groups (silanols) on the silica surface and subsequently induce biomineralization of CaP. Once a surface domain develops a positive charge due to the accumulated Ca^{2+} ions, it combines with phosphate ions. Thereafter, deposition of calcium phosphate continues and through a complex process eventually results in the formation of hydroxyapatite. The mechanisms of hydroxyapatite nucleation and growth on the surface of bioactive glass/ceramics (*e.g.* Bioglass^{TM}) are known (see Section 1.1). However, due to the accelerated growth conditions imposed by the presence of electric bias and the distribution of diverse surface chemistry of the spark processed material, the exact calcification mechanism for porous silica growth layer is unclear.

Similar to BIOPSi, the nucleation of hydroxyapatite catalyzed by Si-OH groups on the surface of SiO_2/Si is likely dependent on the concentration and structural arrangement of functional groups at the wafer surface. Due to its high surface area, the porous silica layer is significantly more hydroxylated than the rest of the silicon wafer, and, therefore, it is expected to be the primary site of CaP deposition. However, the presence of the electric bias clearly causes calcification to occur with variable reaction kinetics at several locations on the wafer electrode. The system is further complicated by the fact that the entire surface of the wafer is exposed to the electrolyte solution. Contrary to the electrochemical growth of CaP on BIOPSi where only the porous surface of the wafer electrode was exposed to SBF by the means of electrochemical cell design,[26] the setup shown in Figure 10 allows one to observe layer overgrowth phenomena and electrohydrodynamic effects which are expected to occur if the SiO_2/Si based implant was operating *in vivo*.

An electrohydrodynamic effect is thought to account for the lack of CaP growth around the porous silica growth layers, which was described previously. This phenomenon was originally reported by Trau *et al.* in their studies on field-induced layering of colloidal crystals.[92,93] Under the electrohydrodynamic mechanism, the presence of particles near the electrode surface or the patterning of electrodes causes gradients in current density, which generate convective flow across the electrode and drive the particles to the area with higher current density.[93] Wang *et al.* observed this effect during electrophoretic deposition of colloidal hydroxyapatite particles on Au/Pd-patterned silicon wafers.[94] In the case of SiO_2/Si electrodes, the polished silicon wafer area is deficient with respect to surface Si-OH groups compared to the porous silica growth layer with a significantly higher surface area. As a result, CaP electrodeposited outside the sparked pattern is not expected to be strongly anchored to the wafer surface. Therefore, hydroxyapatite particles which form in the close proximity of the insulating silica layer are swept towards more conductive areas on the wafer surface and away from the sparked pattern.

Although most of the electrochemistry was done on the simple circular patterns discussed previously, experimental two dimensional patterns were formed when the wafer or the Tesla coil were moved at a constant speed and gap distance. As shown in Figure 28, subsequent SBF/anneal/water treatments resulted in the matching CaP patterns. Note that the

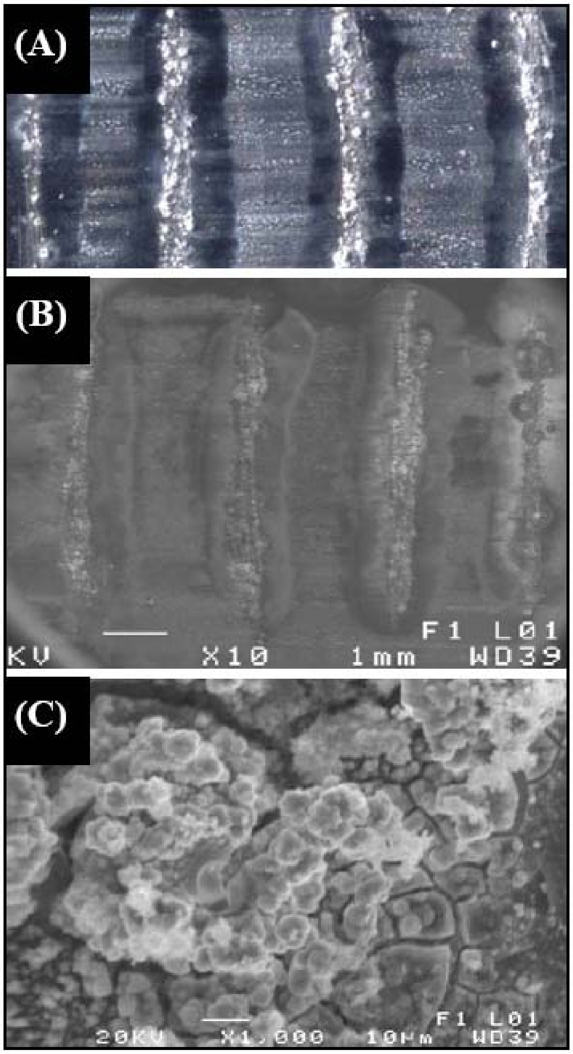

Figure 28. Calcified porous SiO_2 growth layers on spark-processed Si produced under manual spark guidance: (A) optical image, (B) plan view SEM, and (C) magnified view associated with.

calcified porous silica regions are encircled by the CaP-free polished areas beyond which the overgrowth layers coat the remaining wafer surface. The presence of irregular features on this pattern is due the manual spark guidance and arbitrary ablation time. The uniformity can be significantly improved by the use of an automatic custom-built sparking device previously developed by the Coffer's group.[82]

3.3.2 Calcification of Calcium Disilicide Films

The crystal structure of $CaSi_2$, where silicon sheets are intercalated with calcium (see Figure 3), intuitively points towards possible similarities between biomineralization behaviors of $CaSi_2$ and Bioglass^{TM}. The five-stage mechanism for hydroxycarbonate apatite formation on the surface of bioactive glass, formulated by Hench *et al.*, dictates that upon proper surface erosion, calcium and phosphate ions within bioglass migrate to the surface and form a $CaO-P_2O_5$-rich film on top of the SiO_2-rich layer, which, in turn, triggers the growth of amorphous calcium phosphate through electrostatic ion accumulation and its later crystallization into various apatites.[24] In fact, in the absence of electric bias, this mechanism plays a major part in biomineralization of free-standing $CaSi_2$ grains (Chapter 4 & 5). However, the electrochemical growth of CaP on spark-processed Si/$CaSi_2$ wafers is believed to occur via a process which encompasses details of Hench's mechanism pertaining to bioglasses and Canham's mechanism regarding porous silicon described earlier.

The surface of $CaSi_2$ growth layer is inherently Ca-rich, but these calcium ions can be buried within silica or are silicide-bound (see Figure 12D). In either case, because of the short periods of time allotted for electrodeposition reactions, an increase in local supersaturation with respect to calcium due to ion leaching is not expected. Therefore, similar to porous silica growth layers, calcium phosphate nucleation on $CaSi_2$ begins with Ca^{2+} complexation with negatively charged surface silanols. There is likely an abundance of Si-OH groups within the ablated silicide area produced during spark erosion of the silicon wafer, but their concentration is expected to be significantly smaller than in case of porous oxide-terminated Si. Yet, this $CaSi_2$/Si material produces a thermodynamically more stable CaP-wafer interface. Recent findings by Mooney *et al.*, who investigated the calcification behavior of biodegradable polymer films, state that the crystal size and morphology of carbonate apatite (CAp) are dependent on the SBF solution's characteristics but unaffected by the number of hydroxyl groups present on a bioactive surface, *i.e.* an increase in surface hydroxyls does not boost CAp growth.[48] Although porous silica and $CaSi_2$ growth layers exhibit similar anchoring sites for the growing calcium phosphate film, the local chemical composition of SBF around the nucleation sites is different for both cases due to the accelerated growth kinetics imposed by the presence of electric bias. As a result, since $CaSi_2$ growth layer is the most conductive part of the Si electrode, it is the primary target of the ionic current and causes a faster nucleation rate when compared to spark ablated silica. This increase in the reaction rate slows down crystallization of the initially deposited amorphous product. Amorphous calcium phosphate at the CaP-wafer interface will provide a higher contact surface area and a more stable composite material. Note that other SBF components (*e.g.* Mg^{2+}, carbonates, sulfates, *etc.*) are also driven to the wafer surface by the electric field. These may induce formation of calcite, apatite, magnesite and other sparingly soluble mineral systems, which are known to interconvert under certain conditions. [95-98] Additional non-CaP nucleation sites, if eventually overgrown by calcium phosphate, will warrant a denser and more uniform final CaP film and add to the explanation of the increased stability of the calcified $CaSi_2$ growth layer.

In the case of CaP electrodeposition on $CaSi_2$/Si wafers, the process is proposed to begin with formation of $CaCO_3$ nuclei alongside the amorphous calcium phosphate, which subsequently grows and crystallizes into magnesium-substituted calcite particles. Calcite is the most stable polymorph of calcium carbonate, and its crystallization from amorphous $CaCO_3$ precursor is expected to be slower than formation of aragonite or vaterite; however, calcite is the only crystalline form of $CaCO_3$ which is known to incorporate significant amounts of magnesium in its lattice.[99,100] Although conventional SBF has no potential for calcite formation,[101] this phenomenon has been documented by a number of research groups. In their recent detailed reassessment of apatite formation mechanism on bioactive glass surfaces, Chan *et al.* confirm the validity of Hench's mechanism for the apatite formation and point out (but do not discuss) the presence of calcite in the apatite films growing on bioglass samples during initial hours of SBF exposure, as assessed by X-ray diffraction analysis.[102] A similar observation was made by Vallet-Regi and co-workers during the bioactivity study of a CaO-SiO_2 binary glasses system.[103] Here, the presence of calcite was limited to those glasses with higher starting calcium content, and its growth was attributed to the existence of small $CaCO_3$ nuclei on the initial glass. In more recent work, Vallet-Regi reported incorporation of carbonates within first ten minutes of SiO_2-CaO-P_2O_5 sol-gel glass surface evolution in SBF.[104] Note that the carbonate incorporation is usually believed to take place at the later stages of apatite formation on bioglasses, during crystallization of amorphous calcium phosphate.[24] In addition, the analysis of experiments presented in Chapter 4 indicates that sparked $CaSi_2$/Si wafers, which were calcified in the absence of electric bias for various periods of time, show the presence of tricalcium phosphate, β-TCMP and monetite up to the first two weeks of SBF exposure as assessed by Raman spectroscopy (Chapter 4). Furthermore, similar experiments with free-standing $CaSi_2$ grains show formation of phosphate-free and magnesium-free deposits, which eventually convert to calcium phosphate, on silicon sheets within partially-split $CaSi_2$ grains after two weeks in SBF, as assessed by EDX (Chapter 5).

Apatite formation is a thermodynamically controlled process, but in the presence of electric bias, fast reaction kinetics significantly impact chemical equilibrium at the SBF-wafer interface. Dissolution of any precipitated products is disfavored by electrostatic attraction of ions to the electrode and continuous local supersaturation of SBF at the wafer surface when the bias is applied. According to calculations made by Kokubo *et al.*, carbonates form faster than phosphates in SBF, but the solution itself is a lot more saturated with respect to apatite rather than calcite, and the latter is not expected to precipitate under physiological conditions.[101] The ions from solution, drawn to the $CaSi_2$ growth layer by the ionic current, shift the equilibrium position to the left according to Le Chatelier's principle, and the reaction kinetics allow concurrent nucleation of carbonates and phosphates. The formation of carbonates under bias is further accelerated through the incorporation of Mg^{2+} and other ions, possibly forming Mg-substituted calcite. Incorporation of sulfate ions and silicates is known to distort the crystal structure of growing calcite through the unit cell expansion.[105,106] Lifted restrictions on crystal parameters will allow the $(Ca_xMg_y)CO_3$ nuclei to reach their critical size faster. The silicate oligomers form upon silicilic acid release from Si and $CaSi_2$, while the sulfate ions are initially present in the SBF. Furthermore, magnesium is known to force dissolution of embryonic hydroxyapatite nuclei,[107,108] which will also bring about a faster carbonate growth. Eventually, the surface of $(Ca_xMg_y)CO_3$ becomes poisoned by the attachment of phosphate groups,[109] and CaP growth proceeds according to the mechanism established for porous silicon.[26] Note that SO_4^{2-}, CO_3^{2-} and silicates may facilitate overgrowth of non-CaP nuclei by balancing the net charge of the calcium phosphate film through series of coupled ionic substitutions with PO_4^{3-}.

3.3.3 Improvement of CaP and $CaSi_2$/Si Wafer Interface

The intimate role of the 600°C anneal in stabilizing the CaP-wafer interface is unclear, since for a Si/$CaSi_2$/CaP system this anneal may have an impact on any of the three phases individually, as well as on the silicon-silicide and silicide-apatite interfaces. Improvements in structural integrity of the individual Si and $CaSi_2$ phases are unlikely since both phases possess melting points far exceeding the anneal temperature. Surface reconstruction and/or oxidation of Si-$CaSi_2$ interface is expected to come to completion during the ablation process due to the high temperature and atmospheric oxygen presence during the sparking event. Furthermore, rigorous post-ablation treatment of samples such as exposure to a focused stream of H_2O and then N_2 removes insecurely bound silicide grains; similar results were obtained when samples were submerged in H_2O and briefly exposed to ultrasound instead of a H_2O stream. Unfortunately, the detailed investigation of this issue was limited to visual inspection under the optical microscope; when the samples were analyzed by IR or SEM prior to SBF exposure, inconsistent growth results (in terms of total CaP coverage) were obtained, probably due to the introduction of impurities or mechanical damage to the wafer which may serve as additional sites for CaP electrodeposition. The random nature of silicide incorporation into the silicon wafer and the broad range of particle size distribution further complicate the analysis. Although some amorphodization of silicide may occur during the ablation process, crystalline gains are clearly present on the wafer surface prior to CaP deposition (see Figure 12). In addition, delamination of silicon sheets from the $CaSi_2$ grains is known to occur during CaP growth on $CaSi_2$ from SBF in the absence of electrical bias (Chapter 4 & 5). When the silicon sheets parallel to the wafer surface delaminate from the $CaSi_2$ grain, they may carry with them some of the deposited

CaP. In this case, the thermal treatment may halt the grain decomposition by linking the silicon sheets through the Si-O-Si bonds. Nonetheless, this process is not expected to occur in the time frame of electrodeposition reactions.

The most likely explanation for the stabilizing effect of the 600°C anneal is the partial crystallization of the deposited CaP to a less soluble form of hydroxycarbonate apatite. Short durations of the anneals and temperatures under 900°C were not expected to induce significant crystallization of degradable calcium phosphates,[22] and as it was found experimentally, prolonged 600°C thermal treatments did not significantly affect the majority of deposited apatite. The improved interface stability is explained here in terms of thermally-induced dehydration of the amorphous calcium carbonate at the CaP and $CaSi_2$/Si interface and its transformation to a stable calcite form.

3.4 Summary

Spark ablation is a facile dry-etch method for fabricating interfacial layers on silicon. Using this technique, porous silica and calcium disilicide films, which serve as active growth layers for bias-assisted deposition of calcium phosphates, were created on Si surfaces. While $CaSi_2$/Si wafer electrodes exhibit superior site-selectivity towards CaP electrodeposition, spark-processed silica is an appealing alternative since it can be used to form elaborate patterns of CaP films on Si. Bioactive/biocompatible silicon substrates are promising electronically-responsive platforms for the development of smart biomedical devices using existing microelectronics technology. Contrasting biomineralization behaviors of insulating SiO_2 and metallic $CaSi_2$ local domains on semiconducting Si allowed the elucidation of mechanistic details of the bias-assisted CaP film growth *in vitro*. In particular, under accelerated growth conditions imposed by the presence of an electric current, magnesium-rich calcium carbonates form alongside apatitic phosphates.

The potential biomaterial applications of calcium disilicide growth layers on spark-processed Si were also demonstrated through successful surface modifications of calcified $CaSi_2$/Si wafer electrodes with medicinally relevant compounds. Alendronate is now a commonly used drug in osteoporosis treatment.[110] This work demonstrates, it can also be used as a linker between calcified bioactive silicon and molecules that react with primary amine groups, which are exposed when alendronate is bound to the electrochemically-deposited CaP film on $CaSi_2$ growth layers. This strategy opens numerous pathways for the design of new biosensors and drug-delivery systems. In one specific proof-of-concept demonstration, norfloxacin was used to show sustained antibiotic drug release from calcified $CaSi_2$/Si.

Part I

CHAPTER IV.

Mechanism of Zero-Bias *In Vitro* Calcification of Calcium Disilicide Growth Layers on Spark-Processed Silicon

4.0 Overview

This chapter further explores the potential biomaterial applications of calcium disilicide by demonstrating its bioactivity *in vitro* in the absence of electric bias. Recall that during electrodeposition of calcium phosphate (CaP) on $CaSi_2$/Si (Chapter 3) the following phenomena were observed: (i) supersaturation (with respect to apatite) of the simulated body fluid (SBF) electrolyte was even further increased locally at the electrode-solution interface by the applied electric field; (ii) $CaSi_2$ growth layers became covered by CaP within hours, but otherwise the sparked silicide grains remained physically/chemically unchanged; and (iii) amorphous calcium carbonate formed parallel to CaP during the nucleation stage, but this could not be confirmed by any direct measurement due to extremely fast deposition kinetics. Furthermore, aside from providing an electrical contact to $CaSi_2$ growth layers, silicon wafers alone actively participated in the CaP nucleation and growth processes, thereby competing with $CaSi_2$. Investigating the zero-bias behavior of a new biomaterial is a logical next step in the search for new applications, and, because of a much slower expected calcification rate, it also may help the understanding of its biomineralization mechanism.

Here, mechanistic insights regarding $CaSi_2$/Si biomineralization are derived from an analysis of film growth morphology and chemical composition after various soaking periods in standard SBF. Changes in $CaSi_2$ calcification behavior as a function of reaction temperature and pH, SBF concentration, and various surface modification processes were also employed for this purpose. The time-resolved formation of interfacial CaP films was followed by Scanning Electron Microscopy (SEM), X-Ray Energy Dispersive Analysis (EDX), and Raman spectroscopy. The latter technique was utilized for several reasons. First, the routinely-used EDX instrument is equipped with a beryllium window, and, as a result, it cannot detect the presence of carbon in the deposited CaP. Therefore, the EDX alone cannot provide an adequate compositional analysis. For example, the presence of carbonate species in the electrodeposited CaP films was identified only by means of IR spectroscopy, used in conjunction with EDX (Chapter 3). When the IR and EDX were used together, it was still unknown whether the carbonate ions were a part of CaP lattice or merely a part of isolated deposits of calcium carbonate. Raman spectroscopy can identify the presence of apatite/carbonate phases and provide some assessment of their crystallinity (*e.g.* see Figure 29).[60,111-118] Finally, due to a relatively slow CaP deposition rate in the absence of bias, IR

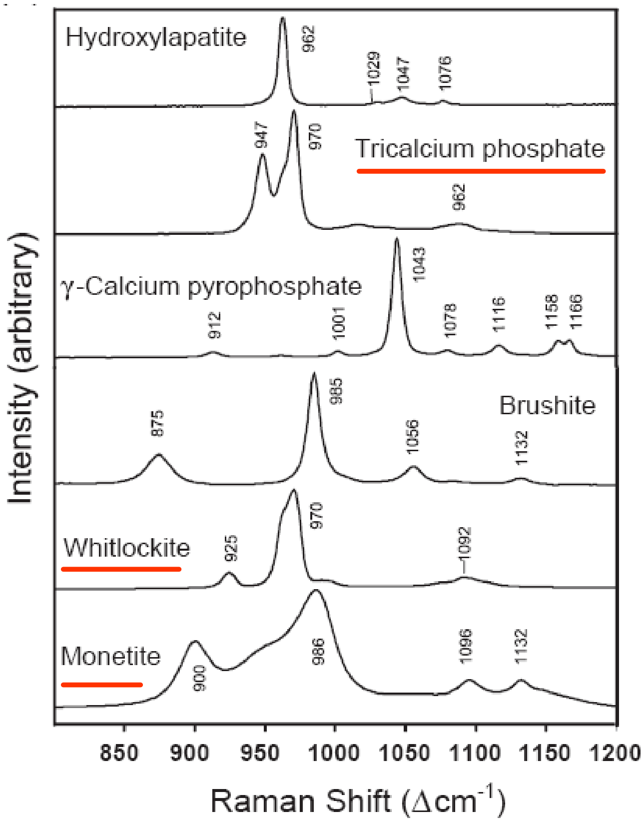

Figure 29. Raman spectra of different calcium phosphates that have different crystalline structures. Adapted from reference 60.

spectroscopy could not be used to analyze those CaP films which formed on $CaSi_2$ growth layers within 3 weeks of SBF exposure because of the instrument's detection limit. Therefore, biomineralization of $CaSi_2$ could not be followed continuously by means of IR, and a more sensitive Raman spectroscopic method was employed instead.

In this chapter it is shown that grains of $CaSi_2$, comprised of silicon sheets intercalated with calcium, decompose through a partial delamination of silicide layers and grow calcium phosphate phases via a mechanism similar to that for bioactive glass/ceramics.[24,46] Although the calcifying substrates in this case are $CaSi_2$/Si spark-processed wafers, the biomineralization mechanism for $CaSi_2$ proposed herein is the same as for free-standing (*i.e.* not incorporated into Si) $CaSi_2$ grains (Chapter 5). It is also shown that calcium disilicide is bioactive only at the physiological temperature of 37°C and bioinert at a lower temperature. Changes in $CaSi_2$ calcification behavior as a function of reaction temperature were studied for two reasons. First, there is a variety of potential applications in dentistry and medicine for hydroxyapatite formed at low or near-physiological temperature.[119] For example, it can be used as a synthetic enamel for rapid tooth repair.[120] Yet, the main purpose of the temperature reduction is to further decrease the rate of CaP precipitation and promote deposition of calcium carbonates (as a negative control) on $CaSi_2$ growth layers over CaP. The mechanisms of crystallization and transformation of calcium carbonates formulated by Sawada indicate that during the nucleation stage, amorphous calcium carbonate is more likely to transform into calcite if the reaction temperature is kept at 25°C.[109] Vaterite, a less stable polymorph, is more abundant at 37°C than calcite at the early metastable stage.[109] Fast dissolution kinetics of vaterite (relative to calcite) assure that there is less competition for the nucleation sites between carbonates and CaP. On the other hand, calcite is the preferred phase at 25°C.[109] In this case, heterogeneous nucleation of CaP on $CaSi_2$ is expected to be significantly retarded, if not completely inhibited.

4.1 Experimental

4.1.1 Spark-Processing of Si

Pieces (8 mm x 14 mm) of p-type, <100>, boron-doped CZ Si (9-18 Ω cm) were pre-cut, washed, and dried via identical procedure as in Chapter 3. Recall that during the last step of the washing sequence wafers were soaked in a $(NH_4)_2S_2O_8/H_2SO_4$ (conc.) cleaning solution for 12-24 hours until a moment prior to spark ablation, at which point they were removed from the cleaning solution, thoroughly washed with DI-water, and dried under a stream of N_2. Therefore, wafer surfaces were hydrophilic at the beginning of each experiment.

Spark ablation was performed in a manner similar to the procedure in Section 3.1.1. In this process, a Ni wire cathode is inserted inside a glass capillary tube (1.2 mm inner diameter), which is partially filled with $CaSi_2$ powder (Johnson Matthey) and pressed against a silicon wafer (anode) at the other end. Immediately prior to sparking, the capillary tube was dipped into the $CaSi_2$ powder up to a fixed 6 mm mark and mounted on top of the wafer. A conical steel plate (diameter ≤ 1.2 mm) was then inserted inside the tube on top of the $CaSi_2$ powder, and the tip of the cathode positioned at a fixed distance (3 mm) above the plate. The excess powder on the outside was removed by a gentle stream of N_2. The contact to Si was made with an alligator clip. All samples were exposed to the Tesla coil discharge for 900 seconds. Upon completion of the sparking events, samples were rinsed under a strong focused stream of DI-water to remove any loose particles and dried under a steam of N_2. In some cases, wafers were cleaved to remove those parts of the wafers where the alligator clip was attached. Such samples possess slightly smaller dimensions (8 mm x 12 mm) and are referred to as "cleaved," in the discussion that follows.

4.1.2 Preparation of SBF and Its Modified Solutions

The SBF solutions were prepared according to a literature procedure.[88] The pH values and the ion concentrations of the SBF and its modified (pH or concentration of Ca^{2+} or HPO_4^{2-} were raised to accelerate precipitation of CaP) solutions are shown in Table 3. Each solution was prepared by dissolving reagent grade $CaCl_2{\cdot}2H_2O$, Na_2SO_4, NaCl, KCl, $MgCl_2{\cdot}6H_2O$, $NaHCO_3$ and K_2HPO_4 in a buffer of trishydroxymethyl-aminomethane and HCl.

		Concentration (mM)							
	pH	Ca^{2+}	HPO_4^{2-}	K^+	Na^+	Mg^{2+}	Cl^-	CO_3^{2-}	SO_4^{2-}
Blood Plasma	7.40	2.50	1.00	5.00	142	1.50	103.0	27.0	0.50
SBF	7.40	2.50	1.00	5.00	142	1.50	147.8	4.20	0.50
pH 7.60 SBF	7.60	2.50	1.01	4.99	142	1.50	147.8	4.19	0.51
Ca 1.50 SBF	7.40	3.74	1.01	5.01	142	1.50	150.3	4.20	0.50
P 1.50 SBF	7.40	2.49	1.50	5.98	142	1.50	147.8	4.19	0.50

Table 3. Ion concentrations of human blood plasma, SBF, and its modified solutions. Adapted from reference 88.

4.1.3 Calcification at 25°C

As-prepared samples (cleaved and uncleaved) were immersed in 20 mL and 80 mL aliquots of standard and modified SBFs for set periods of 3, 4, and 5 weeks at room temperature. The samples were then removed form a given solution, rinsed with DI-water, dried under a stream of N_2 and analyzed by SEM/EDX.

4.1.4 Surface Treatments and Calcification at 37°C

Three types of surface-treated wafers were used: P-$CaSi_2$, Mg-$CaSi_2$ and HF-$CaSi_2$. In case of P-$CaSi_2$ samples, the as-prepared $CaSi_2$/Si wafers were immersed in 2 mL aliquots of K_2HPO_4 (0.5 M) at 37°C for 2 hours. Some of these samples were then immediately placed in SBF, while others were first pre-washed with DI-water/ dried under a stream of N_2 prior to SBF immersion. As-prepared Mg-$CaSi_2$ samples were immersed in 2 mL aliquots of $MgCl_2$ (0.5 M) at 37°C for 2 hours. These samples were then pre-washed with DI-water, dried under a stream of N_2 and placed in SBF. In case of HF-$CaSi_2$ samples, as-prepared $CaSi_2$/Si wafers were dipped into a 48% HF solution for 30 seconds, then thoroughly washed with ethanol/ DI-water, and dried under a stream of N_2 prior to SBF exposure.

Surface-modified samples (alongside as-prepared control) were immersed in 3 mL aliquots of standard SBF for 4 weeks. SBF was replaced with a fresh solution after the first two-week period. The samples were then removed from the SBF, rinsed with DI-water, dried under a stream of N_2 and analyzed by SEM/EDX. Next, as-prepared samples were immersed in 25 mL aliquots of standard SBF for various set periods of time up to 4 weeks. SBF was replaced with a fresh solution after the first two-week period. The samples were then removed from the SBF, rinsed with DI-water, dried at 37°C ($\geq$ 24 hr), and analyzed by SEM/EDX and Raman.

4.1.5 Instrumentation

Surface analysis was done using a JEOL JSM-6100 Scanning Electron Microscope (SEM) coupled with an Energy Dispersive X-Ray (EDX) Analysis detector under 20 kV accelerating voltage. Raman measurements were obtained on a custom-built system employing an Ar^+ laser source in conjunction with a Roper Scientific intensified CCD and a Holo Spec Vpt System from Kaiser Optical Systems, Inc.

4.2 Results

4.2.1 Calcification at 25°C

Immersion of $CaSi_2$/Si wafers in standard SBF at room temperature results in no calcium phosphate formation on $CaSi_2$ growth layers, as assessed by FT-IR. Similar results were obtained when SBF solutions modified with respect to pH, Ca^{2+}, or HPO_4^{2-} were used. SEM analysis of these samples indicates that the physical state of $CaSi_2$ grains has not significantly changed, while the corresponding EDX spectra show approximately 2:1 Si/Ca peak ratios, characteristic of original $CaSi_2$ (Figure 30). A slight decrease in calcium peak

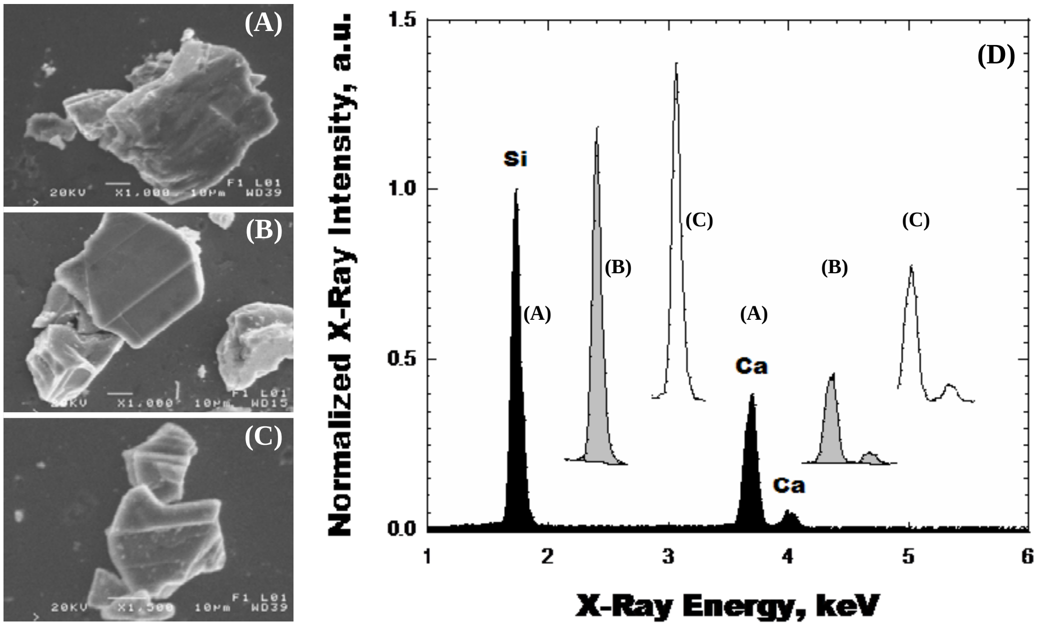

Figure 30. Plan view SEM & EDX spectra of $CaSi_2$ grains on spark-processed Si after 4 weeks in modified SBFs at 25°C: (A) Ca 1.50 SBF, (B) P 1.50 SBF, (C) pH 7.60 SBF, and (D) the EDX spectra associated with (A-C). All spectra are normalized with respect to Si peak intensity.

intensities reflects partial ion-leaching, but this process is inefficient at 25°C compared to the results obtained at 37°C (*vide supra*). The only deposition products that were found on $CaSi_2$ growth layers during these experiments were isolated spherulites such as the one shown in Figure 31. Compositional analysis of these spherulites by EDX typically reflects low Ca levels, often at the instrument's detection limit. Nonetheless, occasionally Si/Ca ratios on the order of 3:1 are observed. Aside from Si and Ca, no other elements were detected, which indicates that calcium within the spherulites is most likely ion-paired with oxygen, carbonates, or silicates. It must also be noted that the routinely used EDX instrument is equipped with a beryllium window, and the presence of oxygen and carbon is invisible to this detector.

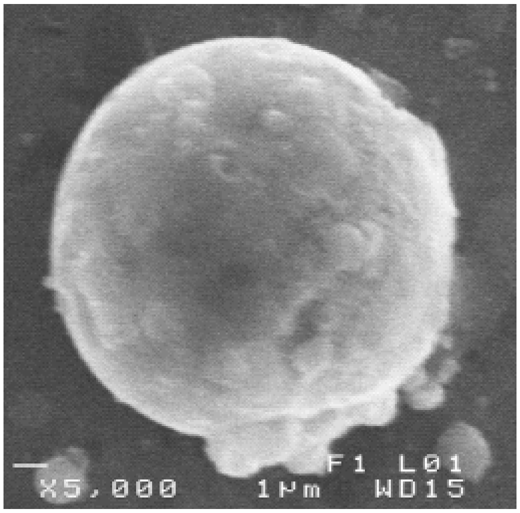

Figure 31. A plan view SEM of an isolated spherulite on $CaSi_2$ growth layer, which was exposed to 'P 1.50 SBF' solution for 4 weeks at 25°C.

Interestingly, CaP deposits were consistently found on the uncleaved wafers in the areas where the Tesla coil electrode had been connected to Si. Minor silicon wafer surface erosion at these locations (as a consequence of a discharge) is expected to produce porous silica layers with a relatively high density of silanols (see Chapter 3). Successful calcification of porous SiO_2 layers alongside inactive $CaSi_2$, both of which have been introduced onto the wafer surface via spark ablation, is a positive control which rules out potential system contamination as a reason for the observed lack of CaP formation on $CaSi_2$.

Overall, $CaSi_2$ appears to be bioinert at room temperature under the conditions of zero bias. In contrast to these observations, similar $CaSi_2$/Si samples calcified readily in standard and all of the modified SBF solutions when an electric current (~0.7 mA) was applied and produced CaP films with the same morphology and composition, as had been shown in Chapter 3. Hence the reference to the electrodeposition experiments is made only to underline the increased role of $CaSi_2$ surface chemistry in zero-bias biomineralization *in vitro*.

4.2.2 Calcification of $CaSi_2$/Si Wafers at 37°C

When the temperature is raised to 37°C, as-prepared and surface-modified $CaSi_2$/Si wafers calcify readily within the 4-week exposure period to SBF. Furthermore, the deposited CaP films, which cover the entire wafer surfaces, can be observed with the unaided eye when samples are first removed from their corresponding SBF solutions. In the case of most samples, a subsequent gentle rinse with DI-water and/or the stream of N_2 which was applied during the drying step, removed overgrowth layers from the polished wafer surfaces around the sparked areas, leaving the deposited CaP films anchored only to $CaSi_2$ growth layers. This delamination appeared to occur with varying degrees of difficulty, reflecting the structural integrity of the deposited CaP films. For example, parts of the overgrowth layer on

Mg-$CaSi_2$ wafers separated from the surface on first contact with DI-water stream, while P-$CaSi_2$ samples retained their CaP film even after 3 minutes of sustained irrigation and exposure to a focused N_2 stream (see Figure 32). Overall, a SEM/EDX analysis revealed

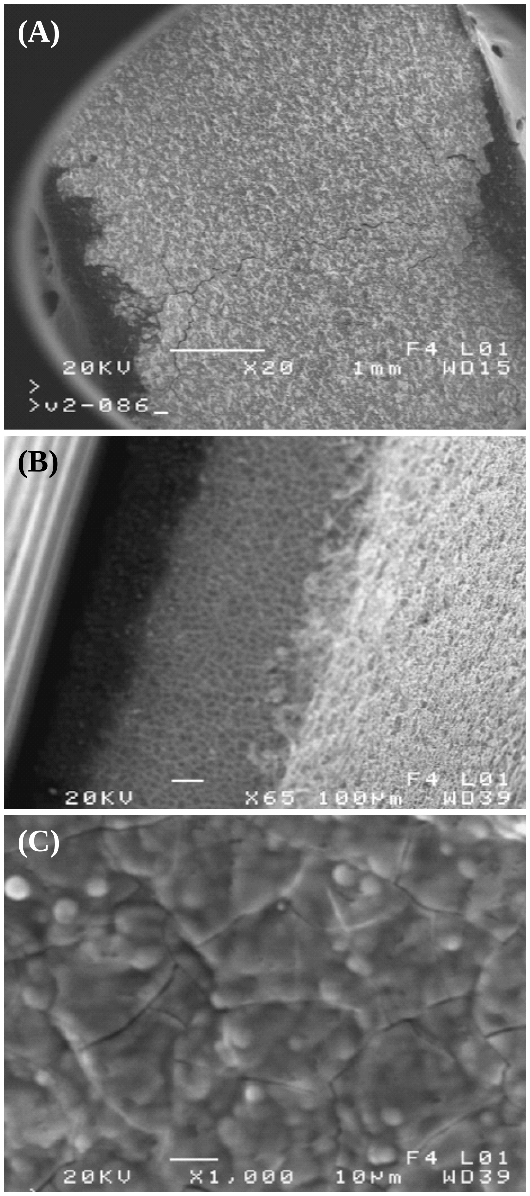

Figure 32. A CaP overgrowth layer formed on the surface of a $CaSi_2$/Si wafer after surface treatment with K_2HPO_4 followed by a 4 week soak in SBF at 37°C: (A) plan view SEM, (B) tilted view showing the wafer edge covered by CaP, and (C) magnified view of (B).

rather subtle changes in morphology and composition of the final CaP films formed on $CaSi_2$ growth layers of all wafers used in these experiments. Nonetheless, some mechanistic insights regarding biomineralization can be inferred from the differences in coverage and chemical composition of CaP films deposited from SBF after various surface treatments had been applied to $CaSi_2$/Si wafers.

The interfacially controlled nucleation of calcium phosphate is expected to begin once $CaSi_2$ growth layers have developed an appropriate negative surface potential to gather positive calcium ions in SBF. Calcium disilicide is a particularly interesting material in this regard, since upon immersion in SBF, it may develop the necessary negative surface potential by exposing Si-OH (silanol) groups and/or by forming a complex between the silicide-bound calcium and the phosphates from the fluid. In the latter case, biomineralization can occur in a manner similar to synthetic hydroxyapatite.[121] This is in addition to the surface erosion of $CaSi_2$ grains in SBF and potential similarities with the known biomineralization mechanism of Bioglass^{TM} (see Section 1.1).

Figure 33 shows a typical morphology and composition associated with as-prepared $CaSi_2$ growth layers on spark-processed Si, which were calcified during 4 weeks in SBF at 37°C. Spherulites with diameters ranging from 1-3 μm form a thin plate-like film at the base of larger uniquely-shaped CaP structures, which emerge above the wafer surface due to the layer overgrowth. Such CaP films crack under rapid drying conditions (or evacuation of the SEM chamber) and often appear in SEM images as isolated platelets. In addition, continuous overgrowth layers (similar to Figure 32) cover the entire polished wafer surfaces prior to the DI-water rinse, which indicates that the system is under the diffusion-controlled growth by the end of the 4 week soak in SBF, and the interfacially-controlled CaP growth is over.

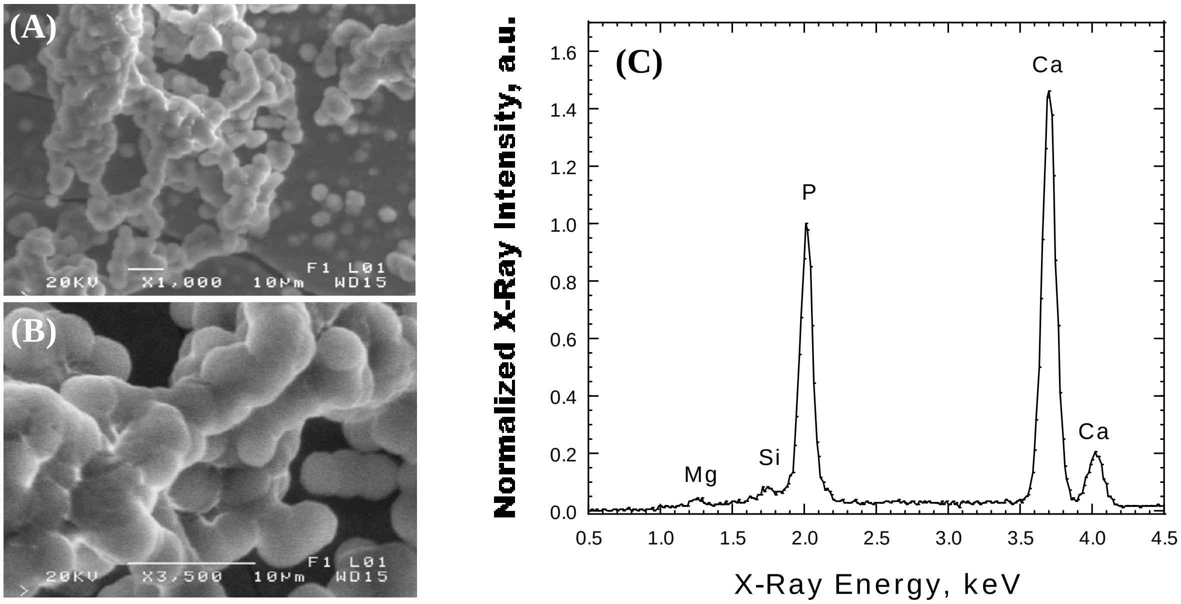

Figure 33. A calcified $CaSi_2$ growth layer on spark-processed Si after 4 weeks in SBF at 37°C: (A) plan view SEM, (B) magnified view of (A), and (C) the EDX spectrum associated with (B).

4.2.2.1 Effects of Surface Treatments

In principle, the $CaSi_2$ growth layer's ability to induce nucleation of CaP may be strongly influenced by the surface Si-OH groups, much like Canham's low porosity silicon.[71] In order to evaluate the extent of surface silanol contribution to the calcium phosphate nucleation process, $CaSi_2$/Si wafers were hydride-terminated via a simple immersion in HF solution. A typical morphology and composition associated with HF-treated $CaSi_2$ samples are shown in Figure 34; both appear strikingly similar to the untreated $CaSi_2$/Si wafers discussed above. Similar to the control, continuous overgrowth layers initially covered the entire wafer surfaces, and upon their delamination during the DI-water rinse, one could observe multiple holes present within the exposed polished silicon areas.

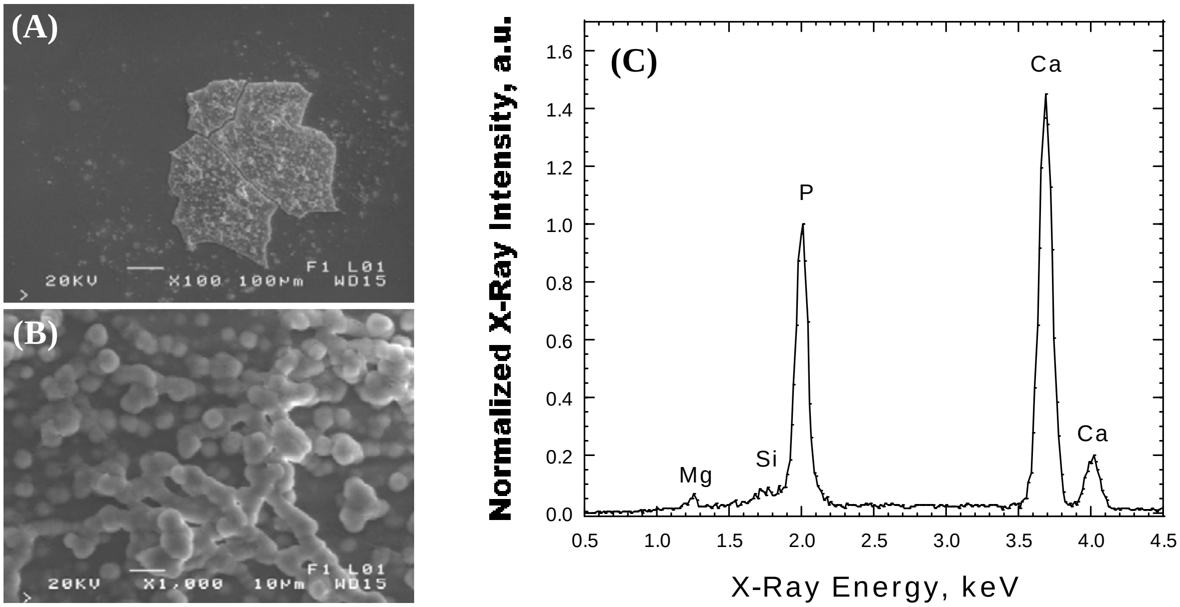

Figure 34. A calcified CaSi$_2$ growth layer on spark-processed Si after surface treatment with HF followed by a 4 week soak in SBF at 37°C: (A) plan view SEM, (B) magnified view of (A), and (C) the EDX spectrum associated with (B).

Exposures of CaSi$_2$ growth layers to HPO_4^{2-} and Mg^{2+} containing solutions were originally expected to increase and decrease the rate of CaP nucleation, respectively. Magnesium is known to inhibit biomineralization processes *in vitro* and *in vivo*,[22,53] while rates of calcification of bioactive glass/ceramics are raised with higher phosphate concentration in their matrix.[22,24] Both Mg- and P-CaSi$_2$ samples formed continuous CaP films throughout their surfaces upon SBF exposure. However, the former appeared under SEM imaging to have the thinnest overgrowth layers and showed the largest degree of delamination (see Section 4.2.2) during the post-growth washing steps. On the other hand samples which had been exposed to the phosphate solution possessed the thickest CaP, which appeared barely cracked during the final SEM analysis. Figures 35 and 36 show the local

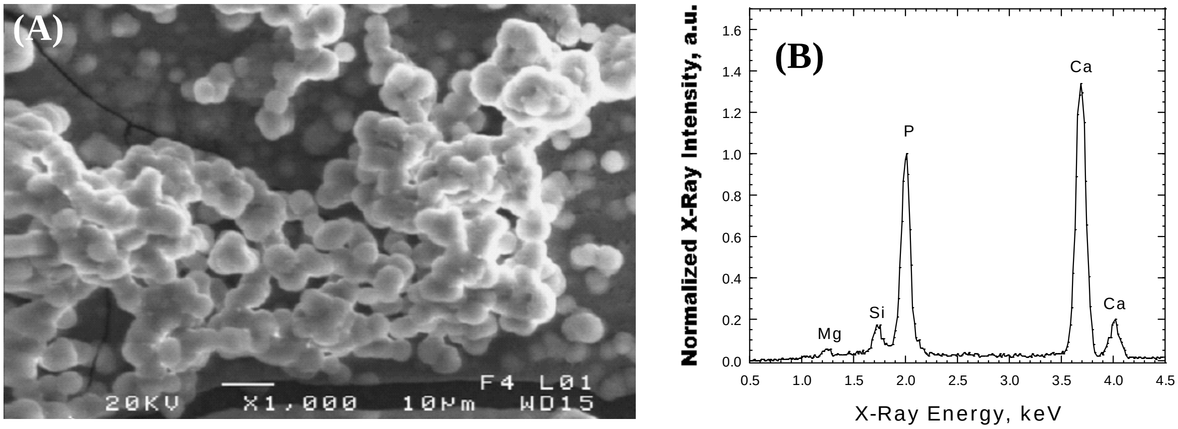

Figure 35. A calcified $CaSi_2$ growth layer on spark-processed Si after surface treatment with K_2HPO_4 followed by a DI-H_2O rinse and a 4 week soak in SBF at 37°C: (A) plan view SEM and (B) the EDX spectrum associated with (A).

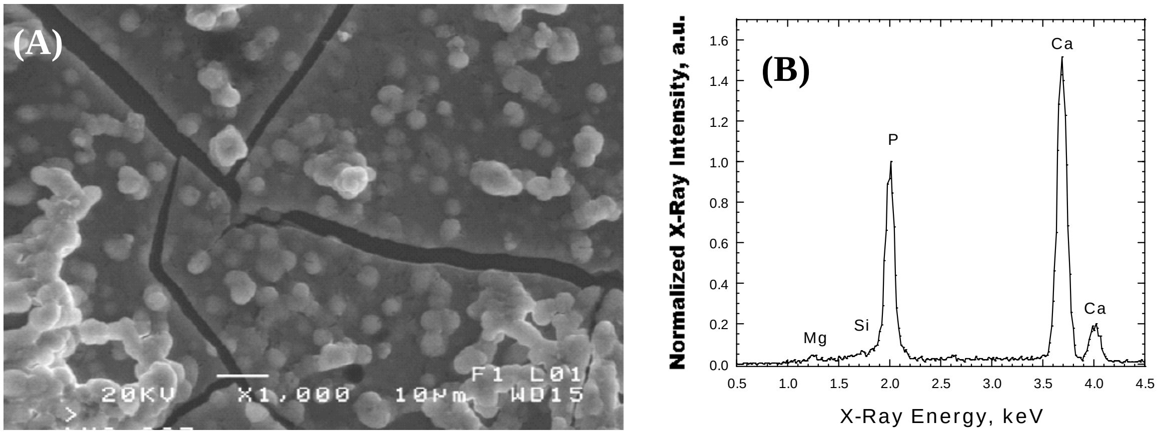

Figure 36. A calcified $CaSi_2$ growth layer on spark-processed Si after surface treatment with $MgCl_2$ followed by a DI-H_2O rinse and a 4 week soak in SBF at 37°C: (A) plan view SEM and (B) the EDX spectrum associated with (A).

microstructures and associated compositions of calcified $CaSi_2$ growth layers on P- and Mg-$CaSi_2$ wafers, respectively. For a given sample type, no significant difference was noted between the samples which were pre-washed with DI-H_2O prior to SBF immersions and those wafers which were placed in SBF immediately after the surface treatment.

Table 4 presents the Ca/P peak ratios which were obtained from the EDX analysis of surface-modified/calcified $CaSi_2$ growth layers on Si. Variation in these values reflects changes in the stoichiometry of the final CaP films depending on the type of surface treatment, and suggests relative biomineralization rates for a constant SBF exposure time. The similarity between untreated samples and those which were hydride-terminated in HF indicates that the rate of CaP nucleation remains unaffected despite the reduced number of Si-OH groups on the surface of $CaSi_2$. Therefore, $CaSi_2$ growth layers do not initiate CaP nucleation exclusively through surface silanols. The initial presence of phosphates on the surface of $CaSi_2$, on the other hand, results in Ca-deficient phases of the final calcium phosphate films, as reflected by the lower Ca/P peak ratio obtained from the P-$CaSi_2$ samples. Substitution of Ca^{2+} in an apatite framework by other cations (*e.g.* Na^+, Mg^{2+}) is an indication of an accelerated CaP growth rate. Surface reactions with phosphate ions from the K_2HPO_4 solution can affect the nucleation rate of CaP in two ways: (i) phosphates can chemically attach to the silicide-bound calcium ions, thereby contributing to the negative

	Surface Treatment			
	None	HF	K_2HPO_4	$MgCl_2$
Ca/P	1.44	1.45	1.34	1.52

Table 4. Ca/P peaks ratios obtained from the EDX analysis of surface-modified/ calcified $CaSi_2$ growth layers.

surface potential, and (ii) physisorbed phosphates can detach from the surface once the sample is in SBF and increase the local saturation of SBF with respect to CaP, thereby accelerating the onset of nucleation. Contribution of the latter can be excluded, since similar results were obtained with those samples which had been pre-washed in DI-H_2O prior to SBF exposure. Finally, exposure to $MgCl_2$ results in a slower nucleation of CaP, as indicated by the increased Ca/P peak ratio. In SBF, hydrated magnesium is expected to poison CaP nucleation sites on $CaSi_2$ by complexing with surface silanols and shielding local surface areas, which may otherwise participate in the nucleation process. Similar to the case of P-$CaSi_2$ samples, the contribution of physisorbed $MgCl_2$ can be excluded. Overall, under zero-bias conditions, biomineralization of $CaSi_2$ growth layers on spark-processed silicon is most affected by the reaction temperature, while the functional groups, which are present on the surface of as-prepared silicide, do not significantly contribute to this process.

4.2.2.2 Evolution of $CaSi_2$ Morphology

As discussed previously, $CaSi_2$ grains retain their physical state even after a month in various SBF solutions at 25°C (see Figure 30). When $CaSi_2$/Si wafers are immersed in SBF at 37°C, $CaSi_2$ undergoes gradual structural decomposition. Figure 37 shows delamination of $CaSi_2$ grains during the first week of SBF exposure, by the end of which the grains appear under the SEM as piles of thin plates (see Figure 37C). No similar structures were found present on the surface of $CaSi_2$/Si wafers which had been exposed to SBF for longer periods of time. Therefore, structural decomposition of $CaSi_2$ is understood to come to completion within 10 days of a biomineralization process at 37°C. In addition, as the surface evolves, the concentration of calcium within these grains reduces (Figure 37D).

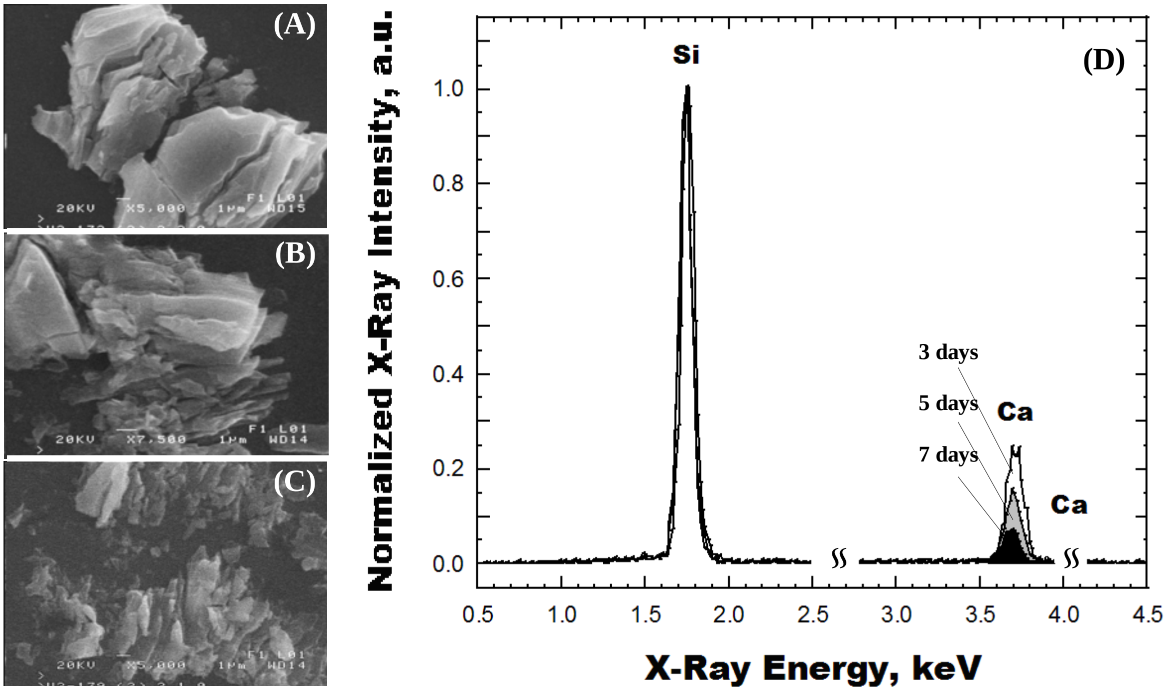

Figure 37. Plan view SEM & EDX spectra of time-dependent surface evolution of $CaSi_2$ grains on spark-processed Si in SBF: (A) day 3, (B) day 5, (C) day 7, and (D) the EDX spectra associated with (A-C). All spectra are normalized with respect to Si peak intensity.

Another change in calcification behavior of $CaSi_2$ growth layers which is induced by the temperature elevation is the formation of isolated spherulites, such as the one shown in Figure 38. On average, these spherulites appear 3-5 times smaller than those that form at 25°C (see Figure 31). The frequency of occurrence of such structures increases as biomineralization progresses. Although it is difficult to establish a definite trend in their compositional change using this particular EDX instrument (aside from Si and Ca, no other elements were detected), a typical starting calcium peak intensity (1:2 ratio relative to Si) appears to gradually decrease during the first two weeks and remain constant thereafter, until CaP overgrowth layers cover wafer surfaces and such spherulites are no longer visible.

Incorporation of phosphate ions within these spherulites, indicated by appearance of the phosphorous signature peak in their associated EDX spectra, occurs in between 16 and 20 days in SBF.

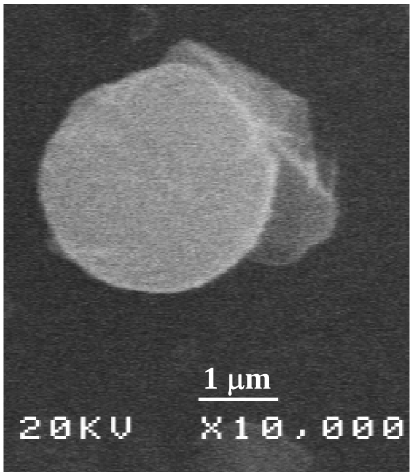

Figure 38. Plan view SEM of an isolated spherulite on a $CaSi_2$ growth layer, which was exposed to SBF solution for 1 week at 37°C. A piece of $CaSi_2$ grain, to which the spherulite appears to be attached, is seen in the background.

4.2.2.3 Raman Analysis of Calcified $CaSi_2$ Layers

A typical Raman spectrum (an enlargement of the P-O stretching region between 800 and 1200 cm^{-1}) associated with calcified $CaSi_2$ layers, which had been exposed to SBF for 28 days at 37°C, is presented in Figure 39. The peaks at 951 cm^{-1} and 977 cm^{-1} are due to the phosphate symmetric stretch modes, but the spectrum itself does not identify with any of the known calcium phosphate phases. The measured Raman spectra resemble those for tricalcium phosphate (peaks at 947 cm^{-1} and 970 cm^{-1}), whitlockite (broad peak at 970 cm^{-1}), and monetite (sloping broad peak at 986 cm^{-1}) (see Figure 29).[60,112] The peaks appear slightly shifted towards lower wavenumbers compared to those samples which had been soaked in SBF for shorter periods of time. Overall, the data suggest that CaP films, which deposit on $CaSi_2$/Si within a month, may include a mix of several calcium phosphate phases such as Mg-substituted whitlockite, tricalcium phosphate, and monetite.

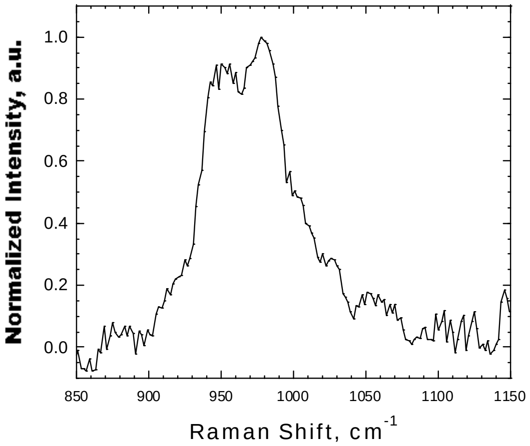

Figure 39. A typical Raman spectrum of a calcified $CaSi_2$ layer on spark-processed Si after 4 weeks in SBF at 37°C.

4.3 Discussion

In theory, $CaSi_2$ grains, where silicon sheets are intercalated with calcium,[40] may initiate CaP nucleation by utilizing surface Si-OH groups similar to bioactive glasses or as synthetic hydroxyapatite by forming a complex between the silicide-bound calcium and phosphate ions from the fluid.[121] The calcification study conducted at 25°C indicates that, in the initial state, the surface of $CaSi_2$ growth layers does not provide adequate structural sites with proper coordination for calcium binding. Modified SBF solutions, such as the ones used in this work, are known to accelerate growth of calcium phosphates *in vitro*,[88] but did not have any effect on $CaSi_2$ growth layers; however, the porous silica areas, which were present on the same wafers, on the other hand, concurrently calcified. Surface treatments with HF, K_2HPO_4, and $MgCl_2$ indicate that both Si-OH and surface-bound phosphates participate in the nucleation process, with less importance being placed on the silanol groups. Finally, the time-dependent surface evolution study shows that the structural decomposition of $CaSi_2$ grains (and the associated local release of calcium) is a prerequisite to CaP deposition. The mechanistic details regarding zero-bias biomineralization of $CaSi_2$ growth layers on spark-processed silicon in SBF can thus be summarized as follows:

- Within 10 days, $CaSi_2$ grains undergo complete decomposition accompanied by the local release of calcium.
- $CaSi_2$ growth layers acquire negative surface charge through surface hydrolysis and adsorption of phosphates.

- Within 20 days, spherulites, which are initially deposited in the form of calcium carbonate/silicate, acquire phosphates through ion exchange with the SBF solution.
- The calcium phosphate phases, which are present during various growth stages, possibly include a combination of Mg-substituted whitlockite, monetite, and tricalcium phosphate.

4.4 Summary

The development of new techniques for fabricating bioactive silicon platforms is an important area of research in the field of bioelectronics. Incorporation of calcium disilicide into silicon wafers via spark-processing technique is a facile dry-etch method for producing silicon surfaces capable of biomineralizing in the presence and in the absence of an electric bias *in vitro*. The process of $CaSi_2$/Si calcification under zero bias appears to follow the same mechanism as bioactive glasses/ceramics, during which calcium phosphate growth is significantly dependent on the structural degradation of $CaSi_2$ grains. Surface functional groups, initially present on the as-prepared material, cannot induce CaP nucleation which begins only upon delamination of $CaSi_2$ layers. This work with $CaSi_2$/Si demonstrates that control over biomineralization rate and mechanism can be eventually achieved by tuning the reaction temperature and/or applying electric current instead of tailoring the starting chemical composition and structure of a biomaterial, which is typically done in case of other platforms.

Part I

CHAPTER V.

Biomineralization of Calcium Disilicide in Porous Polycaprolactone Scaffolds

5.0 Overview

This chapter describes the biomineralization of calcium disilicide ($CaSi_2$) within porous polycaprolactone [PCL; —{$O(CH_2)_5CO$}$_n$—] scaffolds. $CaSi_2$ is a semimetal; its crystalline structure consists of silicon sheets intercalated with calcium.[44] The previous two chapters demonstrated that calcium disilicide growth layers can be used to impart bioactivity onto an underlying crystalline silicon substrate. The biomineralization of $CaSi_2$ occurs via a mechanism similar to that of Bioglass^{TM},[24] while the application of the electric bias to $CaSi_2$/Si composite electrodes greatly accelerates the deposition of calcium phosphates (CaP) in simulated body fluid (SBF). The incorporation of $CaSi_2$ grains within a PCL framework results in bioactive and biodegradable scaffolds which may be used in bone tissue regeneration. Furthermore, the presence of semimetallic $CaSi_2$ may potentially extend the applications of such scaffolds to the field of bioelectronics.

In this work, porous PCL scaffolds were prepared via a combination of salt-leaching/microemulsion methods.[122] Several porogens were evaluated: NaCl alone, a mixture of NaCl and $CaCl_2{\cdot}2H_2O$, or a mixture of NaCl and K_2HPO_4. To provide markedly different structural environments for the inorganic phase, calcium disilicide powder was either added to a mixed-composition porogen during a given scaffold's preparation, or alternatively it was added to pre-made scaffolds. The former route produced homogeneously-dispersed PCL-embedded grains (EMB-$CaSi_2$/PCL), where the latter resulted in the production of randomly-dispersed free-standing grains (RD-$CaSi_2$/PCL). Furthermore, fluorescent tagging of CaP with fluorescein isothiocyanate (FITC) through alendronate (bisphosphonate amine) linkages was employed to assess calcified scaffolds. Alendronate exhibits a strong affinity for bone,[83] and such a strategy allows one to evaluate the distribution of CaP deposits within an extended 3-D PCL framework by the means of fluorescence microscopy.

One promising attribute of alendronate is its common use in osteoporosis treatment.[110] Josse and co-workers recently demonstrated that chemically modified calcium phosphates can be used as materials for bisphosphonate delivery.[123,124] On the other hand, Uludag *et al.* has demonstrated that bone morphogenetic proteins can be conjugated to bisphosphonate amines, such as alendronate, and subsequently released locally once the complex is attached to CaP *in vitro*.[125] Therefore, incorporation of bisphosphonates within calcified PCL scaffolds points towards numerous potential drug delivery applications.

5.1 Experimental

5.1.1 Immersion of Calcium Disilicide Powder in SBF

A SBF solution with ion concentrations nearly equal to those in human blood plasma was prepared from a literature procedure[52] as described in Chapter 3.

Varying amounts of $CaSi_2$ powder (Johnson Matthey) in the range of 2.0 mg to 18.0 mg were distributed among the wells of a tissue culture polystyrene well plate, and 3.0 mL aliquots of SBF were then added to each well. All samples were prepared in duplicate at a minimum. The well plate was placed into a 37±2°C oven for 1 hour to allow temperature equilibration; it was then sealed and remained in the oven undisturbed for 2 weeks. At the end of this soaking period, $CaSi_2$ powder from each well was transferred to test tubes using Pasteur pipettes along with the SBF which was subsequently removed by centrifugation. These samples were then triply washed with DI-water followed by centrifugation and drying at 37°C for $\geq$ 24 hr. The well plate itself, which contained layers of $CaSi_2$ powder loosely bound to the bottom of each well, was thoroughly rinsed with DI-water and dried at 37°C for $\geq$ 24 hr. For the subsequent SEM/EDX analysis, isolated $CaSi_2$ powder was simply dispersed onto carbon tape adhered to an aluminum thimble. $CaSi_2$ samples from the bottom of the wells were obtained by inserting adhesive carbon tape/aluminum thimbles facedown into each well.

5.1.2 Synthesis of Porous $CaSi_2$/PCL Scaffolds

Porous PCL scaffolds were prepared via a salt-leaching method.[122] Polycaprolactone (~2.5 g; M_n~60,000; Aldrich) was first dissolved in 35 mL of chloroform, and then this solution was mixed with a water-soluble porogen. Figure 40 summarizes the experimental procedure for the synthesis of two types of scaffolds for subsequent calcification assays. The chloroform was removed in two steps. It was first allowed to partially evaporate in air while the reaction beaker was immersed in an ultrasound bath to assure a homogeneous dispersion of solid particles within the slowly-gelling PCL. The beaker was then placed under vacuum for 12 hours to complete the evaporation. Once chloroform evaporates, PCL solidifies, and the porogen can be later removed by soaking scaffolds in DI-water. Since evaporation of chloroform had taken place in a glass beaker, the ultimate shape of all scaffolds was a porous cylindrical disk (5±1 mm x 70 mm) whose shoulders were slightly rounded, reflecting the morphology of the PCL/beaker interface. The porogen used in scaffold fabrication was either NaCl alone, a mixture of NaCl and $CaCl_2 \cdot 2H_2O$, or a mixture of NaCl and K_2HPO_4. The porogen was removed in two steps. A scaffold is first immersed in an excess of a rapidly-stirred DI-H_2O for 12 hours to remove most of the porogen, and then it is placed into a

RD-$CaSi_2$/PCL	**EMB-$CaSi_2$/PCL**
(1a) dissolve PCL in $CHCl_3$	(1b) dissolve PCL in $CHCl_3$
(2a) add porogen	(2b) add **$CaSi_2$** & porogen
(3a) evaporate $CHCl_3$	(3b) evaporate $CHCl_3$
(4a) salt-leaching	(4b) salt-leaching
(5a) dry	(5b) dry
(6a) add **$CaSi_2$** (*see Fig. 2*)	

Figure 40. Experimental procedure for fabrication of porous $CaSi_2$/PCL scaffolds.

Hirsch funnel attached to a water aspirator. DI-H_2O is passed through the scaffold until Cl^- is no longer detected with $AgNO_3$. The final scaffolds were dried under vacuum for 24 hours.

Calcium disilicide powder was either added to a mixed-composition porogen during a given scaffold's preparation, which produced homogeneously-dispersed PCL-embedded grains (EMB-$CaSi_2$/PCL), or it was added to pre-made scaffolds, which produced randomly-dispersed free-standing grains (RD-$CaSi_2$/PCL). Amounts of porogen salts and $CaSi_2$, which were used during EMB-$CaSi_2$/PCL fabrication, were measured out by volume; these are presented in Table 5. Analogously, Table 6 refers to RD-$CaSi_2$/PCL, to which $CaSi_2$ was added after the salt-leaching/drying steps and in sub-milligram amounts. Here, the concentration of $CaSi_2$ was also systematically varied, but within this low concentration range the impact of this variation did not have any effect on this type of scaffold's biomineralization. Figure 41 illustrates the process of loading $CaSi_2$ powder into pre-made porous PCL discs to produce RD-$CaSi_2$/PCL. Once the powder is placed on top of a scaffold and into the pores, this local silicide-loaded area is covered by another piece of the same scaffold. An electric drill press equipped with a steel tube is then used to drill tablets out of the PCL discs. This method produces sandwich structures, each composed of two fused porous PCL tablets (6 mm in diameter x 5±1 mm think), one of which is loaded with $CaSi_2$. As the penetration of the spinning tube blade through a scaffold comes to completion, the resulting PCL tablet becomes inserted inside the tube. In the meantime, the tube continues to rotate along with a sample on the inside. This is when $CaSi_2$ grains, which are initially placed in the center of a RD-$CaSi_2$/PCL sandwich structure, become distributed throughout the sample, localized primarily in the bottom tablet. Once the power is turned off, the tablet can be easily pushed out using a stirring rod. After a sandwich structure is removed from the drilling tube, it takes a considerable amount of force to pull the two tablets apart. The rough surfaces of these tablets fuse under a small pressure applied by the drill, and the sandwich structures are able to remain intact throughout all subsequent treatments (SBF exposure, various washing steps, *etc.*).

EMB-$CaSi_2$/PCL	PCL	NaCl		K_2HPO_4		$CaSi_2$		Yield
	g	mL	g	ml	g	ml	g	g
1.1	2.504	24.0	33.02	—	—	1.0	1.032	3.364
1.2	2.493	23.0	32.32	—	—	2.0	2.686	4.886
1.3	2.450	22.0	31.17	—	—	3.0	4.321	6.386
2.1	2.527	22.0	31.46	2.0	2.697	1.0	1.031	3.321
2.2	2.523	21.0	29.23	3.0	4.039	1.0	1.031	3.367
2.3	2.524	20.0	28.24	4.0	5.350	1.0	1.030	3.241

Table 5. Synthesis of EMB-$CaSi_2$/PCL scaffolds.

RD-$CaSi_2$/PCL	PCL	NaCl		$CaCl_2 \cdot 2H2O$		K_2HPO_4		Yield
	g	mL	g	ml	g	ml	g	g
1.1	2.525	22.5	30.20	2.5	2.485	—	—	2.398
1.2	2.496	20.0	27.48	5.0	4.494	—	—	2.393
1.3	2.501	17.5	23.50	7.5	7.350	—	—	2.353
2.1	2.515	22.5	30.46	—	—	2.5	2.835	2.467
2.2	2.508	20.0	26.15	—	—	5.0	6.050	2.404
2.3	2.537	17.5	23.42	—	—	7.5	8.523	2.466

Table 6. Synthesis of RD-$CaSi_2$/PCL scaffolds.

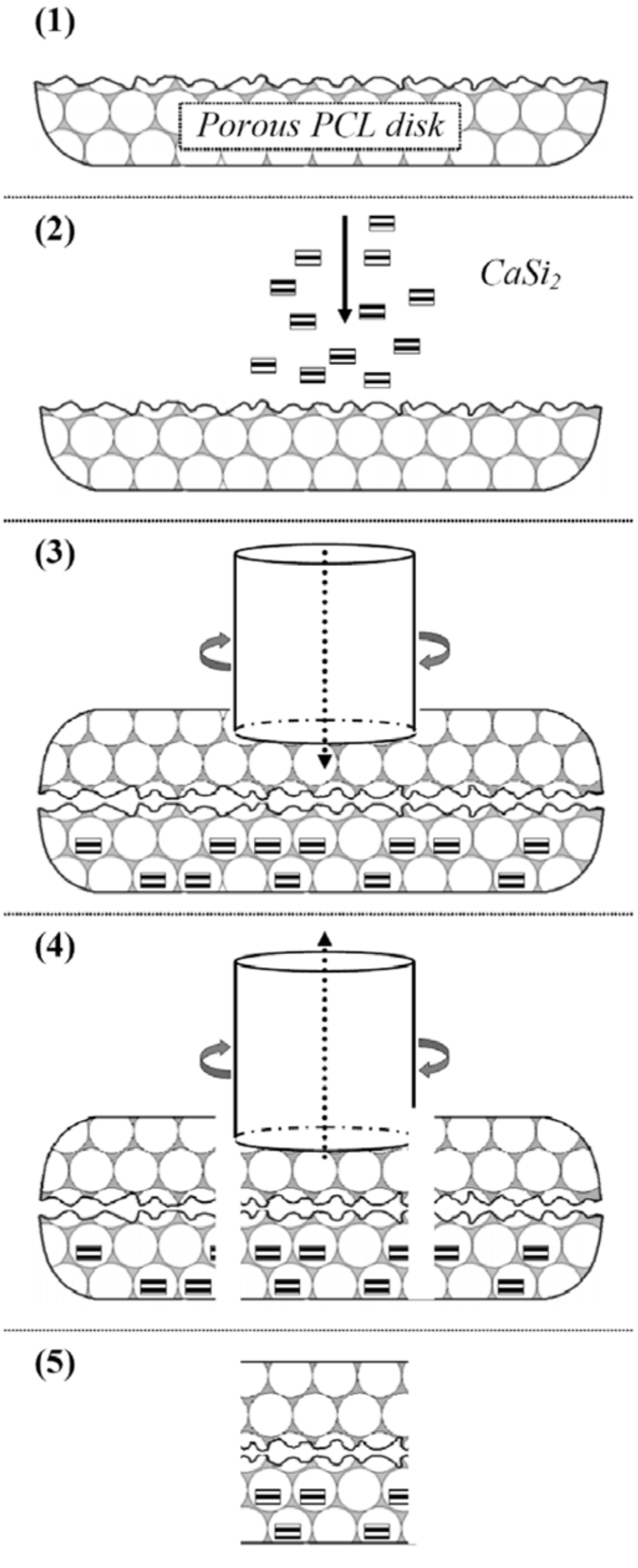

Figure 41. Schematic illustration of porous RD-$CaSi_2$/PCL fabrication process.

5.1.3 Immersion of Porous $CaSi_2$/PCL Scaffolds in SBF

RD-$CaSi_2$/PCL scaffolds were immersed in the SBF in the form of two-tablet sandwich structures (see above), while analogous $CaSi_2$-free sandwiches and single tablets were used as controls. In the case of EMB-$CaSi_2$/PCL scaffolds, only single tablets were used. Each sample was first placed on a piece of filter paper and into a Hirsch funnel attached to a water aspirator. A Pasteur pipette was used to add 5 mL of the SBF solution dropwise on top of a scaffold under mild suction filtration; this was done in order to improve scaffold wettability. As in the case of $CaSi_2$ powder, scaffolds were then distributed among the wells of a well plate, and 3.0 mL aliquots of SBF were added to each well. The well plate was placed into a 37±2°C oven for 1 hour to allow temperature equilibration; it was then sealed and remained in the oven undisturbed for periods of 2 and 4 weeks. Those scaffolds which were exposed to SBF for a month were removed from the SBF after the initial 2-week period, washed again with a fresh solution of SBF, and immersed in fresh 3.0 mL aliquots of SBF for the duration of the remaining 2 weeks. At the end of each calcification assay, scaffolds were thoroughly washed with an excess of DI-H_2O (in a manner similar to the washing with SBF), dried in the air for 12 hours and then under vacuum for 24 hours.

5.1.4 Fluorescent Tagging of RD-$CaSi_2$/PCL Scaffolds

The fluorescent tagging strategy employed in these experiments is the same as the one used to functionalize calcium disilicide/CaP deposits on silicon wafer structures (see Chapter 3). Coupling reactions between CaP and alendronate, $(H_2O_3)_2C(OH)(CH_2)_3NH_2$,[89] were performed by immersing calcified RD-$CaSi_2$/PCL scaffolds (alongside the SBF-exposed $CaSi_2$-free controls) in 2.0 mL aliquots of an aqueous alendronate solution (5.0 mM) for 12 hours. This occurs after a pre-wash step with alendronate to improve wettability. After alendronate exposure, samples were washed with DI-water (as before), followed by coupling reactions with a fluorescent tag. The specific fluorescent probe used here was fluorescein isothiocyanate (FITC, λ_{em}=520 nm), with the coupling procedure performed by a simple immersion of the corresponding scaffold in a 2.0 mL aliquot of 1.0 mM FITC solution in DMSO/H_2O (2:5) in the dark at 4°C. The duration of FITC exposure was typically 12 hours. Prior to fluorescence detection, the wafers were washed with DI-water and dried under vacuum for 12 hours at room temperature.

5.1.5 Silicic Acid Release from EMB-$CaSi_2$/PCL Scaffolds in SBF

Silicic acid release assays were performed using those EMB-$CaSi_2$/PCL scaffolds which had the same concentrations of incorporated $CaSi_2$. Scaffold tablets were prepared in sets of 10 from four different scaffolds (see Table 7 in Section 5.2.3) and inserted into 100-mL volumetric flasks. The SBF solution was added in 75 mL aliquots to each flask, which were then thoroughly shaken to remove air bubbles. The solutions were then made up to the mark, and glass tubes, which had slightly smaller diameters than the necks of the flasks, were inserted into each flask so that the scaffold tablets were fully submerged. A spectrophotometric molybdate assay[126] was performed after the samples remained in the 37±2°C oven for 2 weeks while being thoroughly shaken twice a day for the duration of the SBF exposure.

Prior to performing the molybdate assay for dissoluble silica, samples were allowed to cool to room temperature. Duplicate 10.00 mL aliquots of each SBF solution were analyzed alongside DI-H_2O & SBF controls and standard aqueous solutions of

$Na_2SiO_3 \cdot 5H_2O$ as follows: first, 5.00 mL of HCl (0.25M) were added to each flask, followed by 5.00 mL of an aqueous solution of $(NH_4)_6Mo_7O_{24} \cdot 4H_2O$ (5%) and 5.00 mL of an aqueous solution of disodium EDTA (1%); solutions were thoroughly swirled after each step. Ten to fifteen minutes after the addition of the molybdate, 10.00 mL of an aqueous solution of sodium sulfite (17%) were added, and samples were allowed to equilibrate for 30 minutes prior to the UV-Visible absorption measurements. The absorbance of each solution was measured against a DI-H_2O blank using a wavelength of 700 nm. The UV-Visible absorption measurements were performed using a Beckman Coulter DU 800 spectrophotometer at a resolution of 1 nm.

5.1.6 Characterization of Scaffolds

Scaffold surface analysis was done using a JEOL JSM-6100 Scanning Electron Microscope (SEM) coupled with an Energy Dispersive X-Ray (EDX) Analysis detector under an accelerating voltage of 20 kV. In contrast to EMB-$CaSi_2$/PCL, RD-$CaSi_2$/PCL scaffolds are too insulating to be imaged under SEM directly. These had to be inserted into tailored aluminum thimbles, such that the entire tablet was surrounded by the aluminum except for the surface. The scaffold surface was then sputtered with a 5 nm gold film. Alternatively, some scaffolds were sputtered with a carbon film, which improves conductivity and is transparent to this EDX detector, but partially melts the scaffold surface during the deposition. Therefore, the use of gold was preferred. For the sake of consistency, conductive EMB-$CaSi_2$/PCL scaffolds were prepared for the SEM analysis in a similar manner. The extent of alendronate coverage was evaluated via fluorescence measurements performed on fluorescently labeled samples using a Nikon Optiphot-2 fluorescence microscope with a Santa Barbara Instruments Group CCD and an Ocean Optics S2000 fiber optic spectrometer.

5.2 Results

5.2.1 Fabrication of Porous PCL Disks and Tablets

During the fabrication of porous scaffolds via a salt-leaching method, the complete encapsulation of porogen grains by a polymer is expected to take place. As a result, a fraction of a porogen material will remain entrapped within the final scaffold. If the fabrication process is performed on a macroscopic scale, the concentration of such residue is rather insignificant. Nonetheless, as tissue-engineering scaffolds undergo degradation *in vivo*, the release of these impurity particles may potentially affect biomineralization mechanism. The porogen salts which were selected for fabrication of PCL scaffolds (NaCl, $CaCl_2 \cdot 2H_2O$, and K_2HPO_4) are already present in the blood plasma. The local release of Ca^{2+} and HPO_4^{2-} ions from within the matrix is expected to increase saturation of the medium with respect to hydroxyapatite and promote a given scaffold's biomineralization.

EMB-$CaSi_2$/PCL and $CaSi_2$-free/PCL scaffolds take the shape of round-shouldered disks when PCL solidifies at the bottom of a beaker mold. Maximum pore volumes within PCL relative to the total volume of scaffolds, *i.e.* porosity, can be calculated using a given disk dimensions (5 mm x 70 mm) and the total porogen volume (25 mL). This value is over 100%, which reflects some loss of material during scaffold fabrication. As the polymer gels due to evaporation of chloroform, capillary forces cause the deposition of a thin PCL film along the walls of a container, which is detached from the final scaffold disk. Porosity values were determined experimentally using indirect measurements such as saturation of scaffolds with ethanol[11] or N_2 (BET). The former method lacks precision and produces a value of 95 ± 5%. Furthermore, since scaffolds cannot be outgassed at temperatures above the 60°C melting point of PCL (temperatures above 300°C are needed to completely remove H_2O), porosity values greater than 93%, obtained from BET measurements are also debatable. Nonetheless, both RD-$CaSi_2$/PCL and EMB-$CaSi_2$/PCL are very porous, and the average porosity value is assumed to be $\geq 90\%$.

In principle, pore diameter is dependent on porogen grain size; however, NaCl, $CaCl_2 \cdot 2H_2O$, and K_2HPO_4 have different average grain diameters and are hygroscopic. Uptake of water by these salts results in clustering of the porogen; therefore, the pore size distribution within these PCL scaffolds is random. Aside from the salts, there is another type of porogen present during scaffold fabrication process. Initial slow evaporation of chloroform takes place while the gelling PCL is agitated by the ultrasonic waves, which causes formation of microscopic bubbles within the polymer. Subsequently, during rapid solidification of PCL under vacuum, these bubbles rupture and form additional pores. Such combination of two popular techniques for polymeric scaffold manufacturing, salt-leaching and microemulsion methods,[122] allows one to achieve maximum porosity at the expense of the control over pore morphology. As-prepared PCL disks have a varying surface morphology: they are smooth in those areas where PCL was in contact with a glass beaker (bottom and sides) and rough at the exposed surface. The former does not reflect the true porosity of a scaffold, but the contribution of such flat domains to the overall surface area is minimal in the case of fabricated scaffold tablets and sandwich structures. Machining of scaffolds using an electric drill press equipped with a steel tube prevents excessive deformation of the porous PCL. If scaffolds are simply cut into pieces with scissors, PCL irreversibly deforms under pressure, thereby reducing the overall number of the open pores at the scaffold surface. In addition, the tablet drilling method accounts for distribution of free-standing $CaSi_2$ grains throughout sandwich structures during preparation of RD-$CaSi_2$/PCL samples.

5.2.2 Distribution of $CaSi_2$ within Porous PCL Scaffolds

Use of a spinning tube blade to shape tablets of PCL from RD-$CaSi_2$/PCL composite scaffolds achieves two goals: (1) the uniform distribution of $CaSi_2$ grains throughout the sample, localized primarily in the bottom tablet; (2) a fusion of tablet segments, thereby forming sandwich structures able to remain intact throughout all subsequent treatments (SBF exposure, various washing steps, *etc.*). Figure 42 shows a typical surface morphology associated with as-prepared porous RD-$CaSi_2$/PCL scaffolds. Due to the sub-milligram amounts of $CaSi_2$ powder used in the fabrication process and its thorough distribution throughout a given tablet, very few grains are visible at the surface (not shown). In fact, these images are practically identical to the ones associated with $CaSi_2$-free/PCL scaffolds. Employing mixed-composition porogen with a certain degree of control over the three-dimensional grain arrangement, in principle, should allow one to “dial in” the local pore microstructure. Nonetheless, those scaffolds which were used in calcification studies are assumed to have an overall random pore diameter distribution (Figures 42A & 42B). Two distinct morphological features are commonly observed: flat solid surfaces (Figure 42C) and thin porous films (Figure 42D). The latter are expected to degrade even further in SBF. All RD-$CaSi_2$/PCL scaffolds exhibit the same type of morphology, *i.e.* the addition of minor amounts of $CaCl_2 \cdot 2H_2O$ or K_2HPO_4 to the NaCl salt, which is the major part of a mixed-composition porogen by volume, has an undetectable impact in this regard. The only

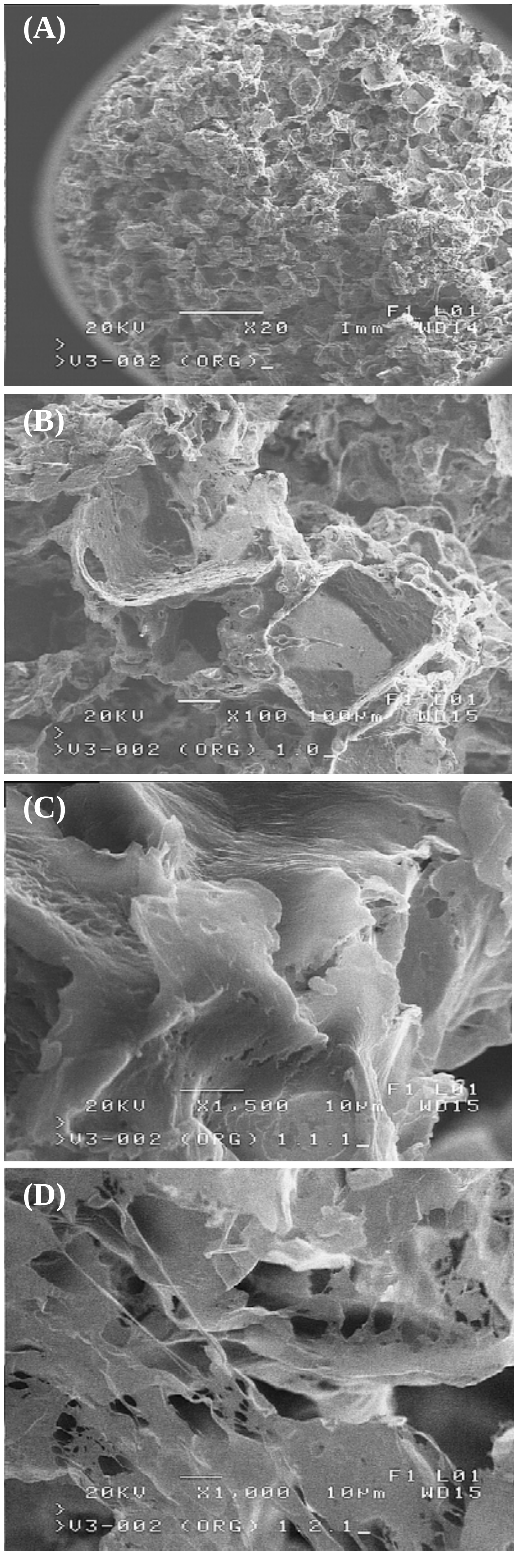

Figure 42. Plan view SEM of an as-prepared RD-$CaSi_2$/PCL scaffold: (A) surface of an entire tablet and (B-D) magnified views associated with (A).

observed difference between Ca^{2+} and HPO_4^{2-}-containing scaffolds is that the latter are slightly softer to the touch, and their average as-prepared weight is higher (see Table 6).

In contrast, the effect of using K_2HPO_4 as a co-porogen with NaCl rather than $CaCl_2{\cdot}2H_2O$ can be visually observed in the case of EMB-$CaSi_2$/PCL scaffolds due to the color difference. The metallic-gray color associated with Ca^{2+}-containing scaffolds, which is also characteristic of $CaSi_2$ powder, is significantly lighter in case of HPO_4^{2-}-containing scaffolds. This loss of color is directly proportional to the concentration of K_2HPO_4 in the porogen. An increased concentration of $CaSi_2$ within EMB-$CaSi_2$/PCL, results in stiffer and darker scaffolds. Under SEM imaging, as-prepared porous EMB-$CaSi_2$/PCL scaffolds closely resemble RD-$CaSi_2$/PCL samples (see Figure 42) with the exception of two additional morphological features which are due to the presence of $CaSi_2$: partially and fully PCL-covered $CaSi_2$ grains (see Figure 43A & 43B, respectively). The three-dimensional arrangement of grains in PCL is random, but the silicide distribution is uniform throughout any given scaffold.

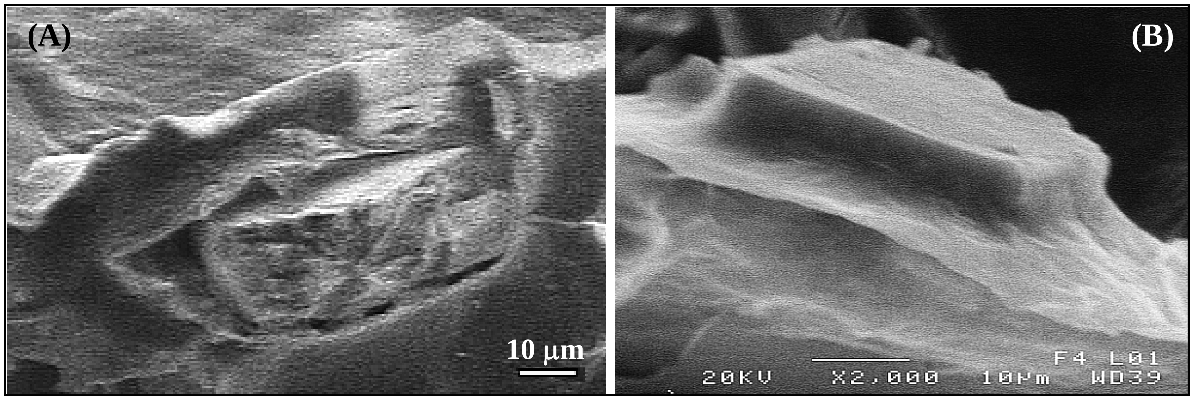

Figure 43. Plan view SEM of an as-prepared EMB-$CaSi_2$/PCL scaffold: (A) $CaSi_2$ grain which is partially embedded in PCL and (B) fully PCL-encapsulated grain.

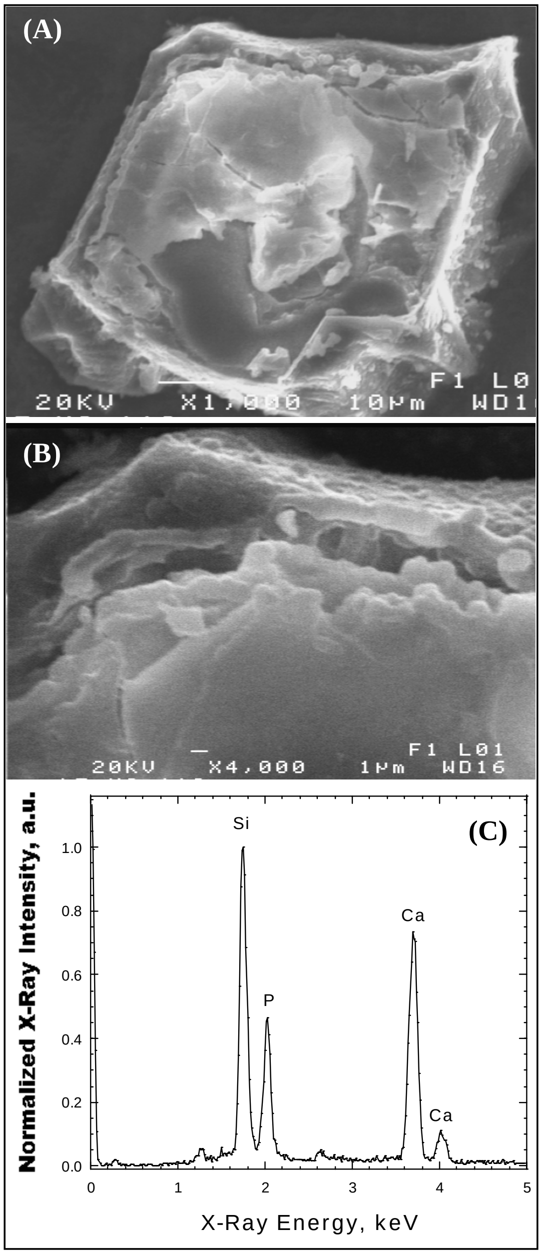

Figure 44. Plan view SEM of a calcified grain after 2-week soak of $CaSi_2$ powder in SBF: (A) entire CaP-coated grain, (B) the magnified view associated with the top-left corner of this grain, and (C) the EDX spectrum associated with (B).

5.2.3 Calcification of $CaSi_2$ and PCL Scaffolds

The study of the biomineralization mechanism of calcium disilicide growth layers on silicon wafers (Chapter 4) has shown that the deposition of CaP films on planar Si substrates in SBF is preceded by the release of Ca^{2+} from within $CaSi_2$ grains due to partial delamination of silicide layers. As this work demonstrates, standalone $CaSi_2$ grains can facilitate a biomineralization process as well; in fact, the rate of CaP deposition on polymer-embedded $CaSi_2$ is greater than when the grains are attached to a Si wafer (as evidenced by SEM analysis). The powder calcified successfully within two weeks of SBF exposure, a week faster than the previous results (see Chapter 4). Under SEM imaging, CaP film appears to coat isolated grains (see Figure 44), but it also deposits as a thin film along the bottom of the reaction container (see Figure 45). It must be noted that locating isolated CaP deposits is difficult in case of those samples in which the concentration of powder is greater than 10 mg of $CaSi_2$ per 3.0 mL of SBF. A random 3-D arrangement and excess of $CaSi_2$ grains implies an abundance of discrete nucleation centers and, in turn, a deposition of a larger number of

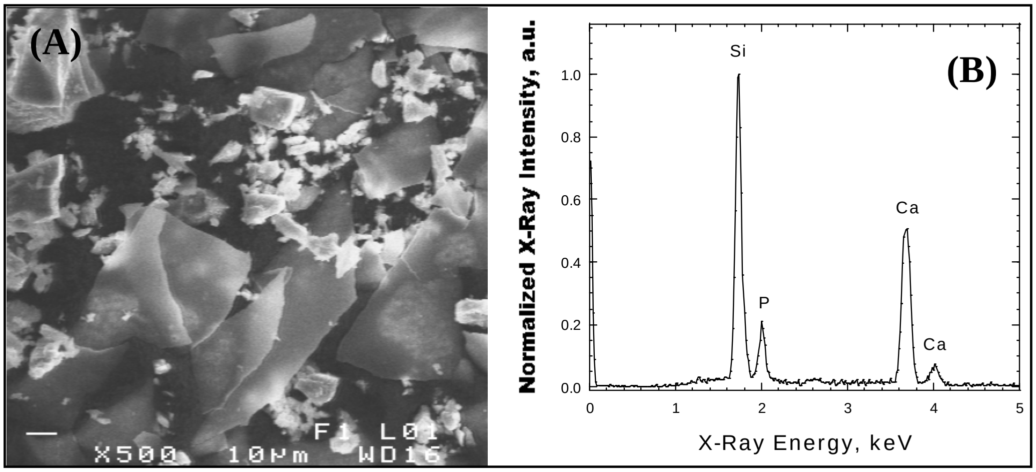

Figure 45. CaP film formed at the bottom of the reaction container during 2-week soak of $CaSi_2$ powder in SBF: (A) plan view SEM and (B) the EDX spectrum associated with (A).

discrete CaP structures which are then smaller and less-visible, as a result. Nonetheless, the presence of CaP is evident in all of the samples, as assessed by SEM/EDX.

The biomineralization of all $CaSi_2$-containing scaffolds is preceded by structural decomposition of calcium disilicide grains, but the rate of layer delamination is dependent on the type of a given scaffold. The break down of the $CaSi_2$ laminar structures within RD-$CaSi_2$/PCL is almost complete by the end of 2 weeks in SBF, while in the case of EMB-$CaSi_2$/PCL scaffolds, this process is retarded (see Figure 46). Decomposition of those grains, which were encapsulated entirely within PCL prior to SBF exposure, is significantly slower on the same time scale (Figure 46B). Delamination of those $CaSi_2$ grains within EMB-$CaSi_2$/PCL which are partially covered by the PCL initiates heterogeneous growth of CaP in SBF. In this regard, the mechanism of CaP deposition is similar to the calcification of calcium disilicide growth layers on silicon wafers (see Chapter 4). Figure 47 shows such $CaSi_2$ grains which were exposed to SBF for 2 and 4 weeks, respectively; these images are of two representative samples rather than of the same scaffold. Due to the lack of phosphorous peak in the EDX spectrum, the biomineralization product associated with a two-week sample

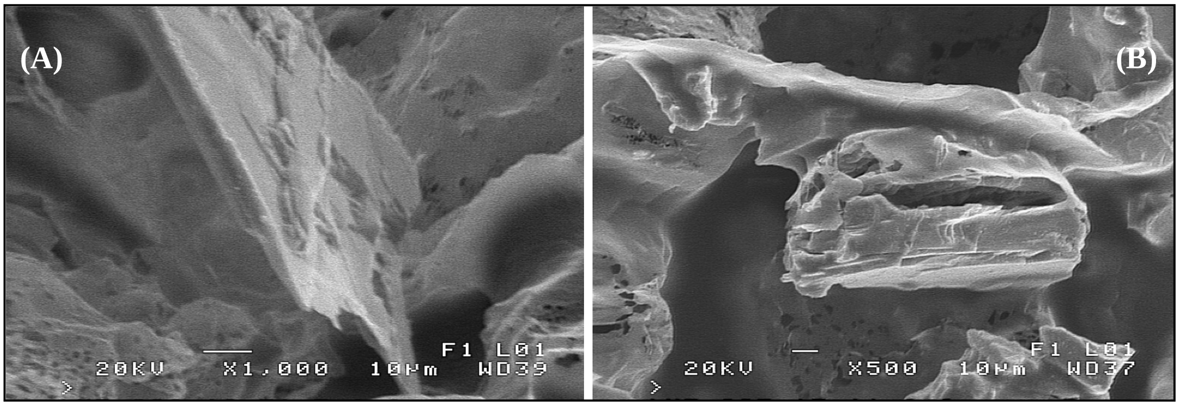

Figure 46. Plan view SEM of delaminated $CaSi_2$ grains within porous PCL scaffolds after 2 weeks in SBF: (A) RD-$CaSi_2$/PCL and (B) EMB-$CaSi_2$/PCL.

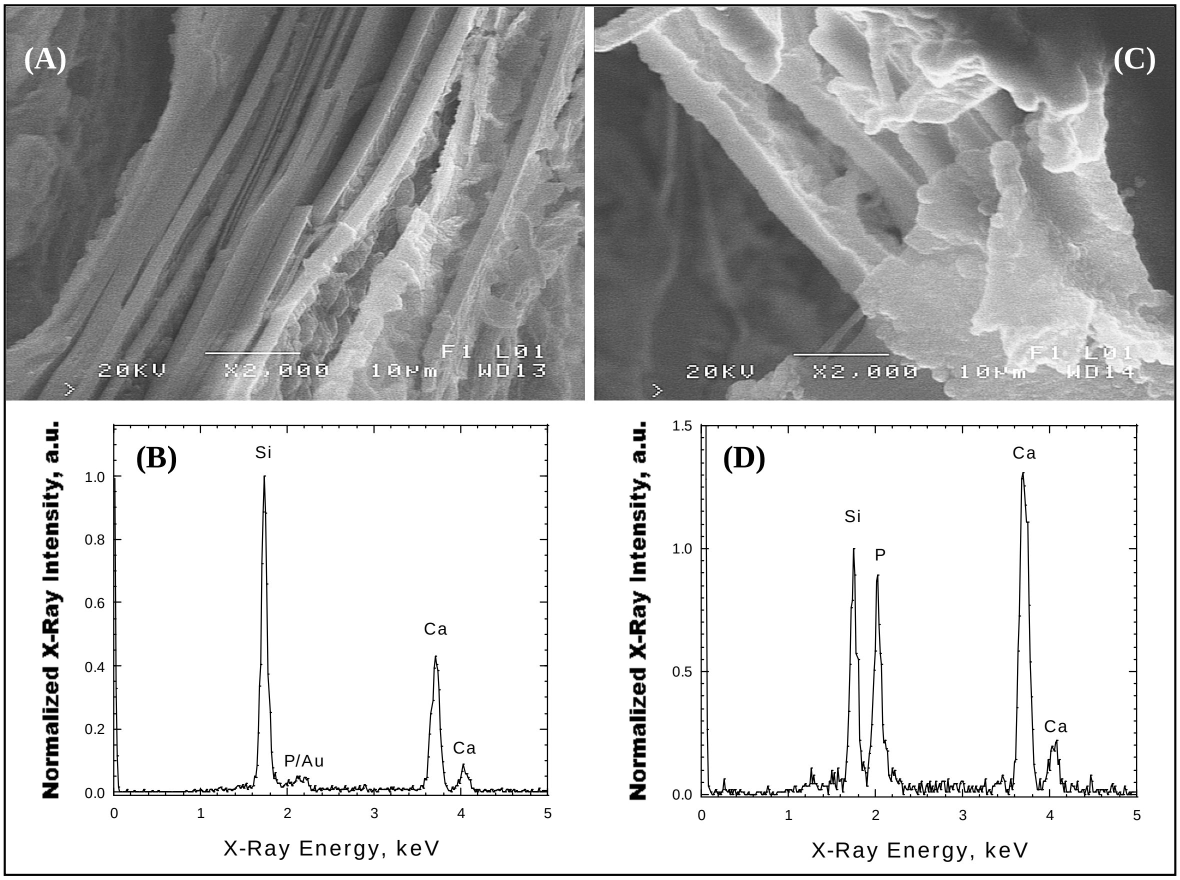

Figure 47. Biomineralized $CaSi_2$ grains within EMB-$CaSi_2$/PCL scaffolds: (A-B) plan view SEM/EDX spectra after 2 weeks and (C-D) after 4 weeks.

is most likely a calcium carbonate phase. An additional 2 weeks immersion in SBF results in its transformation into calcium phosphate (Figure 47C & 47D). Since the deposition of CaP is dependent on concurrent silicide delamination, such slow CaP growth indicates the importance of the PCL degradation: more $CaSi_2$ grains may be able to participate in the biomineralization process as the polymer dissolves. This point is further supported by the observation of the fast decomposition of $CaSi_2$ grains within RD-$CaSi_2$/PCL scaffolds, which results in the formation of CaP in just 2 weeks. During the SEM/EDX analysis of calcified RD-$CaSi_2$/PCL scaffolds, CaP deposits, such as the ones shown in Figure 48, were found exclusively in the neighborhood of decomposed calcium disilicide grains. CaP structures, comprised of 1-10 μm diameter spherulites, take on various three-dimensional shapes depending on the local microstructure of the PCL host.

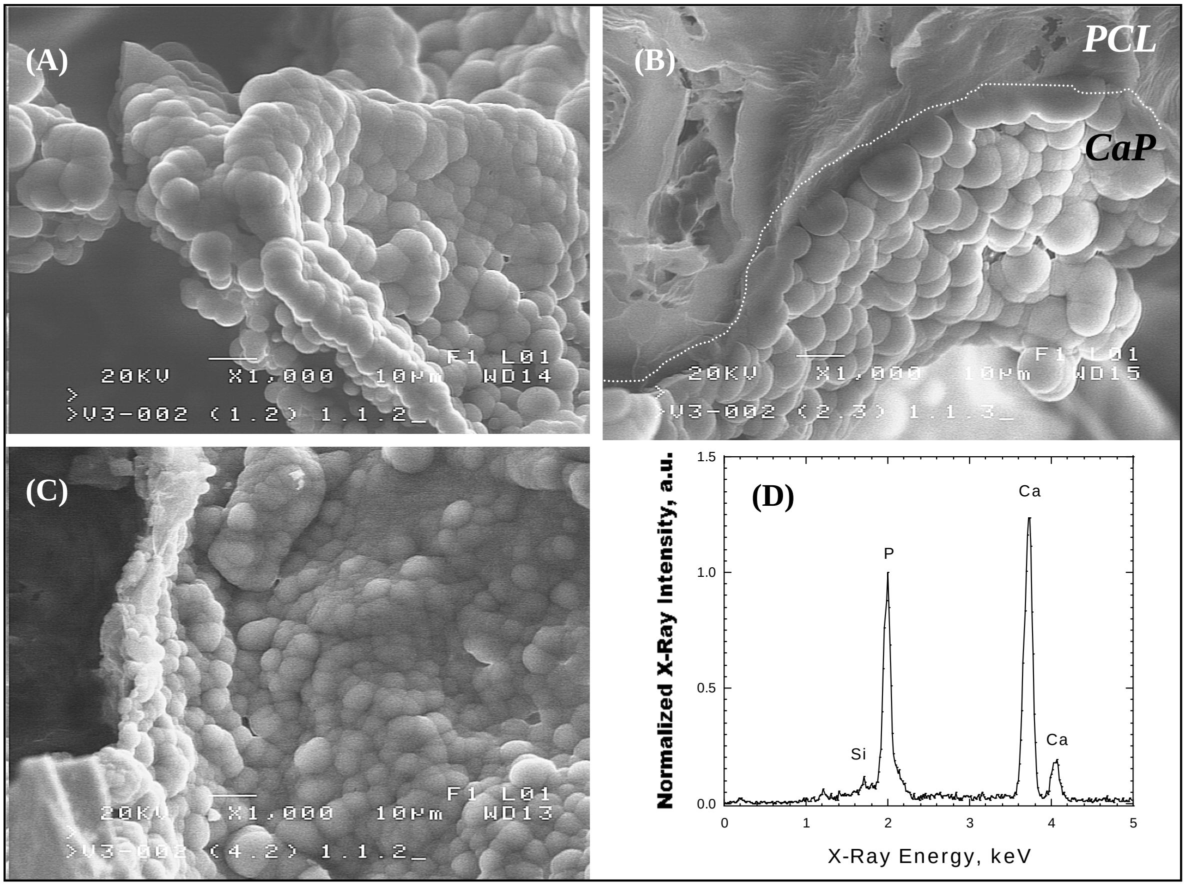

Figure 48. CaP deposits found within various RD-$CaSi_2$/PCL scaffolds which were immersed in SBF for 2 weeks: (A-C) plan view SEM images and (D) the typical EDX spectrum associated with all three images.

The concurrent processes of CaP deposition and the delamination of $CaSi_2$ grains are accompanied by the slow release of silicon in the form of orthosilicic acid [$Si(OH)_4$]. Silicon, which is an important dietary supplement,[127] is present in human blood plasma at concentration levels less than 1 mg/L.[25] It has been suggested in the literature that the bone formation is positively affected by the 20-50 mg/day dietary intake of silicon.[72,127,128] $CaSi_2$ grains on Si wafers are known to undergo complete structural delamination within the first 10 days of the SBF exposure (see Chapter 4). As shown in Table 7, an average EMB-$CaSi_2$/PCL scaffold tablet releases ~20 mg/L of $Si(OH)_4$ during the initial 2 weeks in SBF, which corresponds to the silicon release rate of < 0.5 mg/L per day. *In vivo*, this would amount to the < 2.5 mg Si/day intake (assuming ~ 5 L of blood per average person), the value which is well below the required dietary minimum.

EMB-$CaSi_2$/PCL (see Table I)	Weight (tablet)	H_4SiO_4 (released)
	mg	mg/L
1.1	30.7 ± 2.0	18.3 ± 1.6
2.1	30.4 ± 1.5	29.4 ± 5.7
2.2	29.7 ± 2.2	23.6 ± 0.7
2.3	28.7 ± 1.3	18.8 ± 1.4

Table 7. Silicic acid release from EMB-$CaSi_2$/PCL scaffolds.

Immersion of $CaSi_2$-free/PCL control scaffolds in SBF for either 2 or 4 weeks did not result in CaP formation, as assessed by SEM/EDX. All EDX spectra, which were obtained from Ca^{2+}- and HPO_4^{2-}-containing scaffolds before and after SBF exposure, show neither calcium nor phosphorous peaks. The lack of CaP growth due to the absence of $CaSi_2$ was further confirmed when all SBF-exposed scaffolds were fluorescently tagged with FITC-alendronate moieties. Since alendronate specifically binds to calcium ions, this assay, when applied to as-prepared $CaSi_2$-free/PCL, also confirms the lack of calcium chloride incorporation into PCL during the scaffold fabrication process. Figure 49 is a fluorescent image of FITC-labeled alendronate-derivatized CaP on a $CaSi_2$ grain within a calcified RD-$CaSi_2$/PCL scaffold. The emitted 520 nm green light is detected only at the locations of calcified $CaSi_2$ grains. The PCL matrix around these areas, as well as all of the control samples, is non-fluorescent, which indicates the absence of calcium available for binding with alendronate.

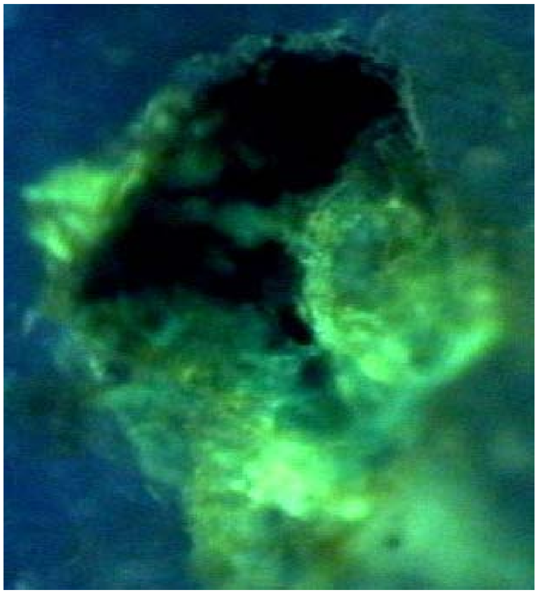

Figure 49. FITC-labeled alendronate-derivatized CaP on a $CaSi_2$ grain within a calcified RD-$CaSi_2$/PCL scaffold.

5.3 Discussion

The structural delamination of crystalline $CaSi_2$ grains, in which silicon sheets are intercalated with calcium, is responsible for the striking similarities between biomineralization behaviors of $CaSi_2$ and Bioglass^{TM} (Chapter 1-4). The five-stage mechanism for hydroxycarbonate apatite formation on the surface of bioactive glass, formulated by Hench *et al.*,[24] dictates that upon proper surface erosion, calcium and phosphate ions within bioglass migrate to the surface and form a CaO-P_2O_5-rich film on top of the SiO_2-rich layer.[24] This, in turn, triggers the growth of amorphous calcium phosphate through electrostatic ion accumulation and its later crystallization into various apatites.[24] In Chapter 4, it has been determined that when $CaSi_2$ is anchored to a silicon wafer, the degradation of laminar Ca^{2+}-rich grains (and the associated local release of calcium) is a prerequisite to CaP deposition. This delamination of $CaSi_2$ grains, which are partially buried in silicon, comes to completion within 10 days of the SBF exposure. Concurrently, $CaSi_2$ acquires a negative surface charge through surface hydrolysis and adsorption of phosphates. Finally, the growth of CaP occurs when the initially-deposited spherical nuclei of calcium carbonate/silicate begin to acquire phosphates (in EDX-detectable amounts) through ion exchange with the solution. This presumably occurs by the end of the third week in SBF.

The biomineralization of porous $CaSi_2$/PCL scaffolds is initiated solely by the inorganic phase and can be accelerated by the degradation of the polymer matrix. RD-$CaSi_2$/PCL calcified faster than EMB-$CaSi_2$/PCL due to the larger surface area of $CaSi_2$ which was exposed to the SBF. In the latter case, the calcification of $CaSi_2$ grains, which are partially embedded within PCL, occurs via the same mechanism as for the calcium disilicide growth layers on spark-processed Si (see Chapter 4), including the formation of transient calcium carbonate precursor phases. Delamination of $CaSi_2$ is accompanied by the release of $Si(OH)_4$, at a biologically-benign rate.

Finally, the preliminary electrodeposition experiments with concentrated EMB-$CaSi_2$/PCL indicate that these materials may also find applications as electronically-responsive orthopedic tissue engineering scaffolds. Recall that calcium disilicide is a semimetal (Chapter 1). Polycaprolactone, on the other hand, is an insulator. Under electric bias, the growth of CaP on $CaSi_2$ is significantly accelerated, and calcified $CaSi_2$/PCL scaffolds can be obtained within several hours. Furthermore, formation of Mg-rich CaP structures was observed when scaffolds were exposed to the SBF under bias (Figure 50), much like in the case of the previous work with bias-assisted calcification of $CaSi_2$ on Si (see Chapter 3). The mechanism of magnesium incorporation into naturally occurring carbonates and apatites by various biological organisms and the possibility of carbonated apatite formation by the way of transient precursor phases are questions that continue to challenge researchers in the field of biomaterials.[53] The further exploration of $CaSi_2$ biomineralization behavior may increase the understanding of these two phenomena.

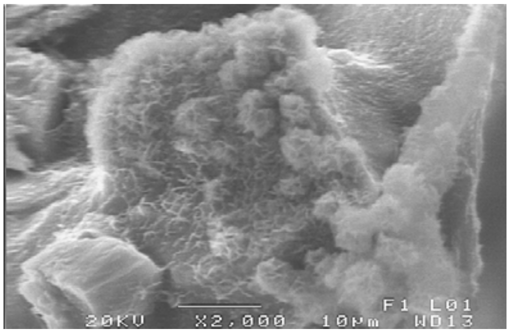

Figure 50. A plan view SEM of Mg-rich CaP deposits on an EMB-$CaSi_2$/PCL scaffold which was exposed to SBF under bias (1 mA) for 5 hours.

5.4 Summary

Biodegradable and bioactive scaffolds for bone tissue regeneration can be obtained through the incorporation of $CaSi_2$ grains within PCL frameworks. Matrix porosity values over 95% can be achieved by employing a combination of salt-leaching and microemulsion techniques for polymer scaffold processing. Calcium disilicide powder can either be added to a mixed-composition porogen during a given scaffold's fabrication to produce homogeneously-dispersed PCL-embedded grains (*EMB*-), or it can be added to pre-made scaffolds which will then result in the random dispersion of free-standing grains within PCL (*RD*-). Scaffolds of the first type may find further applications in the field of bioelectronics due to the unique semimetallic properties of $CaSi_2$. The second method for seeding porous PCL networks with bioactive $CaSi_2$ may be useful when low loading levels and controlled positioning of a bioactive material within a scaffold is needed. The process of $CaSi_2$/PCL scaffold calcification under zero bias, during which calcium phosphate growth is significantly dependent on the structural degradation of $CaSi_2$ grains, has a similar mechanism as the CaP growth on bioactive glasses/ceramics. The biomineralization of these scaffolds is initiated solely by the inorganic phase and can be accelerated by the degradation of the polymer matrix. As a consequence, RD-$CaSi_2$/PCL facilitates deposition of CaP at a slightly faster rate than the scaffolds of the *EMB*- type. Successful fluorescent tagging of CaP within calcified PCL scaffolds using fluorescein isothiocyanate through alendronate (bisphosphonate amine) linkages implies that these materials may potentially be used in drug delivery applications.

Part II

CHAPTER VI.

Literature Review

6.0 Introduction

6.0.1 The Age of Silicon

Since 1954, the year when Gordon Teal of Texas Instruments introduced an operational silicon (Si) transistor, Si-based devices have been improving the quality of human life.[129] The age of silicon began in 1951 when Teal and Beuhler invented the method for single-crystal silicon growth,[130] and until now existing microelectronics technology has been dominated by silicon.[14,15] In 1965 Gordon Moore published a ten-year forecast predicting that the number of components on an integrated circuit would double every two years due to the continuing exponential increase of the complexity for a minimum cost of components.[131] Giant corporations grew from technologies based on tiny silicon chips,[132] extending the validity of the "Moore's Law" to the present day.

6.0.2 Future of Device Miniaturization

Continuing device miniaturization any further is, however, a problem.[133] For example, insulating transistor gates become conductive if made too small and thin. Despite the fact that device miniaturization is rapidly approaching its fundamental limit, silicon is still the optimal choice for electronic devices.[14] As an alternative to conventional scaling,[130,134] recent advances in process technology project that the miniaturization of integrated silicon circuits will continue (see reference 135 for an example).[15] Yet another actively researched strategy, which will ideally provide an enormous leap forward in device performance, is the fabrication of optical circuits.[136] Integrating optical and electronic systems will continue driving forward the existing microelectronic technology and produce devices which, potentially, may operate at the speed of light.

6.0.3 Developing a Silicon-Based Optoelectronic Platform

The speed of photons traveling through vacuum exceeds the maximum speed of electrons in an electrical circuit. Therefore, transporting information with light is the focus of a vast number of research projects in the fields of science and engineering. Integration of optical components into electronic systems accelerated since the discovery of novel properties (*e.g.* improved Si light emission[137]) that materials possess when reduced down to the nano-scale regime. Developing methods for building optically active device components on existing microelectronic platforms is the most practical strategy from the standpoint of economics. Compound (*e.g.* GaAs[138]) and elemental (*e.g.* Si, Ge) semiconductors are given the primary emphases in solid-state electronics.[139] As silicon is an established semiconducting platform, major research efforts are being directed toward fabrication of silicon optical device components (*e.g.* waveguide, detector, *etc.*) and, in particular, efficient light emitters on silicon. Progress toward silicon optoelectronic platform development recently reached a milestone when Liu and co-workers introduced a high-speed silicon optical modulator;[140] shortly thereafter, a miniaturized prototype of such a device was fabricated by Xu *et. al*.[141] However, a key device component, the efficient silicon light source, is still difficult to produce.[142] Unless silicon itself is made luminescent, the maximum switching speed of such optoelectronic devices will not be reached due to structural incompatibilities between silicon and direct gap emissive semiconductors.

Silicon is an indirect-band gap semiconductor and, unlike direct-band materials, does not have an inherent mechanism for practical light emission.[136,143] Yet, the limitations imposed by the silicon indirect band gap can be overcome in several ways.[144] For example, room-temperature luminescence can be obtained from porous silicon[145] or from locally strained silicon.[146] Rare earth incorporation into crystalline Si is another appealing strategy discussed in detail in the following sections. In particular, one area of emphasis in the Coffer research group is the development of new methods for doping nanostructured silicon (and recently germanium[147]) with erbium.[148]

6.1 Sensitization of Lanthanide Luminescence

Emission of light from Er^{3+}-doped Si nanocrystals is an exampled of sensitized lanthanide luminescence. An organic or inorganic sensitizer, in this case silicon, transfers energy to the rare-earth ion, thereby placing it into the excited electronic state. The so called ‘cold light’ is subsequently achieved when the electron radiatively relaxes down to the ground state. This process is outlined in Figure 51. If the applied electric potential is the source of the excitation energy, the process is referred to as ‘electroluminescence’ (EL). Alternatively, if the photoexcitation is used (*e.g.* by employing a focused laser beam as the source), the process is referred to as ‘photoluminescence’ (PL). In any practical application EL is usually preferred over PL, even at the expense of quantum yield (number of photons emitted per energy supplied), because electroluminescence is significantly more cost-effective. An efficient electroluminescent material used to replace street lights with ever-burning “semiconductor bulbs”, for example, could become the cornerstone of a multibillion dollar industry. The emission wavelength is dependent on the lanthanide identity.[149-152]

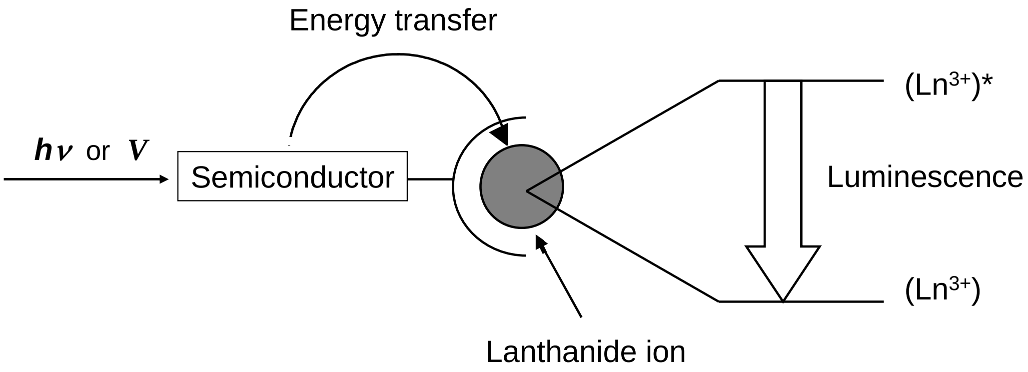

Figure 51. Sensitization of lanthanide luminescence by a semiconductor.

6.2 Photoluminescence of Erbium-Doped Silicon

When rare earth impurities are present within silicon, they bind excitons which transfer energy and emit photons by intracenter transitions between discrete energy states.[143,144] Erbium is of particular interest in this regard because its ($^4I_{3/2}$) → ($^4I_{15/2}$) luminescent transition at 1.54 μm lies at a transmission maximum for silica-based waveguides (see Figure 52).[151] Coffer *et al.* previously developed a method for kinetic trapping of erbium ions during the nucleation and growth of silicon nanoparticles in the gas phase (*vide supra*).[148,153] Recall that silicon is an indirect band-gap semiconductor. Photoexcited electrons within silicon nanoparticles cannot radiatively recombine intrinsically, unless a quantum-size effect is present.[137] However, a silicon nanoparticle has

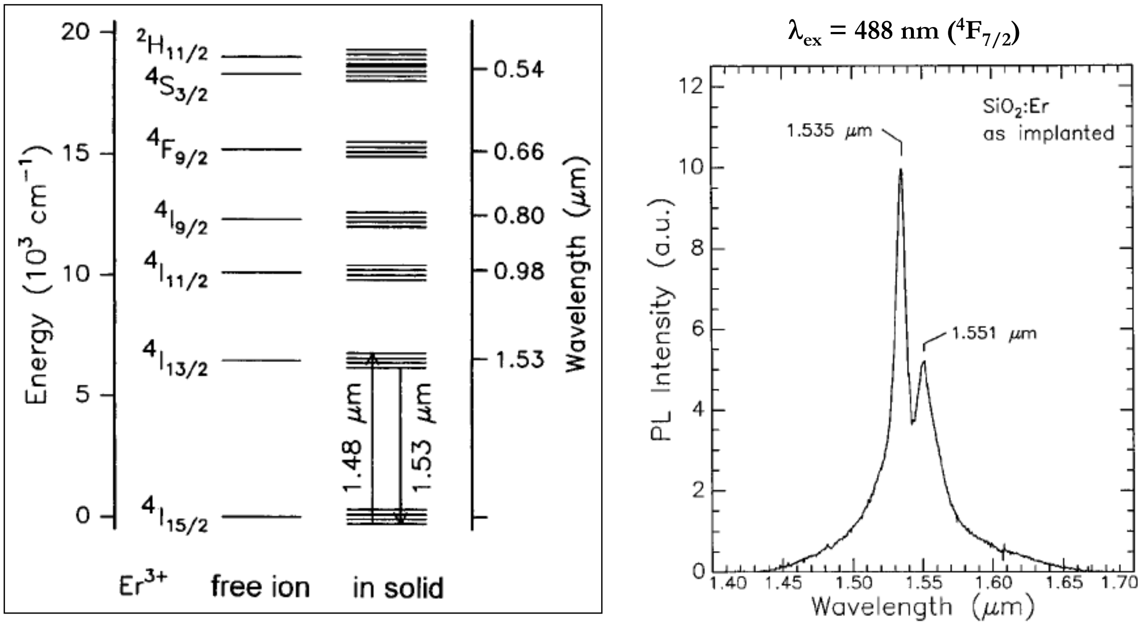

Figure 52. Schematic energy level diagram of Er^{3+} and room-temperature PL spectrum of Er-implanted amorphous Si:H,O. Taken from reference 151.

a much larger adsorption cross-section than an erbium ion, and, therefore, Si efficiently soaks up laser light during photoexcitation. An electron-hole pair (exciton), confined to the dimensions of a nanocrystal, transfers energy to erbium through a phonon-mediated process (Figure 53).[154]

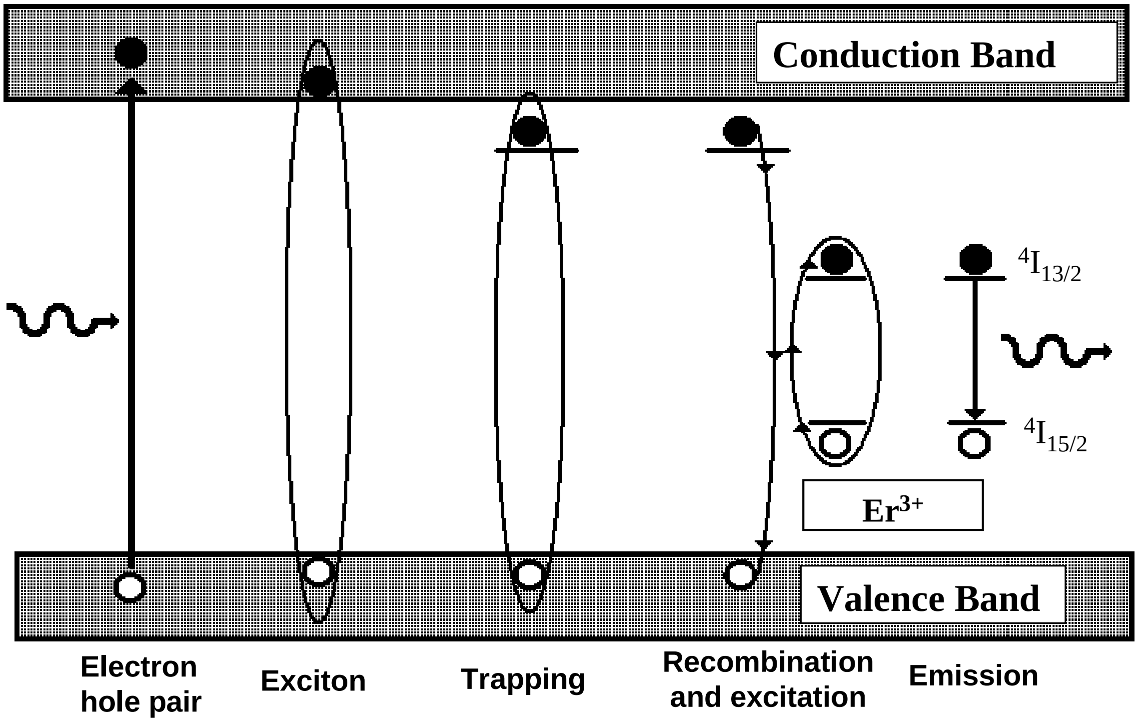

Figure 53. Schematic illustration of the energy transfer process from a silicon nanocrystal to the erbium ion. Taken from reference 155.

The efficiency of radiative electron-hole recombination through Er^{3+} centers within these randomly dispersed Er-doped Si nanocrystals (Er/Si-NCs) is relatively small.[155,156] First, the presence of deep surface states, associated with the fabrication process, presents additional nonradiative relaxation pathways for the excited electrons.[157] In addition, inter-erbium energy transfer via an Auger process,[143] energy back transfer from the excited Er^{3+} to

Si, or depopulation of trapped excitons may further decrease the quantum yield of Er/Si-NCs. The radiative relaxation mechanism competes with several other electron-hole recombination pathways, which do not result in light emission. In particular, the exciton can recombine non-radiatively using surface states whose energy lies within the silicon band-gap (see Figure 54). The conduction and valence bands of silicon are separated by an energy gap, within which electronic transitions are forbidden.[143] However, at the surface, accumulation of non-bonding electrons causes formation of so-called ‘surface states’ (*e.g.* dangling bonds) whose energy lies within this band gap. Here, a photo-excited electron can sequentially return to the valence band without light emission.

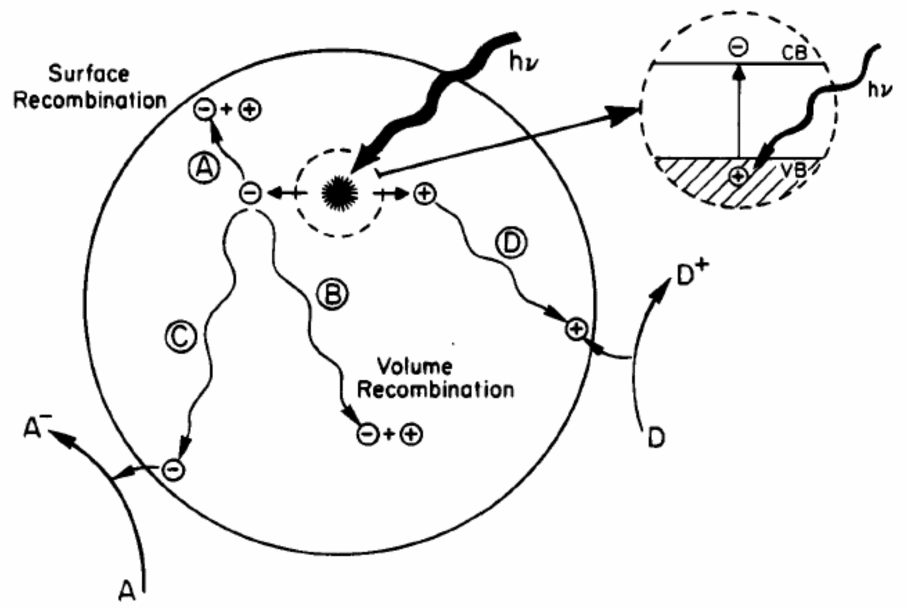

Figure 54. Schematic photoexcitation in a solid followed by deexcitation events. Taken from reference 158.

6.3 Improving Photoluminescence of Er/Si-NCs through Organic Surface Modification

The strategy which was previously used by Coffer *et al.* for passivating surface dangling bonds on Si nanocrystals involved the use of organic surface caps (see Figure 55).[159] An additional goal for this method, which was successfully achieved, was to improve the solubility of silicon nanocrystals in common solvents. When uncapped, they can only be dissolved in ethylene glycol, and this limits their applications to those which do not involve solution chemistry. Surface chemical modification with organic molecules improves nanocrystal solubility in a variety of solvents, but is accompanied by a reduction in photoluminescence efficiency.[159] As-prepared silicon nanocrystals have many surface defects which are the additional centers for the non-radiative electron-hole pair recombination. These are usually eliminated by prolonged high-temperature anneals, which destroy organic surface

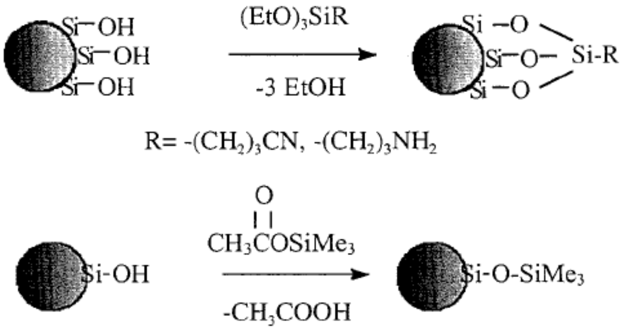

Figure 55. Reaction scheme of capping reagents (organic) with Si nanoparticles. Taken from reference 159.

caps. Any high-temperature anneal used to improve the room-temperature PL of Er-doped silicon[160] cannot be applied to these materials because it destroys the organic functionality and results in the clustering of discrete particles. Surface passivation with robust larger-bandgap inorganic materials, presented in this dissertation, is an alternative route to removing surface defects and thus achieving stronger luminescent Er/Si-NCs. Encapsulation of erbium-doped silicon nanocrystals with zinc oxide not only improves the luminescence efficiency, but also has a potential for the development of a multi-color emitter, since ZnO is a direct wide-band gap semiconductor which is capable of emitting UV-Visible light.[161]

6.4 Synthesis of Randomly Dispersed Erbium-Doped Silicon Nanocrystals

The procedure for the synthesis of erbium-doped Si nanocrystals was previously developed by John St. John, a former student in Coffer research group (Figure 56).[148,156] Er/Si-NCs are formed upon pyrolysis of helium-diluted disilane (0.48% Si_2H_6 in He) in the presence of $Er(tmhd)_3$ [tris(2,2,6,6-tetramethyl-3,5-heptanedionato)erbium (III)], an erbium CVD precursor. The erbium precursor resides in a warmed bubbler, upstream from the disilane entrance point. Helium passes through this bubbler at a controlled rate, mixes with the slowly-sublimating $Er(tmhd)_3$, and carries it through a quartz reactor down to the pyrolysis oven entrance. During a reaction time, both nucleation and growth of nanocrystals take place while the mixture of decomposed gases travels through the oven, heated to 1000^{o}C. The resulting Si nanocrystals containing aerosol then flows through a bubbler filled

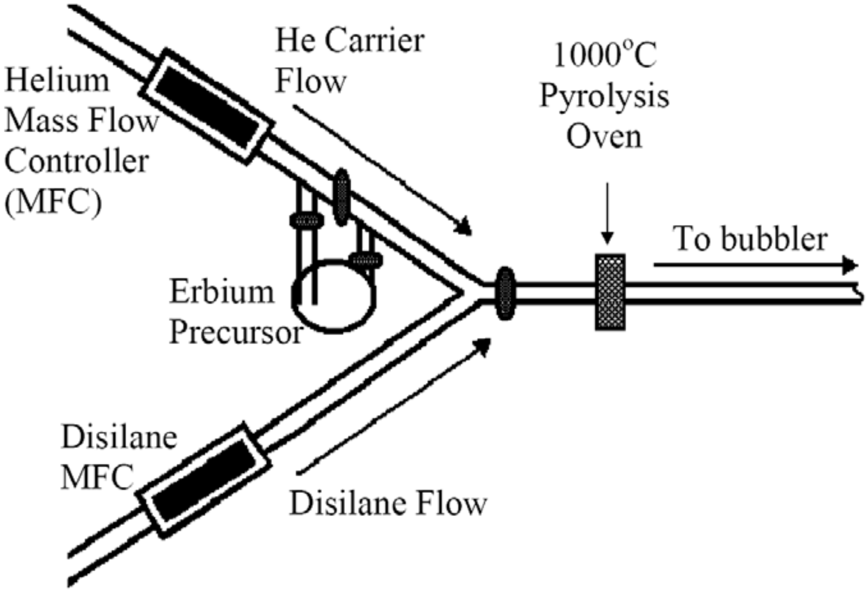

Figure 56. Schematic illustration of the pyrolysis system. Taken from reference 155.

with ethylene glycol where the particles are collected.

Particle sizes can be controlled by varying the oven length and disilane concentration.[148,153,155,156] The typical flow rates for disilane and the He stream which passes through Er-bubbler are 3.6 and 3000 sccm, respectively; these are controlled with mass flow controllers (MFC). A typical reaction runs for 24 hours. Within the isolated Er/Si-NCs, erbium is randomly dispersed throughout silicon lattice because during particle growth Si entraps erbium kinetically at non-equilibrium concentrations.[148, 155,156]

Part II

CHAPTER VII.

Research Synopsis

One strategy designed to achieve efficient light emission from nanocrystalline silicon (Si) involves the incorporation of rare-earth (erbium, europium, etc.) impurities into its framework. Previous work from Coffer laboratories have established that erbium-doped silicon nanocrystals (quantum dots) grown from the concomitant pyrolysis of disilane and an erbium source compound can emit at 1.54 micrometers, the wavelength of light which is the most compatible with existing silica-based fiber optics. Erbium photoluminescence is triggered by complex energy transfer mechanisms which involve various combinations of carrier(silicon)-mediated and direct excitation of erbium centers by 488 nm laser light. In an attempt to improve the photoluminescence efficiency of these nanocrystals by reducing interfacial defect density, several selective surface modification reactions with inorganic capping layers, comprised of either aluminum oxide (AlO_x) or zinc oxide (ZnO_x), were analyzed. This part of the dissertation presents synthetic routes for fabrication of AlO_x or ZnO_x coated Er-doped Si nanocrystals and their structural characterization. The results demonstrate the impact of inorganic surface modification on rare earth photophysics.

Part II

CHAPTER VIII.

Photoluminescence of Erbium-Doped Silicon Nanocrystals Encapsulated by Aluminum and Zinc Oxides

8.0 Overview

The speed of photons traveling through vacuum exceeds the maximum speed of electrons in an electrical circuit. Therefore, transporting information with light is the focus of a vast number of research projects in the fields of science and engineering. As silicon (Si) is an established semiconducting platform, major research efforts are being directed toward fabrication of efficient light emitters on silicon. When doped with erbium, silicon nanocrystals emit at 1.54 μm, which is a transmission maximum for silica-based waveguides. These randomly dispersed erbium doped Si nanocrystals (Er/Si-NCs) are prepared *via* pyrolysis of disilane in the presence of an Er^{3+} precursor.[156] However, the efficiency of radiative electron-hole recombination through Er^{3+} centers within Er/Si-NCs is relatively small (see Chapter 6).

This chapter presents routes to surface chemical modification of Er/Si-NCs with either aluminum oxide (AlO_x) or zinc oxide (ZnO_x) and characterization of the resultant products. Encapsulated nanocrystals of both types of surface caps show an improvement in erbium photoluminescence when compared to the uncapped control. Er/Si-NCs which were used in subsequent inorganic surface modification reactions were prepared using a 6 cm oven and have an average diameter of about 18 nanometers. Structural and photophysical characterization of all Si nanocrystals was performed by means of Transmission Electron Microscopy and steady-state room temperature near-IR Photoluminescence Spectroscopy, respectively.

8.1 Experimental

8.1.1 Synthesis of Er^{3+}-doped Si Nanocrystals

Randomly dispersed Er^{3+}-doped Si nanocrystals (Er/Si-NCs) were prepared according to the method developed previously by Coffer, *et al.*[148] In short, silicon nanoparticles are synthesized via pyrolysis of helium-diluted disilane (Si_2H_6; Praxair) in the presence of an erbium precursor [$Er(tmhd)_3$; Strem]. Both Si_2H_6 and $Er(tmhd)_3$ are carried to the reaction zone by He gas. Er/Si-NCs dots nucleate and grow as the aerosol mixture passes through a 6 cm-long oven, held at 1000°C (see Chapter 6). An ethylene glycol-filled dual bubbler, positioned downstream from the oven, is used for nanocrystal collection.

A series of sequential washing steps is employed to isolate Er/Si-NCs: (1) tetrahydrofuran [THF; reagent grade] is used to remove ethylene glycol; (2) absolute ethanol [EtOH] is then used to remove physisorbed erbium ions; and (3) spectrophotometric grade THF to reduce surface-bound hydrocarbon residue. The isolation process is completed by nanocrystal drying at room temperature under vacuum for $\geq$ 12 hours. Prior to PL measurements, Er/Si-NCs are annealed at 800°C under vacuum for 1 hour.

8.1.2 Encapsulation of Er/Si-NCs within Aluminum Oxide

During the surface modification with aluminum oxide, Er/Si-NCs (0.75±0.25 mg) are first dispersed in 15.0 mL of isopropyl ether [$(iPr)_2O$] using sonication. Aluminum isopropoxide [$Al(O\text{-}iPr)_3$; 25.00±5.00 mg; Aldrich) is added to a 25-mL round-bottom flask while it is still in the sonication bath. The flask is subsequently placed into an 85±5°C oil bath under N_2 atmosphere and a condenser; a magnetic bar is used to rapidly stir the reaction mixture for 2 hours. For the purpose of breaking up aggregates, after the initial 3-5 minutes of such equilibration, the flask is briefly removed from the oil bath and placed back into the sonicator for 1-2 minutes; thereafter, the flask is returned into the oil bath for the remaining 2 hours.

Next, aluminum oxide-coated nanocrystals (AlO_x/Er/Si-NCs) and the solvent are transferred to an Erlenmeyer flask and diluted with 60 mL of isopropanol. Upon 1 hour of sonication, solid particles (AlO_x/Er/Si-NCs and Si-free aluminum oxide) are isolated using centrifugation and dried under vacuum for 12 hours. The isolated product is then washed with 3 mL of THF under sonication and subsequently collected by centrifugation. AlO_x/Er/Si-NCs are finally separated from Si-free aluminum oxide as follows: (1) the mixture is re-dissolved in 3 mL of ethylene glycol using sonication, (2) AlO_x/Er/Si-NCs are precipitated using prolonged centrifugation [$\geq$ 12 hr], and (3) ethylene glycol is decanted, and the nanocrystals are then washed with THF>EtOH>THF, as before. Prior to PL measurements, vacuum-dried AlO_x/Er/Si-NCs are annealed at 800°C in a N_2/O_2 atmosphere for 1 hour.

As a control, a NCs-free aluminum oxide matrix was prepared and isolated in a way similar to the synthesis of AlO_x/Er/Si-NCs, with the exception that Er/Si-NCs were absent. These aluminum oxide particles appeared to be significantly smaller (or less agglomerated), and the entire reaction product was lost during isolation: once sonicated into ethylene glycol, none of aluminum oxide precipitate could be collected by centrifugation.

8.1.3 Encapsulation of Er/Si-NCs within Zinc Oxide

During the surface modification with zinc oxide, Er/Si-NCs (0.50±0.05 mg) are combined with 15.0 mg of $ZnCl_2$ (Aldrich) in a 25-mL round-bottom flask. Next, 3.0 mL of acidic H_2O (de-ionized water with a drop of 0.25M HCl) are added, and the flask is placed into a sonicator. Once the $ZnCl_2$ is dissolved and the nanocrystals are uniformly dispersed, 7.0 mL of ethylene glycol are added, and the flask is exposed to sonication for 1 hour. At the end of this sonication period, the flask is placed into an 85±5°C oil bath under N_2 atmosphere and a condenser for 1 hour. The flask is then briefly removed from the oil bath and placed back into the sonicator for 1-2 minutes, during which 5.0 mL of 0.10M NaOH are added. After the flask has been re-inserted into the oil bath, equilibration is allowed to proceed for 20 hours under rapid stirring.

Next, the heating and stirring are discontinued, and the flask is allowed to cool to room temperature. Zinc hydroxide coated nanocrystals and the solvent are then transferred to an Erlenmeyer flask and diluted with 60 mL of H_2O. Upon 1 hour of sonication, solid particles [coated nanocrystals and Si-free $Zn_x(OH)_y$] are isolated using centrifugation. The isolated product is then washed three times with 3 mL of H_2O under sonication and subsequently collected by centrifugation. Similar to the case of AlO_x/Er/Si-NCs, Si-free $Zn_x(OH)_y$ particles are separated as follows: (1) the mixture is re-dissolved in 3 mL of ethylene glycol using sonication, (2) Si-nanoparticles are precipitated using prolonged centrifugation [≥ 12 hr], (3) ethylene glycol is decanted, and the nanocrystals are then washed with THF>EtOH>THF and vacuum dried, as before. The $Zn_x(OH)_y$ surface cap is converted into ZnO_x using an 800°C anneal in a N_2/O_2 atmosphere for 1 hour, thereby producing ZnO_x/Er/Si-NCs which are used in PL measurements.

As a control, a NCs-free zinc oxide matrix was prepared and isolated in a way similar to the synthesis of ZnO_x/Er/Si-NCs, with the exception that Er/Si-NCs were absent. These zinc oxide particles were not sonicated into ethylene glycol, *etc.*, to avoid product loss. As an additional control, a batch of Er/Si-NCs was treated in a way similar to the ZnO_x/Er/Si-NCs with exception of $ZnCl_2$ addition. This was done to assess the potential change in Er/Si-NCs photoluminescence properties as a consequence of base (NaOH) exposure.

8.1.4 Instrumentation

For comparisons of the PL efficiency for nanocrystals with different surface caps, all samples were measured after being dispersed in KBr at the same silicon concentration percent (by mass) with identical acquisition parameters, i.e. laser power, detector sensitivity, etc. Previous X-ray Energy Dispersive Spectroscopy (EDX) measurements indicate erbium level of ≤ 2 at. % within Er/Si-NCs.[148] Erbium concentration within surface-modified nanocrystals is assumed to be in constant proportion to silicon. Macroscopic silicon concentrations for AlO_x/Er/Si-NCs and ZnO_x/Er/Si-NCs were determined via ICP spectroscopy (Desert Analytics, Tucson, Arizona). Microscopic silicon concentrations for ZnO_x/Er/Si-NCs were determined via EDX analysis using a Thermo Noran Vantage EDX system in conjunction with a JEOL JEM-3010 transmission electron microscope (TEM) at the University of Illinois-Chicago. Low-resolution (± 4 nm) near-IR PL spectra were obtained by using an Applied Detector Corp. liquid N_2-cooled Ge detector in conjunction with a Stanford Research Systems Chopper/Lock-In amplifier and an Acton Research Corp. 0.25 m monochromator. Excitation was provided by a Coherent Ar^+ laser. Emitted light was collected at a 40° angle relative to the excitation direction. A 1000 nm cutoff filter (Melles

Griot) was positioned over the monochromator entrance slit to filter out second- and third-order light. An optical microscope and a near IR-transparent optical fiber were used to focus light emitted from the samples onto the monochromator entrance slit.

8.2 Results and Discussion

8.2.1 Photoluminescence of Er^{3+}-doped Si Nanocrystals

An evaluation of the impact of surface modification on the photophysics of Er-doped silicon nanocrystals must begin with an understanding of the fundamental light emission mechanism associated with Er/Si-NCs. The photoluminescence at 1.51 μm is achieved through an energy transfer mechanism which involves a combination of carrier(silicon)-mediated and direct excitation of erbium centers by 488 nm laser light (see Chapter 6). As pointed out earlier, the nanocrystal surface can affect PL intensity in several ways, one of which being interfacial defect density. To remove this latter detriment, surface capping layers are introduced, whose ultimate role is twofold: (1) the dangling bonds are eliminated and the surface strain is relaxed; (2) the clustering of individual nanocrystals is reduced. The latter effect is especially significant since the PL-activating 800°C anneal, which reduces the interior strain and number of lattice defects within Er/Si-NCs, can cause unprotected Si surfaces to fuse together.

A contribution of the former effect to the overall improvement in the PL efficiency of the capped Er/Si-NCs cannot be quantitatively separated from the latter during room-temperature measurements performed on a macroscopic sample. However, the effect of Er/Si-NCs clustering, which occurs during the PL-activating 800°C anneals, and the associated reduction in PL intensity can be mimicked using KBr pellets whose Er/Si-NCs concentration is above 1 wt. %. As shown in Figure 57, the photoluminescence of the uncapped nanocrystals is a function of Er/Si-NCs concentration in KBr. At concentration values above 1 wt. %, the spectra intensities plateau, which indicates that that the KBr

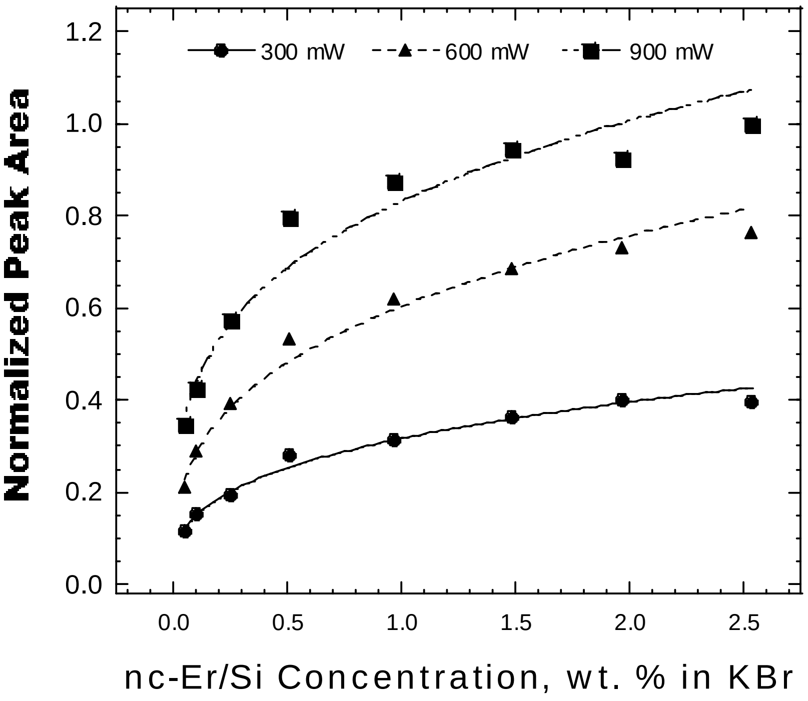

Figure 57. Room-temperature PL of uncapped Er/Si-NCs, dispersed in KBr pellets, under variable laser power excitation (λ_{ex}=488 nm).

samples are optically saturated and the emission of any additional nanocrystals is quenched, primarily via an Auger process. The onset of this saturation is detected at 0.5 wt. % under the low-power laser excitation. An increase in the laser power results in the delay of this onset: a larger population of nanocrystals is being sampled as the higher flux of scattered photons within dense KBr pellets results in the excitation of Er/Si-NCs located throughout the sample.

8.2.2 Photoluminescence of Surface-Modified Er/Si-NCs

Aluminum oxide-coated material (AlO_x/Er/Si-NCs) is synthesized from Er/Si-NCs and $Al(O\text{-}iPr)_3$ via a process similar to a nonhydrolytic sol-gel route followed by calcination.[162-164] ZnO-coated Er/Si-NCs (ZnO_x/Er/Si-NCs) are obtained by: (1) the precipitation of $Zn_x(OH)_y$ from $ZnCl_2$ in the presence of NaOH and Er/Si-NCs; (2) followed by calcination. These terminal 800°C anneals of the surface modified Er/Si-NCs are carried out in a N_2/O_2 atmosphere, unlike the case of the uncapped controls where anneals are performed under vacuum. However, no change in the underlying Er/Si-NCs particle size (TEM) or the local environment of erbium centers occurs during the annealing process, as assessed by EXAFS.[165]

Figure 58 shows the effect that aluminum oxide and zinc oxide surface caps have on the Er/Si-NCs PL in the case of those KBr samples where the nanocrystals' concentration is 0.05 wt. %. Here, AlO_x/Er/Si-NCs and ZnO_x/Er/Si-NCs have the same concentration of

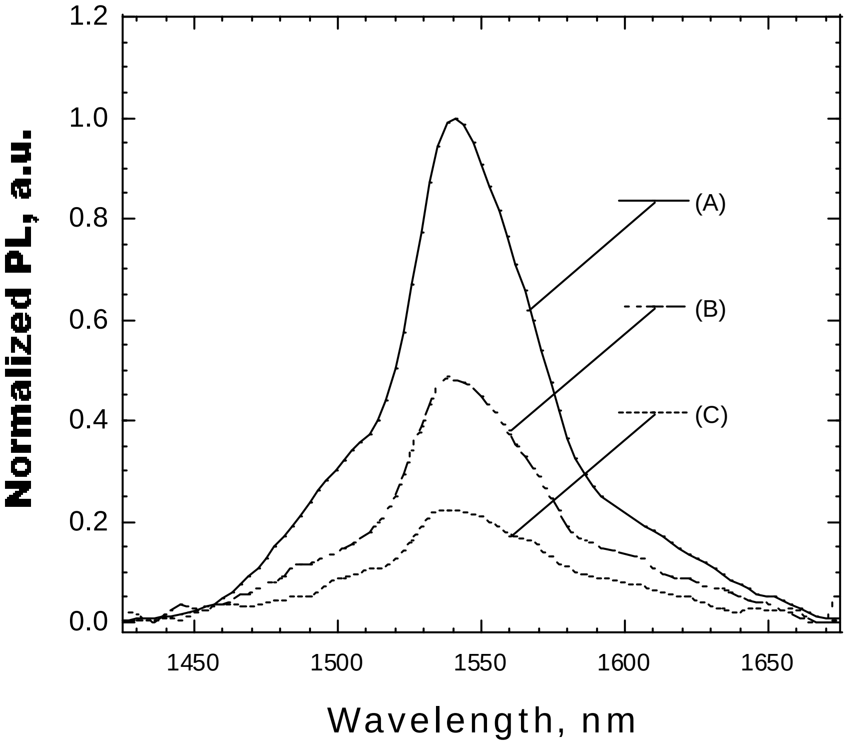

Figure 58. Room-temperature PL of nanocrystal-doped KBr pellets (0.05 wt. % Si; λ_{ex}=488 nm; P_{ex}=300mW): (A) ZnO_x/Er/Si-NCs, (B) AlO_x/Er/Si-NCs, and (C) Er/Si-NCs.

underlying Er/Si-NCs as the uncapped control. The presence of the zinc oxide caps increases the PL efficiency by a factor of four, while aluminum oxide-coated nanocrystals are twice as luminescent as the control. The PL of those Er/Si-NCs which were treated with NaOH in the absence of $ZnCl_2$, *etc*. (see Section 8.1), is similar to the as-prepared Er/Si-NCs. From the spectra presented in Figure 58, one can infer superior photoluminescence of ZnO_x/Er/Si-NCs over the aluminum oxide-capped nanocrystals. The change in photoluminescence properties of the surface-modified Er/Si-NCs can be explained in part by examining the local microstructure of the particles of each type.

Under low-resolution TEM analysis, as-prepared Er/Si-NCs appear as loose agglomerates of discrete particles (see Figure 59A). Each nanocrystal is a single-crystalline Si particle doped with Er^{3+} ions at ~2 at. % loading level.[148] An agglomerate such as the one shown in Figure 59A is expected to fuse into a single large cluster during an 800°C anneal. AlO_x/Er/Si-NCs and ZnO_x/Er/Si-NCs are shown in Figures 59B & 59C, respectively. Table 8 presents the average particle sizes (see the histograms in Figure 60) and compositions of as-

	Particle size (nm)	Composition
Er/Si-NCs	16.6 ± 3.3	≤ 2 at. % Er *(ref. 148)*
AlO_x/Er/Si-NCs	--	8.37 wt. % Si *(ICP)*
ZnO_x/Er/Si-NCs	153.8 ± 40.7	2.01 wt. % Si *(ICP, XEDS)*

Table 8. Average particle sizes and compositions of Er-doped Si nanocrystals.

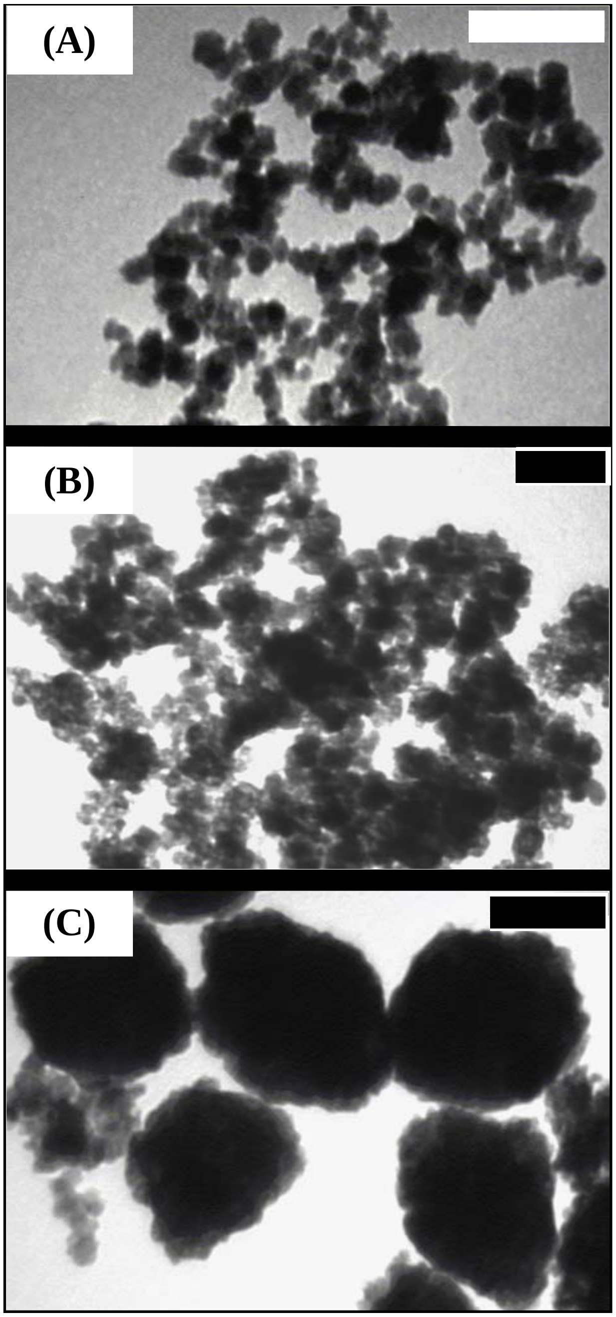

Figure 59. Low-resolution transmission electron micrographs of Si nanocrystals: (A) Er/Si-NCs, (B) as-prepared AlO_x/Er/Si-NCs, and (C) ZnO_x/Er/Si-NCs. Each scale bar is 100 nm.

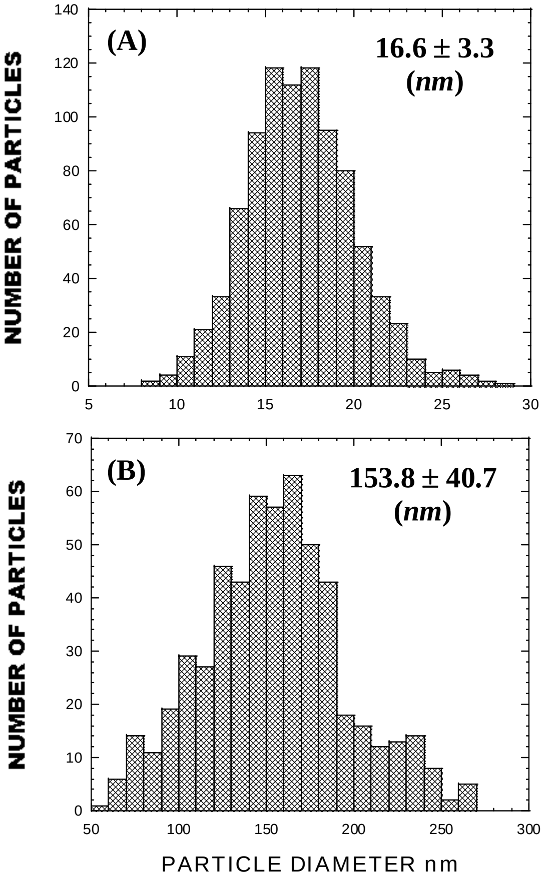

Figure 60. Size histograms for: (A) Er/Si-NCs and (B) ZnO_x/Er/Si-NCs (as shown in Figure 59). Also shown are the statistical average particle diameters and associated standard deviations.

prepared Si nanocrystals. It must be noted that the erbium-to-silicon ratio is assumed to be constant between samples. There is a dramatic change in the overall host geometry/average particle size with the introduction of zinc oxide caps. However, within the aluminum oxide-coated material, individual Er/Si-NCs are clustered randomly, and the average aggregate size cannot be determined. It must be noted that the formation of such discrete zinc oxide particles was not observed during synthesis of the NCs-free ZnO_x control (see Section 8.1), as evidenced by TEM. Such local arrangement of Er/Si-NCs within aluminum or zinc oxide is explained by the corresponding reaction conditions; the reaction scheme of both processes is presented in Figure 61.

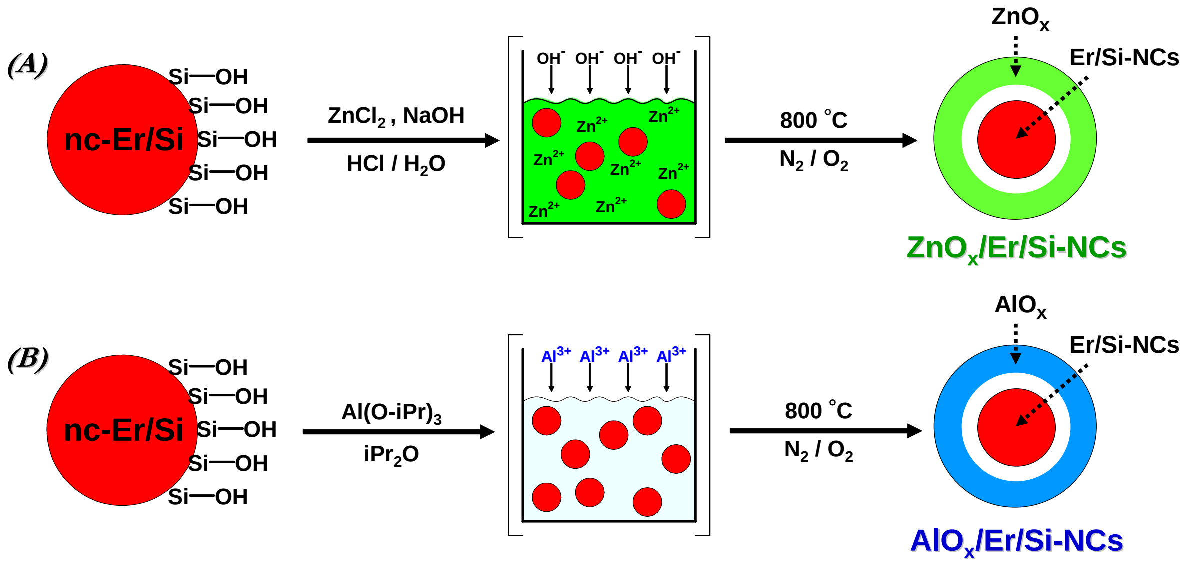

Figure 61. Reaction scheme of capping reagents (inorganic) with Si nanoparticles: (A) ZnO_x/Er/Si-NCs and (B) AlO_x/Er/Si-NCs.

Surface modification with aluminum oxide takes place under kinetic control. Rapid and spontaneous precipitation of aluminum oxide from solution, which is further accelerated by the presence of residual water, results in random entrapment of silicon particles within the aluminum oxide matrix. On the other hand, precipitation of zinc hydroxide is thermodynamically controlled and is initiated by the addition of base. During the initial precipitation, encapsulation of nanocrystals within $Zn_x(OH)_y$ is driven by the Oswald ripening process[166] and results in discrete zinc hydroxide particles doped with Er/Si-NCs.[161] Deposition of a zinc oxide surface layer is a thermodynamically-controlled reaction, during which zinc hydroxide nucleation occurs homogeneously in solution but also on the surface of nanocrystals; the subsequent growth of silicon-free zinc hydroxide particles is suppressed by Oswald ripening. Within each of these large ZnO_x/Er/Si-NCs particles, Er/Si-NCs are well dispersed. The EDX map in Figure 62B shows uniform distribution of silicon within the

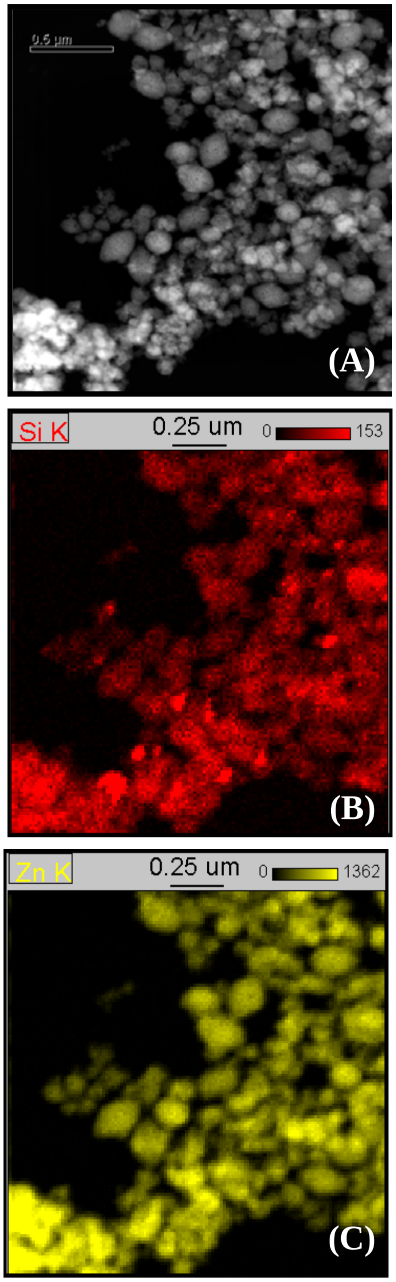

Figure 62. A low-resolution TEM micrograph of ZnO_x/Er/Si-NCs (A) and the associated EDX maps: (B) silicon and (C) zinc.

zinc oxide matrix; Figure 62C is the EDX map which shows locations of zinc, present in excess according to the different intensities of Si and Zn signals. Due to the poor segregation of Er/Si-NCs within aluminum oxide matrix, AlO_x/Er/Si-NCs are relatively less efficient emitters than ZnO_x/Er/Si-NCs.

The PL mechanism associated with Er/Si-NCs was studied through evaluation of emission intensity dependence on the excitation wavelength. When Er/Si-NCs absorb laser light (λ_{ex}=488 nm) and then transfer this energy to Er^{3+} ions, the photoexcitation of Er^{3+} centers is a carrier[silicon]-mediated process.[148,155,156] In this case, a plot of PL intensity *vs.* excitation wavelength is a straight line, sloping downward from 476 to 514 nm mark [see Figure 63(RD)].[148,155,156] On the other hand, Er^{3+} centers can also be laser-excited directly if

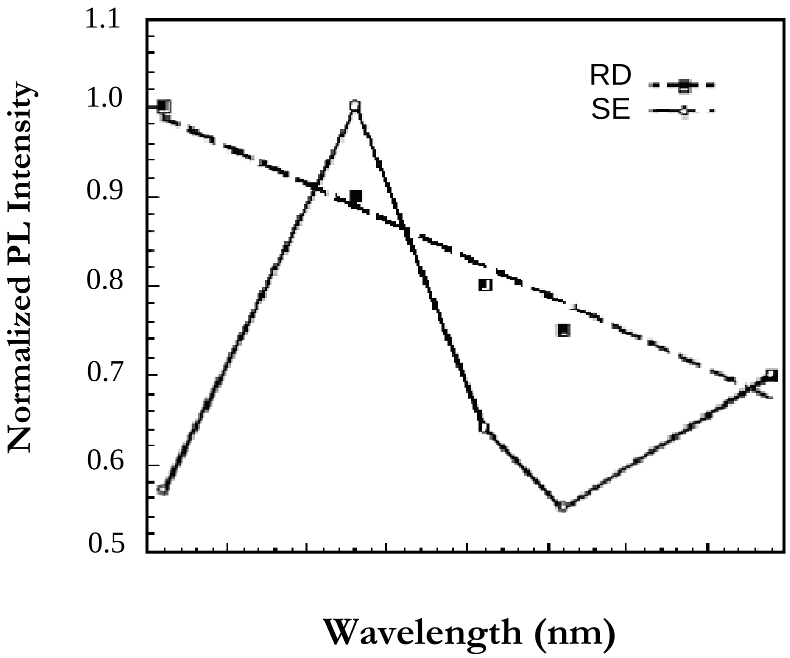

Figure 63. Near-IR PL spectra of Er^{3+} surface-enriched Si nanocrystals (SE) and randomly dispersed Er/Si-NCs (RD) in a KBr for the various excitation wavelengths. Taken from reference 155.

the excitation wavelength is 488 or 514 nm, in which case resulting PL intensity *vs.* wavelength plot is non-linear, with spikes at these wavelengths [see Figure 63(SE)].[155] Such PL intensity *vs.* excitation wavelength plots associated with surface-modified Er/Si-NCs are presented in Figure 64. Photoluminescence of uncapped nanocrystals is a carrier-mediated process, as evidenced by the sloping straight line in Figure 64(C). The plots associated with surface-modified nanocrystals (Figures 64 A&B) yield enhanced emission at 488 and 514 nm excitation, indicating a direct excitation component, more pronounced in the case of ZnO_x/Er/Si-NCs. Nonetheless, the excitation mechanism in both cases is perhaps a combination of direct and carrier-mediated processes. This is plausible, for example, in the case of AlO_x/Er/Si-NCs since the overall emission intensity at the highest excitation wavelength (514 nm) is still lower relative to the lowest wavelength value (476).

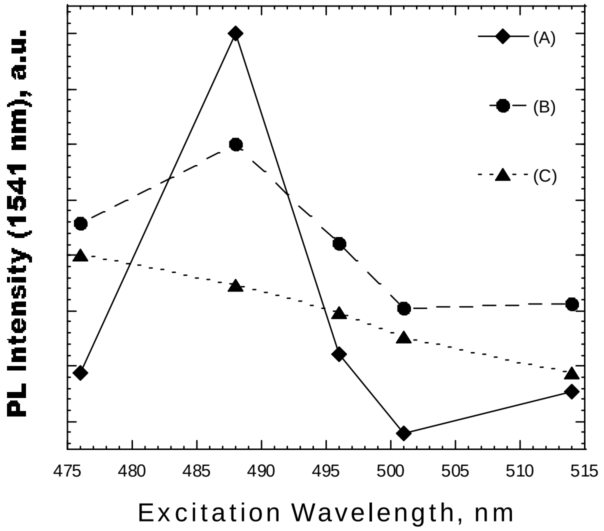

Figure 64. Near-IR PL spectra of Er^{3+}-doped Si nanocrystals in a KBr for the various excitation wavelengths: (A) ZnO_x/Er/Si-NCs, (B) AlO_x/Er/Si-NCs, and (C) Er/Si-NCs (ZnO_x/Er/Si-NCs-like treated control). Each spectrum was normalized and shifted vertically for clarity.

In addition, encapsulation of erbium-doped silicon nanocrystals with zinc oxide not only improves the luminescence efficiency, but also has a potential for the development of a multi-color emitter, since ZnO is a direct wide-band gap semiconductor which is capable of emitting UV-Visible light.[161] Figure 65 is the visible photoluminescence spectrum of ZnO_x/Er/Si-NCs; the spectrum was obtained using a fluorescence microscope with an excitation of 370 nm (see Chapter 3.1 for instrument specifications). ZnO_x/Er/Si-NCs also exhibit green thermoluminescence when annealed to 800°C (see Section 8.1).

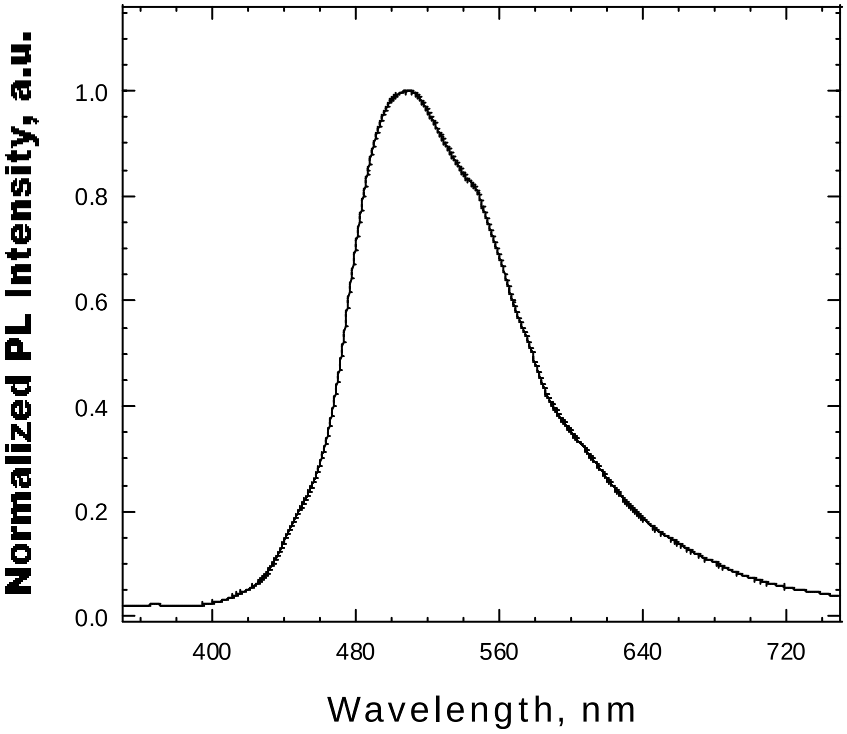

Figure 65. Visible PL (green) spectrum obtained from ZnO_x/Er/Si-NCs.

8.3 Summary

Through selective surface modification of Er/Si-NCs with inorganic capping layers comprised of either aluminum oxide or zinc oxide the photoluminescence efficiency can be improved. Encapsulated nanocrystals of both types of surface caps show an improvement in erbium photoluminescence when compared to the uncapped control. The presence of the ZnO_x caps increases the PL efficiency by a factor of four, while AlO_x-coated nanocrystals are twice as luminescent as the control. Discrete ZnO_x/Er/Si-NCs structures exhibit photoluminescence superior to AlO_x/Er/Si-NCs due to a more efficient separation of erbium centers and, therefore, suppressed contribution of non-radiative Auger erbium relaxation pathway to the PL process.

CHAPTER IX.

Concluding Remarks

Fabrication of luminescent and bioactive silicon structures is the general theme of this dissertation. The first part of the work focused on biomaterial properties of surface-modified silicon wafers. The use of Si as an electronically-responsive platform for the development of smart biomedical devices using existing microelectronics technology was the main interest of this research, during which the bio-relevance of the previously unexplored phase $CaSi_2$ was discovered. Thereafter, the scope of the work expanded to an evaluation of bioactive properties of calcium disilicide itself and as a composite while researching its potential biomedical applications. Concurrently, inorganic surface modification of erbium-doped silicon nanocrystals was studied as a way to improve Si luminescence efficiency and develop a silicon-based light source for future optoelectronic applications.

Chapter 3 presents two methods for fabricating interfacial layers on silicon using a facile dry-etch spark ablation technique. An electric discharge was used to selectively oxidize areas on single-crystal Si to form porous silica films (SiO_2/Si). These subsequently act as active growth layers for bias-assisted deposition of apatitic phosphates (CaP; synthetic bone) *in vitro*. The selectivity of bioactive pattern formation was further improved through fabrication of calcium disilicide ($CaSi_2$) growth layers on spark-processed Si. $CaSi_2$ was chosen as an alternative interfacial layer on Si in an attempt to increase local concentration of calcium and thus accelerate the onset of calcium phosphate nucleation. Calcium disilicide is a semimetal because the overlap between *p* and *d* orbitals of Si and Ca, respectively, reduces the energy gap between conduction and valance bands of the bulk crystalline $CaSi_2$. Under electric bias, a bioactive CaP film selectively forms on the more conductive $CaSi_2$ growth layers.

While $CaSi_2$/Si wafer electrodes exhibit superior site-selectivity towards CaP electrodeposition, spark-processed silica is an appealing alternative since it can be used to form elaborate patterns of CaP films on Si. In addition to this, contrasting biomineralization behaviors of insulating SiO_2 and metallic $CaSi_2$ local domains on semiconducting Si allowed the elucidation of mechanistic details of the bias-assisted CaP film growth *in vitro*. In particular, under accelerated growth conditions imposed by the presence of an electric current, magnesium-rich calcium carbonates form alongside apatitic phosphates.

The potential biomaterial applications of calcium disilicide growth layers on spark-processed Si were also demonstrated through successful surface modification of calcified $CaSi_2$/Si wafer electrodes with medicinally relevant compounds: alendronate and norfloxacin. The former can also be used as a linker between calcified bioactive silicon and molecules that react with primary amine groups, which are exposed when alendronate is bound to the electrochemically-deposited CaP film on $CaSi_2$ growth layers. This strategy opens numerous pathways for the design of new biosensors and drug-delivery systems. In one specific proof-of-concept demonstration, norfloxacin was used to show sustained antibiotic drug release from calcified $CaSi_2$/Si.

Chapter 4 demonstrates that $CaSi_2$/Si composite electrodes can readily calcify *in vitro* even in the absence of the electric potential. The process of $CaSi_2$/Si calcification under zero bias appears to follow the same mechanism as bioactive glasses/ceramics, during which calcium phosphate growth is significantly dependent on the structural degradation of $CaSi_2$ grains. Surface functional groups, initially present on the as-prepared material, cannot induce CaP nucleation which begins only upon delamination of $CaSi_2$ layers. This work demonstrates that control over biomineralization rate and mechanism can be eventually achieved by tuning the reaction temperature and/or applying electric current instead of tailoring the starting chemical composition and structure of a biomaterial, which is typically done in case of other biomaterials that $CaSi_2$ mimics: bioglasses and porous silicon.

Another demonstration of biomaterial properties of calcium disilicide is presented in Chapter 5. Biodegradable and bioactive scaffolds for bone tissue regeneration can be obtained through the incorporation of $CaSi_2$ grains within polycaprolactone (PCL) frameworks. Matrix porosity values over 95% can be achieved by employing a combination of salt-leaching and microemulsion techniques for polymer scaffold processing. Calcium disilicide powder can either be added to a mixed-composition porogen during a given scaffold's fabrication to produce homogeneously-dispersed PCL-embedded grains (*EMB*-), or it can be added to pre-made scaffolds which will then result in the random dispersion of free-standing grains within PCL (*RD*-). Scaffolds of the first type may find further applications in the field of bioelectronics due to the unique semimetallic properties of $CaSi_2$. The second method for seeding porous PCL networks with bioactive $CaSi_2$ may be useful when low loading levels and controlled positioning of a bioactive material within a scaffold is needed. The process of $CaSi_2$/PCL scaffold calcification under zero bias, during which calcium phosphate growth is significantly dependent on the structural degradation of $CaSi_2$ grains, has a similar mechanism as the CaP growth on bioactive glasses/ceramics. The biomineralization of these scaffolds is initiated solely by the inorganic phase and can be accelerated by the degradation of the polymer matrix. As a consequence, RD-$CaSi_2$/PCL facilitates deposition of CaP at a slightly faster rate than the scaffolds of the *EMB*- type. Successful fluorescent tagging of CaP within calcified PCL scaffolds using fluorescein isothiocyanate through bisphosphonate amine (alendronate) linkages implies that these materials may potentially be used in drug delivery applications.

The dissertation concludes with Chapter 8, where it is demonstrated that the photoluminescence efficiency of Er^{3+}-doped silicon nanocrystals (Er/Si-NCs) can be improved through selective surface modification with inorganic capping layers comprised of either aluminum oxide or zinc oxide. Encapsulated nanocrystals of both types of surface caps show an improvement in erbium photoluminescence when compared to the uncapped control. The presence of the ZnO_x caps increases the PL efficiency by a factor of four, while AlO_x-coated nanocrystals are twice as luminescent as the control. Discrete ZnO_x/Er/Si-NCs structures exhibit photoluminescence superior to AlO_x/Er/Si-NCs due to a more efficient separation of erbium centers. In addition, encapsulation of erbium-doped silicon nanocrystals with zinc oxide not only improves the luminescence efficiency, but also has a potential for the development of a multi-color emitter, since ZnO is a direct wide-band gap semiconductor which is capable of emitting UV-Visible light.

REFERENCES

1. Ratner, B.D.; Bryant, S.J. *Annu. Rev. Biomed. Eng.* **2004,** *6*, 41.
2. Langer, R.; Tirrell, D.A. *Nature* **2004,** *428*, 487.
3. Hench, L.L.; Xynos, I.D.; Polak, J.M. *J. Biomater. Sci. Polymer Edn.* **2004,** *15*, 543.
4. Hench, L.L.; Polak, J.M. *Science* **2002,** *295,* 1014.
5. Bronzino, J. D. *The Biomedical Engineering Handbook*, **2000**, CRC Press, Boca Raton.
6. Anderson, D.G.; Burdick, J.A.; Langer, R. *Science* **2004,** *305*, 1923.
7. Buckwalter, J.A. *J. Bone Joint Surg. Am.* **2000,** *82*, 1782.
8. Jackson, T.N. *Nat. Mater.* **2005,** *4*, 581.
9. Hill, R.T.; Lyon, J.L.; Allen, R.; Stevenson, K.J.; Shear, J.B. *J. Am. Chem. Soc.* **2005,** *127*, 10707.
10. Chew, S.Y.; Wen, J.; Yim, E.K.F.; Leong, K.W. *Biomacromolecules* **2005,** *6*, 2017.
11. Whitehead, M.A. *Biodegradable Polymer Scaffolds Containing Mesoporous Silicon and One-Dimensional Nanostructures of Silicon and Germanium for Use in Tissue Engineering,* M.S. Thesis, Texas Christian University, **2005.**
12. Zelikin, A.N.; Lynn, D.M.; Farhadi, J.; Martin, I.; Shastri, V.; Langer, R. *Angew. Chem. Int. Ed.* **2002,** *41*, 141.
13. Chiellini, E.; Solaro, R. *Adv. Mater.* **1996,** *8*, 305.
14. Ball, P. *Nat. Mater.* **2005,** *4,* 119.
15. Ieong, M.; Doris, B.; Kedzierski, J.; Rim, K.; Yang, M. *Science* **2004,** *306,* 2057.
16. Buckwalter, J.A. *J. Bone Joint Surg. Am.* **2003,** *85*, 1.
17. Weiner, S.; Wagner, H.D. *Annu. Rev. Mater. Sci.* **1998,** *28,* 271.
18. Rodan, G.A.; Martin, T.J. *Science* **2000,** *289,* 1508.
19. Veis, A. *Science* **2005,** *307*, 1419.
20. Boskey, A.L. *Connect. Tissue Res.* **2003,** *44*, 5.
21. Popescu, M.L.; Piticescu, R.M.; Petrescu, S.; Zdrentu, L.; Mihailescu, I.; Socol, G.; Lojkowski, W. *Rev. Adv. Mater. Sci.* **2004,** *8*, 164.

22. LeGeros, R. Z. *Calcium Phosphates in Oral Biology and Medicine,* **1991**, Karger, Basel.

23. Shirtliff, V.J.; Hench, L.L. *J. Mater. Sci.* **2003,** *38*, 4697.

24. Hench, L. L.; Wilson, J. *An Introduction to Bioceramics*, **1993**, World Scientific, River Edge.

25. Canham, L.T. *Adv. Mater.* **1995,** *7*, 1033.

26. Canham, L.T.; Newey, J.P.; Reeves, C.L.; Houlton, M.R.; Loni, A.; Simons, A.J.; Cox, T.I. *Adv. Mater.* **1996,** *8*, 847.

27. Ji, J.; Li, X.; Canham, L.T.; Coffer, J.L. *Adv. Mater.* **2002,** *14*, 41.

28. Li, X.; Coffer, J.L.; Chen, Y.; Pinizzotto, R.F.; Newey, J.; Canham, L.T. *J. Am. Chem. Soc.* **1998,** *120*, 11706.

29. Li, X.; St. John, J.; Coffer, J.L.; Chen, Y.; Pinizzotto, R.F.; Newey, J.; Reeves, C.; Canham, L.T. *Biomed. Microdevices* **2000,** *2*, 265.

30. Santini Jr, J.T.; Cima, M.J.; Langer, R. *Nature* **1999,** *97*, 335.

31. Lahann, J.; Mitragotri, S.; Tran, T.; Kaido, H.; Sundaram, J.; Choi, I.S.; Hoffer, S.; Somorjai, G.A.; Langer, R. *Science* **2003,** *299*, 371.

32. Maex, K.; van Rossum, M. *Properties of Metal Silicides*, **1995**, INSPEC, Stevenage.

33. Bisi, O.; Braicovich, L.; Carbone, C.; Lindau, I.; Iandelli, A.; Olcese, G.L.; Palenzona, A. *Phys. Rev. B* **1989,** *40*, 10194.

34. Schopke, A.; Wurz, R.; Schmidt, M. *Surf. Interface Anal.* **2002,** *34*, 464.

35. Morar, J.F.; Wittmer, M. *Phys. Rev. B.* **1988,** *37*, 2618.

36. Vogg, G.; Brandt, M.S.; Stutzmann, M. *Chem. Mater.* **2003,** *15*, 910.

37. Affronte, M.; Sanfilippo, S.; Nunez-Regueiro, M.; Laborde, O.; Lefloch, S.; Bordet, P.; Hanfland, M.; Levi, D.; Palenzona, A.; Olcese, G.L. *Physica B* **2000,** *284*, 1117.

38. Sanfilippo, S.; Elsinger, H.; Nunez-Regueiro, M.; Laborde, O.; LeFloch, S.; Affronte, M.; Olcese, G.L.; Palenzona, A. *Phys. Rev. B* **2000,** *61*, R3800.

39. Aoki, M.; Ohba, N.; Noritake, T.; Towata, S. *Appl. Phys. Lett.* **2004,** *85*, 387.

40. Fahy, S.; Hamann, D.R. *Phys. Rev. B* **1990,** *41*, 7587.

41. Satta, G.; Profeta, G.; Bernardini, F.; Continenza, A.; Massidda, S. *Phys. Rev. B* **2001,** *64*, 104507.

42. Gemming, S.; Seifert, G. *Phys. Rev. B* **2003,** *68*, 075416.

43. Jia, J.J.; Callcott, T.A.; Asfaw, A.; Carlisle, J.A.; Terminello, L.J.; Ederer, D.L.; Himpsel, F.J.; Perera, R.C.C. *Phys. Rev. B* **1995,** *52*, 4904.

44. Langer, R. *Acc. Chem. Res.* **2000,** *33*, 94.

45. Pereira, M.M.; Jones, J.R.; Hench, L.L. *Adv. Appl. Ceram.* **2005,** *104*, 35.

46. Kokubo, T.; Kim, H.M.; Kawashita, M. *Biomaterials* **2003,** *24*, 2161.

47. Kokubo, T. *Mat. Sci. Eng. C-Biomim.* **2005,** *25*, 97.

48. Murphy, W.L.; Mooney, D.J. *J. Am. Chem. Soc.* **2002,** *124*, 1910.

49. Oyane, A.; Uchida, M.; Yokoyama, Y.; Choong, C.; Triffitt, J.; Ito, A. *J. Biomed. Mater. Res.* **2005,** *75A*, 138.

50. Kutz, M. *Standard Handbook of Biomedical Engineering and Design*, **2003**, McGraw-Hill, New York.

51. Kohn, M.J.; Rakovan, J.F.; Hughes, J. M. *Phosphates: Geochemical, Geobiological, and Materials Importance*, **2002**, Mineralogical Society of America, Washington.

52. Oyane, A.; Onuma, K.; Ito, A.; Kim, H.M.; Kokubo, T.; Nakamura, T. *J. Biomed. Mater. Res. A* **2003,** *64*, 339.

53. Weiner, S.; Sagi, I.; Addadi, L. *Science* **2005,** *309*, 1027.

54. Dee, K.C.; Puleo, D.A.; Bizios, R. *An Introduction to Tissue-Biomaterial Interactions*, **2002**, Wiley-Liss, Hoboken.

55. Neo, M.; Nakamura, T.; Ohtsuki, C.; Kokubo, T.; Yamamuro, T. *J. Biomed. Mater. Res.* **1993,** *27*, 999.

56. Hench, L.L.; West, J.K. *Chem. Rev.* **1990,** *90*, 33.

57. Jones, J.R.; Ahir, S.; Hench, L.L. *J. Sol-Gel Sci. Techn.* **2004,** *29*, 179.

58. Fujibayashi, S.; Neo, M.; Kim, H.M.; Kokubo, T.; Nakamura, T. *Biomaterials* **2003,** *24*, 1349.

59. Fini, M.; Giavaresi, G.; Giardino, R.; Cavani, F.; Cadossi, R. *J. Bone Joint Surg. Br.* **2006,** *88*, 123.

60. Wopenka, B.; Pasteris, J.D. *Mat. Sci. Eng. C-Biomim.* **2005,** *25*, 131.

61. Zimolo, Z.; Wesolowski, G.; Rodan, G.A. *J. Clin. Invest.* **1995,** *96*, 2277.

62. Mundy, G.R. *Bone* **1991,** *12*, S1.

63. Kanehisa, J.; Heersche, J.N.M. *Bone* **1988,** *9*, 73.

64. Ross Garrett, I. *Semin. Oncol.* **1993,** *20*, 4.

65. Orr, W.; Varani, J.; Gondek, M.D.; Ward, P.A.; Mundy, G.R. *Science* **1979,** *203*, 176.

66. Eilon, G.; Mundy, G.R. *Science* **1978,** *276*, 726.

67. Sabatini, M.; Yates, A.J.; Ross Garrett, I.; Chavez, J.; Dunn, J.F.; Bonewald, L.; Mundy, G.R. *Lab. Invest.* **1990,** *63*, 676.

68. Canham, L.T.; Cox, T.I.; Loni, A.; Simons, A.J. *Appl. Surf. Sci.* **1996,** *102*, 436.

69. Li, P.; Ohtsuki, C.; Kokubo, T.; Nakanishi, K.; Soga, N.; Nakamura, T.; Yamamuro, T. *J Mater. Sci.-Mater. M* **1993,** *4*, 127.

70. Canham, L.T. *Properties of Porous Silicon*, **1997**, Inspec/Iee, London.

71. Canham, L.T.; Reeves, C.L. *Mat. Res. Soc. Symp. Proc.* **1996,** *414*, 189.

72. Anderson, S.; Elliot, H.; Wallis, D.; Canham, L.; Powell, J. *Phys. Stat. Sol. (A)* **2003,** *197*, 331.

73. Canham, L.T.; Reeves, C.L.; King, D.O.; Branfield, P.J.; Crabb, J.G.; Ward, M.C.L. *Adv Mater.* **1996,** *8*, 850.

74. Yamashita, K.; Oikawa, N.; Umegaki, T. *J. Ceram. Soc. Japan.* **1996,** *8*, 2697.

75. Yamashita, K.; Nakamura, S. *J. Ceram. Soc. Japan* **2005,** *113*, 1.

76. Lehmann, V.; Gosele, U. *Appl. Phys. Lett.* **1991,** *8*, 856.

77. Li, X. *Fundamental Properties of Transition Metal Complex Doped-Calcium Phosphate/Porous Silicon/Silicon Structures*, Ph.D. Dissertation, Texas Christian University, **2000.**

78. Ludwig, M.H.; Augustin, A.; Hummel, R.E.; Gross, T. *J. Appl. Phys.* **1996,** *80*, 5318.

79. Hummel, R.E.; Chang, S. *Appl. Phys. Lett.* **1992,** *61*, 1965.

80. St. John, J.; Coffer, J.L. *Appl. Phys. Lett.* **1996,** *68*, 3416.

81. St. John, J.; Coffer, J.L.; Rho, Y.G.; Diehl, P.; Pinizzotto, R.F.; Culp, T.D.; Bray, K.L. *Chem. Mater.* **1997,** *9*, 3176.

82. Coffer, J.L.; Montchamp, J.L.; Aimone, J.B.; Weis, R.P. *Phys. Status Solidi A* **2003,** *197*, 336.

83. Jeal, W.; Barradell, L.B.; McTavish, D. *Drugs* **1997,** *53*, 415.

84. Zhanel, G.G.; Ennis, K.; Vercaigne, L.; Walkty, A.; Gin, A.S.; Embil, J.; Smith, H.; Hoban, D.J. *Drugs* **2002,** *62*, 13.

85. Weis, R.P.; Montchamp, J.L.; Coffer, J.L.; Attiah, D.G.; Desai, T.A. *Dis. Markers* **2002,** *18*, 159.

86. Melde, B.J.; Stein, A. *Chem. Mater.* **2002,** *14*, 3326.

87. Chen, Z.; Xiong, R.; Zuo, J.; Guo, Z.; You, X.; Fun, H. *Dalton T.* **2000,** *22*, 4013.

88. Uchida, M.; Kim, H.; Kokubo, T.; Miyaji, F.; Nakamura, T. *J. Am. Ceram. Soc.* **2001,** *84*, 2041.

89. Kieczykowski, G.R.; Jobson, R.B.; Melillo, D.G.; Reinhold, D.F.; Grenda, V.J.; Shinkai, I. *J. Org. Chem.* **1995,** *60*, 8310.

90. Perez-Pariente, J.; Balas, F.; Roman, J.; Salinas, A.J.; Vallet-Regi, M. *J. Biomed. Mater. Res.* **1999,** *47*, 170.

91. Walsh, D.; Mann, S. *Adv. Mater.* **1997,** *9*, 658.

92. Trau, M.; Saville, D.A.; Aksay, I.A. *Science* **1996,** *272*, 706.

93. Trau, M.; Saville, D.A.; Aksay, I.A. *Langmuir* **1997,** *13*, 6375.

94. Wang, R.; Hu, Y.X. *J. Biomed. Mater. Res.* **2003,** *67*, 270.

95. Somasundaran, P.; Amankonah, J.O.; Ananthapadmabhan, K.P. *Colloids Surf.* **1985,** *15*, 309.

96. Park, J.H.; Lee, Y.K.; Kim, K.M.; Kim, K.N. *Surf. Coat. Tech.* **2005,** *195*, 252.

97. Xie, J.; Riley, C.; Kumar, M.; Chittur, K. *Biomaterials* **2002,** *23*, 3609.

98. Kumar, M.; Dasarathy, H.; Riley, C. *J. Biomed. Mater. Res.* **1999,** *45*, 302.

99. Raz, S.; Weiner, S.; Addadi, L. *Adv. Mater.* **2000,** *12*, 38.

100. Loste, E.; Wilson, R.M.; Seshadri, R.; Meldrum, F.C. *J. Cryst. Growth* **2003,** *254*, 206.

101. Oyane, A.; Kim, H.; Furuya, T.; Kokubo, T.; Miyazaki, T.; Nakamura, T. *J. Biomed. Mater. Res.* **2003,** *65*, 188.

102. Lin, K.S.K.; Tseng, Y.; Mou, Y.; Hsu, Y.; Yang, C.; Chan, J.C.C. *Chem. Mater.* **2005,** *17*, 4493.

103. Martinez, A.; Izquierdo-Barba, I.; Vallet-Regi, M. *Chem. Mater.* **2000,** *12*, 3080.

104. Arcos, D.; Pena, J.; Vallet-Regi, M. *Key Eng. Mat.* **2004,** *254*, 27.

105. Kontrec, J.; Kralj, D.; Brecevic, L.; Falini, G.; Fermani, S.; Noethig-Laslo, V.; Mirosavljevic, K. *Eur. J. Inorg. Chem.* **2004,** 4579.

106. Lakshminarayanan, R.; Valiyaveettil, S. *Cryst. Growth Des.* **2003,** *3*, 611.

107. Blumenthal, N.C.; Betts, F.; Posner, A.S. *Calcif. Tissue Res.* **1977,** *23*, 245.

108. Blumenthal, N.C.; Posner, A.S. *Colloids Surf.* **1987,** *26*, 123.

109. Sawada, K. *Pure Appl. Chem.* **1997,** *69*, 921.

110. Bone, H.; Hosking, D.; Devogelaer, J.P.; Tucci, J.R.; Emkey, R.D.; Tonino, R.T.; Rodriguez-Portales, J.A.; Downs, R.W.; Gupta, J.; Santora, A.C.; Liberman, U.A. *N. Eng. J. Med.* **2004,** *350*, 1189.

111. Jackson, K. *Internet J. Vib. Spec.[www.ijvs.com]* **1998,** *2*, 1.

112. de Aza, P.N.; Guitian, F.; Santos, C.; de Aza, S.; Cusco, R.; Artus, L. *Chem. Mater.* **1997,** *9*, 916.

113. Otto, C.; de Grauw, J.; Duindam, J.J.; Sijtsema, N.M.; Greve, J. *J. Raman Spectrosc.* **1997,** *28*, 143.

114. Pezzotti, G.; Sakakura, S. *J. Biomed. Mater. Res.* **2003,** *65A*, 229.

115. Schulze, K.A.; Balooch, G.; Marshall, G.W.; Marshall, S.J. *J. Biomed. Mater. Res.* **2004,** *69A*, 286.

116. Gabrielli, C.; Jaouhari, R.; Joiret, S.; Maurin, G. *J. Raman Spectrosc.* **2000,** *31*, 497.

117. de Aza, P.N.; Santos, C.; Pazo, A.; de Aza, S.; Cusco, R.; Artus, L. *Chem. Mater.* **1997,** *9*, 912.

118. Notingher, I.; Jones, J.R.; Verrier, S.; Bisson, I.; Embanga, P.; Edwards, P.; Polak, J.M.; Hench, L.L. *Spectroscopy* **2003,** *17*, 275.

119. Brown, P.W.; Fulmer, M. *J. Biomed. Mater. Res.* **1996,** *31*, 395.

120. Yamagishi, K.; Onuma, K.; Suzuki, T.; Okada, F.; Tagami, J.; Otsuki, M.; Senawangse, P. *Nature* **2005,** *433*, 819.

121. Kim, H.M.; Himeno, T.; Kawashita, M.; Kokubo, T.; Nakamura, T. *J. Roy. Soc. Interface* **2004,** *1*, 17.

122. Thomson, R.C.; Shung, A.K.; Yaszemski, M.J.; Mikos, A.G. *Principles of Ttissue Engineering: Polymer Scaffold Processing*, **2002**, Academic Press, San Diego.

123. Josse, S.; Faucheux, C.; Soueidan, A.; Grimandi, G.; Massiot, D.; Alonso, B.; Janvier, P.; Laib, S.; Gauthier, O.; Daculsi, G.; Guicheux, J.; Bujoli, B.; Bouler, J. *Adv. Mater.* **2004,** *16*, 1423.

124. Josse, S.; Faucheux, C.; Soueidan, A.; Grimandi, G.; Massiot, D.; Alonso, B.; Janvier, P.; Laib, S.; Pilet, P.; Gauthier, O. *Biomaterials* **2005,** *26*, 2073.

125. Uludag, H.; Kousinioris, N.; Gao, T.; Kantoci, D. *Biotechnol. Prog.* **2000,** *16*, 258.

126. Smith, A.L. *The Analytical Chemistry of Silicones*, **1991**, John Wiley & Sons, Inc., New York.

127. Jugdaohsingh, R.; Anderson, S.; Tucker, K.; Elliott, H.; Kiel, D.; Thompson, R.; Powell, J. *Am. J. Clin. Nutr.* **2002,** *75*, 887.

128. Carlisle, E.M. *Science.* **1970,** *167*, 179.

129. Riordan, M.; Hoddeson, L. *Crystal Fire*, **1997**, Norton, New York.

130. McGuire, G.E. *Semiconductor Materials and Process Technology Handbook*, **1988**, Noyes Publications, Park Ridge.

131. Moore, G. *Electronics* **1965,** *38*, April 19.

132. Robinson, A.L. *Science* **1980,** *208*, 480.

133. Keye, R.W. *Science* **1977,** *195*, 1230.

134. Campbell, S.A.; Lewerenz, H.J. *Semiconductor Micromachining*, **1998**, Wiley, Chichester.

135. Xia, Y.; Rogers, J.A.; Paul, K.E.; Whitesides, G.M. *Chem. Rev.* **1999,** *99*, 1823-1848.

136. Reed, G.T. *Nature* **2004,** *427*, 595.

137. Linnros, J. *Nat. Mater.* **2005,** *4*, 117.

138. Liu, W. *Fundamentals of III-V Devices: HBTs, MESFETs, and HFETs/HEMTs*, **1999**, Wiley, New York.

139. Gatos, H.C. *Science* **1969,** *164*, 137.

140. Liu, A.; Jones, R.; Liao, L.; Samara-Rubio, D.; Ruin, D.; Cohen, O.; Nicolaescu, R.; Paniccia, M. *Nature* **2004,** *427*, 615.

141. Xu, Q.; Schmidt, B.; Pradhan, S.; Lipson, M. *Nature* **2005,** *435*, 325.

142. Faist, J. *Nature* **2005,** *433*, 691.

143. Pankove, J.I. *Optical Processes in Semiconductors,* **1971**, Prentice-Hall, Englewood Cliffs.

144. Kimerling, L.C.; Kolenbrander, K.D.; Palm, J. *J. Solid State Phys.* **1997,** *50*, 333.

145. Canham, L.T. *Appl. Phys. Lett.* **1990,** *57*, 1046.

146. Ng, W.L.; Lourenco, M.A.; Gwilliam, R.M.; Ledain, S.; Shao, G.; Homewood, K.P. *Nature* **2001,** *410*, 192.

147. Wu, J.; Punchaipetch, P.; Wallace, R.M.; Coffer, J.L. *Adv. Mater.* **2004,** *16*, 1444.

148. St. John, J.; Coffer, J.L.; Chen, Y.; Pinizzotto, R.F. *J. Am. Chem. Soc.* **1999,** *121*, 1888.

149. Cotton, S. *Lanthanides and Actinides,* **1991**, Oxford University Press, New York.

150. van Pieterson, L.; Wegh, R.T.; Meijerink, A. *J. Phys. Chem.* **2001,** *115*, 9382.

151. Polman, A. *J. Appl. Phys.* **1997,** *82*, 1.

152. Ballato, J.; Lewis, J.S.; Holloway, P. *MRS Bull.* **1999,** 51.

153. St. John, J.; Coffer, J.L.; Chen, Y.; Pinizzotto, R.F. *Appl. Phys. Lett.* **2000,** *77*, 1635.

154. Ennen, H.; Scheider, J.; Pomrenke, G.; Axman, A. *Appl. Phys. Lett.* **1983,** *43*, 943.

155. Senter, R.A. *A Study of Structural and Electronic Effects in Erbium (III) Doped and Undoped Group 14 Nanostructures,* Ph.D. Dissertation, Texas Christian University, **2004**.

156. St. John, J.V. *Fabrication and Characterization of Rare Earth-Doped Silicon Nanocrystals and Rare Earth-Doped Silicon Dioxide Nanostructures,* Ph.D. Dissertation, Texas Christian University, **1998**.

157. Samia, A.; Burda, C.; Senter, R.; Coffer, J. *J. Chem. Phys.* **2004,** *120*, 8716.

158. Linsebigler, A.L.; Lu, G.; Yates, J.T. *Chem. Rev.* **1995,** *95*, 735.

159. Ji, J.; Chen, Y.; Senter, R.A.; Coffer, J.L. *Chem. Mater.* **2001,** *13*, 4783.

160. Michel, J.; Benton, J.L.; Ferrante, R.F.; Jacobson, D.C.; Eaglesham, D.J.; Fitzegerald, E.A.; Xie, Y.; Poate, J.M.; Kimerling, L.C. *J. Appl. Phys.* **1991,** *70*, 2672.

161. Bang, J.; Yang, H.; Holloway, P.H. *Nanotechnology* **2006,** *17*, 973.

162. Corriu, R.; Leclercq, D.; Lefevre, P.; Mutin, P.H.; Vioux, A. *Chem. Mater.* **1992,** *4*, 961.

163. Vioux, A. *Chem. Mater.* **1997,** *9*, 2292.

164. Hay, J.N.; Raval, H.M. *Chem. Mater.* **2001,** *13*, 3396.

165. Tessler, L.R.; Coffer, J.L.; Ji, J.; Senter, R.A. *J. Non Cryst. Solids.* **2002,** *299*, 673.

166. Schubert, U.; Hüsing, N. *Synthesis of Inorganic Materials*, **2000**, Wiley-VCH, Weinheim.

VITA

Vladimir Victor Seregin was born in Zagork, Russia on February 1, 1979. He is the oldest child of Victor V. Seregin and Olga A. Lamont. A 1996 graduate of High School #6 in Sergiev Posad, Russia, Vladimir pursued a Bachelor of Science Degree (B.S.) at Mendeleev University of Chemical Technology, Moscow, Russia. In August, 1996, Vladimir immigrated to the United States and went on to receive an Associate of Science Degree with a major in chemistry from Kilgore College, Kilgore, Texas, in 1999. In 2001 Vladimir received a B.S. Degree with majors in chemistry and mathematics from Texas A&M University-Commerce in Commerce, Texas. Vladimir entered Texas Christian University in August, 2001, to pursue his doctorate in inorganic/materials chemistry under the direction of Prof. Jeffery L. Coffer.

EXTENDED ABSTRACT

PART I: FABRICATION AND SURFACE MODIFICATION OF COMPOSITE BIOMATERIALS BASED ON SILICON AND CALCIUM DISILICIDE; PART II: SYNTHESIS AND CHARACTERIZATION OF ERBIUM DOPED SILICON NANOCRYSTALS ENCAPSULATED BY ALUMINUM AND ZINC OXIDES

by

Vladimir Victor Seregin, Ph. D., 2006
Department of Chemistry
Texas Chemistry University

Dissertation Advisor: Jeffery L. Coffer, Professor of Chemistry
and Chair of the Department

A dry-etch spark ablation method was used to produce porous silica (SiO_2/Si) and calcium disilicide ($CaSi_2/Si$) layers on silicon (Si) surfaces for the electrochemical growth of apatitic phosphates (CaP). Both SiO_2/Si and $CaSi_2/Si$ composite electrodes readily calcify *in vitro* under the application of a small electric potential, and with proper treatment the electrodeposition of CaP is localized to the sparked areas. Porous SiO_2 films can also be fabricated via a guided ablation technique and subsequently produce patterns of CaP on Si. In addition to increasing the local concentration of Ca^{2+}, interfacial layers of $CaSi_2$ on Si exhibit exceptional site-selectivity towards CaP formation under bias due to the difference in conductivity between Si and $CaSi_2$. The proposed mechanism for bias-assisted biomineralization of $CaSi_2/Si$ layers on spark-processed Si accounts for the physicochemical properties of deposited CaP films. This work also describes routes to surface modification of calcified composite electrodes with medicinally relevant compounds such as alendronate and norfloxacin. To assess the

suitability of this material as an antibiotic delivery platform, release of the latter compound was also monitored as a function of time.

Next, biomineralization of $CaSi_2$/Si layers on Si surfaces under *zero* bias was followed by means of Scanning Electron Microscopy (SEM), X-Ray Energy Dispersive Analysis (EDX), and Raman spectroscopy. $CaSi_2$/Si wafers are bioinert at 25°C and bioactive at 37°C. Mechanistic insights regarding biomineralization were derived from an analysis of film growth morphology and chemical composition after various soaking periods in standard SBF. Changes in $CaSi_2$ calcification behavior as a function of reaction temperature and pH, SBF concentration, and various surface modification processes were also employed for this purpose. During $CaSi_2$/Si calcification under zero bias, CaP growth is significantly dependent on the structural degradation of $CaSi_2$ grains. Surface silanol groups, initially present on the as-prepared material, cannot induce CaP nucleation which begins only upon delamination of $CaSi_2$ layers. The CaP phases, which are present during various growth stages, possibly include a combination of Mg-substituted whitlockite, monetite, and tricalcium phosphate.

The incorporation of $CaSi_2$ grains within a polycaprolactone (PCL) framework results in bioactive and biodegradable scaffolds which may be used in bone tissue regeneration. Porous PCL scaffolds were prepared via a combination of salt-leaching/microemulsion methods. To provide markedly different structural environments for the inorganic phase, calcium disilicide powder was either added to a mixed-composition porogen during a given scaffold’s preparation, or alternatively added to pre-formed scaffolds. Selective fluorescent labeling, SEM, and EDX were employed to assess scaffold calcification *in vitro*. The process of $CaSi_2$/PCL scaffold calcification under zero bias, during which CaP growth is significantly dependent on the structural degradation of $CaSi_2$ grains, has a similar mechanism to CaP growth on bioactive glasses/ceramics. The biomineralization of these scaffolds is initiated solely by the silicide phase and can be accelerated by the degradation of the polymer matrix.

A separate part of this work deals with rare earth-doped Si nanocrystals. Photoexcited erbium-doped silicon nanocrystals (Er/Si-NCs) emit at 1.54 μm, the wavelength of light which is the most compatible with existing silica-based fiber optics. Several selective surface modification reactions with inorganic capping layers comprised of either aluminum or zinc oxide were analyzed in an attempt to improve the photoluminescence (PL) efficiency of these nanocrystals by reducing interfacial defect density. It is shown that coating Er/Si-NCs with aluminum oxide via kinetically controlled chemical reaction doubles the PL efficiency. Zinc oxide, deposited under thermodynamic control, improves the PL by a factor of four. Such processes demonstrate the impact of surface modification on dopant photophysics.